

Tom Lahmer

Herausgeber
Timon Rabczuk

Carsten Könke

ISM-Bericht 2/2014
Institut für Strukturmechanik
Fakultät Bauingenieurwesen
Bauhaus-Universität Weimar
Marienstraße 15
D-99423 Weimar
Germany

ISSN: 1610-7381

Tel. +49 (0)3643/584504
Fax. +49(0)3643/584514

<http://www.uni-weimar.de/Bauing/ism>

**Numerical Simulation of Thermo-Chemo-Hygro-
Mechanical Alkali-Silica Reaction Model in Concrete
at the Mesoscale and Macroscale**

DISSERTATION

zur Erlangung des akademischen Grades
Doktor-Ingenieur (Dr.-Ing.)
an der Fakultät Bauingenieurwesen
der
Bauhaus-Universität Weimar

vorgelegt von
Zarina Itam
geboren am 05.08.1978 in Liverpool

Weimar, September 2012

Mentor:

Prof. Dr.-Ing. habil Carsten Könke

Gutachter:

Prof. Dr.-Ing. habil Detlef Kuhl, Universität Kassel

Prof. Dr.-Ing. Reinhard Harte, Bergische Universität Wuppertal

Disputation am 28. März 2014

ABSTRACT

Alkali-silica reaction causes major problems in concrete structures due to the rapidity of its deformation which leads to the serviceability limit of the structure being reached well before its time. Factors that affect ASR vary greatly, including alkali and silica content, relative humidity, temperature and porosity of the cementitious matrix, all these making it a very complex phenomenon to consider explicitly. With this in mind, the finite element technique was used to build models and generate expansive pressures and damage propagation due to ASR under the influence of thermo-hygro-chemoelastic loading. Since ASR initializes in the mesoscopic regions of the concrete, the accumulative effects of its expansion escalates onto the macroscale level with the development of web cracking on the concrete surface, hence solution of the damage model as well as simulation of the ASR phenomenon at both the macroscale and mesoscale levels have been performed. The macroscale model realizes the effects of ASR expansion as a whole and shows how it develops under the influence of moisture, thermal and mechanical loading. Results of the macroscale modeling are smeared throughout the structure and are sufficient to show how damage due to ASR expansion orientates. As opposed to the mesoscale model, the heterogeneity of the model shows us how difference in material properties between aggregates and the cementitious matrix facilitates ASR expansion. With both these models, the ASR phenomenon under influence of thermo-chemo-hygro-mechanical loading can be better understood.

ZUSAMMENFASSUNG

Die Alkali-Kieselsäure-Reaktion (AKR) verursacht aufgrund der hohen Geschwindigkeit ihrer Deformation erhebliche Schäden an Betonbauwerken. Dies führt zu Ermüdungserscheinungen an den Bauwerken, weit vor Erreichen der eigentlich möglichen Lebensdauer. Die Anzahl verschiedener Faktoren, welche die AKR beeinflussen, insbesondere der Alkali- und Kieselsäureanteil, die relative Feuchtigkeit, die Temperatur sowie die Porosität der Zementmatrix, machen das Phänomen schwer vorhersehbar. Unter Verwendung der Methode der finiten Elemente wurde ein Modell erstellt, welches die expansiven Drücke und die sich ausbreitenden Risse, die durch AKR unter dem Einfluss thermischer, hygrischer und chemo-elastischer Belastungen entstehen, abbildet. Da die AKR in den mesoskopischen Regionen des Zements beginnt und sich auf makroskopischer Ebene durch akkumulierende Effekte in Form von netzartigen Rissen auf der Zementoberfläche ausbreitet, wurden Lösungen des Schadensmodells und Simulationen der AKR-Phänomene sowohl auf der makro- als auch auf der mesoskopischen Ebene durchgeführt. Mit dem makroskopischen Modell werden die globalen Ausdehnungseffekte der AKR abgebildet und die fortschreitende Entwicklung der AKR unter dem Einfluss von Feuchtigkeit, sowie thermischen und mechanischen Belastungen simuliert. Die Ergebnisse der makroskopischen Modellierung verweisen durch die Struktur und sind ausreichend, um die Orientierung der Schadensausbreitung infolge der AKR aufzuzeigen. Demgegenüber zeigt die Heterogenität des Modells auf der mesoskopischen Ebene wie unterschiedliche Materialeigenschaften von Aggregaten und Zementmatrix die Ausbreitung der AKR begünstigen. Zusammen tragen beide Modelle zu einem besseren Verständnis des Einflusses von thermo-chemo-hygro-mechanischen Belastungen bei.

ACKNOWLEDGEMENT

“Knowledge is in the end based on acknowledgement”

Ludwig Wittgenstein (1969)

As much as doing the Ph.D seemed like a lonely journey, there are a lot of people that have been with me all the while. Without the financial support from the Ministry of Higher Education of Malaysia and University Technology MARA, this thesis would never have been realized. Thank you.

I would like to express my gratitude to Prof. Dr.-Ing. habil. Carsten Könke and the staff of Institut für Struktur-Mechanik, for their patience and guidance. I am also indebted to Prof. Dr.-Ing. Jochen Stark and the staff from the Finger-Institut Baustoffkunde for their contributions towards the research.

My sincerest gratitude towards the Bauhaus-Universität Weimar for being my second home these last few years giving me not only a lifetime of memories, but also the extra funding for my thesis through the HIWI vertrag and the Frauenförderung stipendium.

I would like to express my deepest gratitude to my parents, Prof. Dr. Itam Sulaiman and Hamidah Mat Isa for always believing in me. For the patience and support and neverending motivation. And to my son, Daniel, thank you for understanding all the time we spent apart, this is for you. Not forgetting my Srikandi friends for their comfort and encouragement. Thank you.

TABLE OF CONTENTS

ABSTRACT	iii
ZUSAMMENFASSUNG	v
ACKNOWLEDGEMENT	vii
TABLE OF CONTENTS	ix
NOMENCLATURE	xiii
1 INTRODUCTION	1
1.1 MOTIVATION OF RESEARCH	1
1.2 SCOPE OF RESEARCH	3
1.3 THESIS OUTLINE	4
2 OVERVIEW OF THE FINITE ELEMENT METHOD	7
2.1 INTRODUCTION	7
2.2 DEFORMATION AND KINEMATIC EQUATIONS	8
2.2.1 The Lagrangian Description of Motion	8
2.2.2 The Eulerian Description of Motion	9
2.3 CONSTITUTIVE EQUATIONS FOR MECHANICAL MODELING	10
2.3.1 Plane Elasticity	14
2.4 SPATIAL DISCRETIZATION OF THE EQUATION OF MOTION	15
2.4.1 Material Nonlinearity	21

2.5	ITERATION METHODS FOR FINITE ELEMENT ANALYSIS	22
2.5.1	Direct Iteration Method	22
2.5.2	Newton-Raphson Iteration Method	23
3	FLUID FLOW AND HEAT TRANSFER ANALYSIS	27
3.1	INTRODUCTION	27
3.2	CONSERVATION EQUATIONS FOR FLUID FLOW AND HEAT TRANSFER ANALYSIS	28
3.2.1	Conservation of Mass	29
3.2.2	Conservation of Linear Momentum	32
3.2.3	Conservation of Energy	34
3.3	POISSON'S PRESSURE EQUATION	35
3.4	CONSTITUTIVE EQUATIONS FOR FLUID FLOW AND HEAT TRANSFER ANALYSIS	37
3.5	FINITE ELEMENT IMPLEMENTATION	39
3.5.1	Spatial Discretization for Fluid Flow and Heat Transfer Equations	39
3.5.2	Temporal Discretization for Fluid Flow and Heat Transfer Equations	42
4	ALKALI-SILICA REACTION	45
4.1	INTRODUCTION	45
4.2	FACTORS INFLUENCING ASR	46
4.2.1	Alkali Content	46
4.2.2	Silica Content	47
4.2.3	Relative Humidity	48
4.2.4	External Sources of Reactants	49
4.2.5	Concrete Permeability and Porosity	51
4.2.6	Temperature	51
4.3	THE CHEMISTRY OF ASR	52
4.4	ASR MODELING CONSIDERATIONS	54
4.4.1	Relationship of ASR Strain to Reaction Extent	54
4.4.2	Relationship of ASR Strain to Temperature	57
4.4.3	Relationship of ASR Strain to Applied Stress	59
4.4.4	Relationship of ASR Strain to Relative Humidity	60

4.5	CONSERVATION EQUATIONS FOR ASR PROBLEMS	61
4.5.1	Conservation of Mass	61
4.5.2	Conservation of Linear Momentum	63
4.6	CONSTITUTIVE EQUATIONS FOR ASR ANALYSIS	64
4.7	HEAT AND MOISTURE DIFFUSION LENGTHS	70
5	DAMAGE MECHANICS	73
5.1	INTRODUCTION	73
5.2	DAMAGE FORMULATION	74
5.2.1	Strain-based Local Damage Formulation	76
5.2.2	Stress-based Local Damage Formulation	78
5.2.3	Nonlocal Damage Formulation	82
5.3	CONSTITUTIVE EQUATIONS FOR DAMAGE IN ASR ANALYSIS	84
5.4	FINITE ELEMENT IMPLEMENTATION OF THE DAMAGE ANALYSIS	85
6	MODELING ASR AT THE MACROSCALE	87
6.1	INTRODUCTION	87
6.2	MACROSCALE SIMULATION OF A CONCRETE GRAVITY DAM	88
6.2.1	Modeling Parameters	88
6.2.2	Theories and Assumptions	90
6.2.3	Heat Analysis for Transient Conditions	92
6.2.4	Thermal Stress Analysis for Transient Conditions	93
6.2.5	ASR and Hydrostatic Pressure Analysis for Constant Relative Humidity	96
6.2.6	ASR and Hydrostatic Pressure Analysis for Varying Relative Humidity	101
7	MODELING ASR AT THE MESOSCALE	106
7.1	INTRODUCTION	106
7.2	THE CONCEPT OF MESOSCALE MODELING	107
7.2.1	Aggregate Particles Shape Distribution (Take Process)	109
7.2.2	Aggregate Particles Size Distribution (Place Process)	112

7.3	ASR TESTING METHODS	114
7.3.1	Petrography	116
7.3.2	Mortar Bar Test	116
7.3.3	ASR Performance Test	118
7.4	NUMERICAL SIMULATION FOR ASR EXPANSION ANALYSIS	121
7.4.1	Modeling Parameters	121
7.4.2	Theories and Assumptions	123
7.4.3	Simulation of Experimental Results from the FIB	123
7.4.4	Simulation of Damage due to ASR Expansion	127
8	CONCLUSION	136
8.1	SUMMARY	136
8.2	FUTURE WORK	138
	BIBLIOGRAPHY	139

NOMENCLATURE

LOWER CASE LETTERS

a	Acceleration
c_x	Center points coordinates
d	Diameter
dV	Volume element
dV_m	Microscopic volume element
dV^π	Average volume element
dV^α	Volume element occupied by any constituent ϕ
dm^π	Local mass
e_i	Unit vector i of coordinate system
f_c	Compressive strength
f_t	Tensile strength
h	Height
h_e	Thickness of plate
k	Thermal conductivity coefficient
k^a	Coefficient for alkali-silica reaction velocity
k_c	Convective heat transfer coefficient
l	Length
n_j	Vector normal to the boundary surface
q	Heat flux
q_c	Convective components
r	Radii
t	Time
s^l	Water saturation
x	Distance
w_i	Weight functions
w_p	Weight of the aggregate particles
\mathbf{x}^π	Current position of each material point
\mathbf{x}'	Displacement vector of the material

CAPITAL LETTERS

A	Chemical reaction affinity (Only in Chapter 4)
A	Area
B^a	ASR gel bulk modulus
C_v	Specific heat capacity
C_a	ASR gel compliance
D	Diffusivity coefficient
E	Young's Modulus
$E(V)$	Expected value of the volume of aggregate particle
F_σ	Applied stress function
F^D	Thermodynamic force
G	Fracture energy
H	Relative humidity
M	Mass/Molar mass
M_i	Momentum equation (only in Chapter 3)
N_i	Interpolation function
P	Pressure
P^f	Fluid pressure
$P(d)$	Cumulative percentage passing a sieve
R	Ideal gas constant
R	Nonlocal Radius (only in Chapters 6 and 7)
$R_{i=1,m}$	Reactants
T	Temperature
T_0	Initial temperature
U_a, U_C, U_L	Activation energies
U_e	Strain energy
\dot{U}	Energy release rate
V_T	Total volume of the specimen
V_E	Element volume
V_P	Volume of aggregates within a grading class
W	Work
Y_p	Specific weight
$\mathbf{A}, \bar{\mathbf{A}}$	Matrix for ellipsoids
\mathbf{B}, B_{ij}	Strain-displacement matrix
\mathbf{C}, C_{ijkl}	Elastic matrix of the mechanical properties
$\mathbf{D}_t, \mathbf{D}_r$	Transformation matrices for translations and rotations
\mathbf{F}	Body force vector
\mathbf{J}^s	Skeleton deformation gradient tensor
\mathbf{M}	Mass matrix
\mathbf{K}	Stiffness matrix
\mathbf{R}	Vector of internal nodal point loads
\mathbf{u}	Displacement/deformation
\mathbf{V}, V_i	Velocity vector
\mathbf{X}^π	Initial reference configuration point

GREEK LETTERS

κ_C	Permeability of concrete
μ_f	Viscosity of fluid
$\nu_{i=1,m}$	Stoichiometric coefficients
φ	Material constituents
α	Moving phase under consideration in π
π	Phase in the material
α_T	Linear coefficient of thermal expansion at 20°C
β_T	Volumetric coefficient of thermal expansion at 20°C
Π	Element potential energy
ω	Damage variable
ϵ	Error tolerance
κ	Threshold value (only in Chapter 5)
Ω	Domain
ψ	Free energy
ν	Poisson's ratio
ϕ^π	Volume fraction, porosity
ϕ_m	Mass fraction of aggregate for one mineral class
ρ	Partial density
ρ_0	Initial material density
ρ_f	Fluid density
ϱ	Material density
ξ	Reaction extent of ASR
σ	Stress vector/tensor
$\bar{\sigma}$	Effective stress vector/tensor
τ_C, τ_L	Characteristic and latency time constants
ϵ	Strain vector/tensor
ϵ^a	Free linear expansion for alkali-aggregate reaction
ϵ_∞	Asymptotic ASR expansion
ϵ^{th}	Thermal strain tensor
ϵ_{100}	Free expansion at 100% H
η_{13}	Maximum ratio between two radii r_{ij}
Ψ, Φ, Θ	Vectors of interpolation functions
λ, μ	Lamé constants
δ_{ij}	Kronecker delta
γ^π	Phase distribution function
Γ	Domain boundary surface

1 INTRODUCTION

1.1 MOTIVATION OF RESEARCH

Concrete has been the building block of construction for centuries, dating back to ancient civilizations like the Roman Empire. However, problems with concrete may arise not only from design errors like insufficient materials used in the construction, but also from the effects of environmental conditions like freezing and thawing, carbonation and alkali-silica reaction. Damage to concrete due to alkali-silica reaction, or ASR is a phenomenon that was first recognized in the United States of America in the 1940s by Stanton (1940) and has since been observed in many other countries. Since then, many studies on that matter have been published.

Factors that affect ASR vary greatly although it is unanimous that ASR occurs between deleterious silica from aggregates and hydroxide ions in the pore solution that result from cement hydration. Other factors include the relative humidity, temperature and porosity of the cementitious matrix. Temperature influences the reaction kinetics of silica disintegration and causes thermal stresses in the structure. Moisture provides a transport medium for external sources of alkali and works as a swelling agent for the gel which is hydrophilic in nature. The resultant gel flows into the voids or accumulates on the aggregate surface. The gel expands with the availability of moisture, thus exerting internal pressure onto the surrounding matrix and lowering the concrete stiffness, in extreme cases to the point of cracking.

ASR deformation can be identified by a random network of crack patterns on its surface known as map cracking, leaching of the ASR gel and concrete spalling. ASR expansion in an affected concrete structure may happen rapidly and cause deformation to the structure well before its serviceability limit is reached, making the understanding

of its process crucial. What sets apart ASR from other concrete damage models is its heterogeneity, occurring at different concrete regions at different rates depending on the concrete composition as well as external influences, making predicting its behaviour somewhat difficult. The heterogeneity of the process depends on the pore distribution in the concrete and the rate of water diffusion into the reactive sites. The rate of ASR expansion in turn depends on temperature and the availability of chemical substances from within the matrix or from external sources.

Despite the fact that ASR initializes in the mesoscopic regions of the concrete, the accumulative effects of its expansion escalates onto the macroscale level with the development of web cracking on the concrete surface. Once the extent of damage that ASR brings onto the concrete structure on the macroscale has been determined, the mesoscale model is then studied to gain a more explicit insight on what happens at the material level. Macroscopic material models are characterized by considering the heterogeneities and structural defects in an averaged sense and are therefore regarded as a homogeneous material. Modeling on the mesoscale level however, allows the matrix adjacent to the aggregate surface to be developed. This allows us to study the different phases separately, for instance, the effects of ASR gel expansion on the aggregates as well as the bulk matrix due to the difference in material and physical parameters of the different phases.

In investigating the mechanical deformation of the structure, the theory of continuum damage mechanics proves to be a suitable method. Damage mechanics can be used to predict the physical and chemical behavior of a structure, making it an appropriate method to study the behavior of the structure under the influence of alkali-silica reactivity. Therefore solution of the damage model, as well as simulation of the ASR phenomenon at both the macroscale and mesoscale level in order to provide better understanding, or even solving the problem is critically needed. Numerical simulation has enabled us to build models for the representation of different physical phenomena based on different theories and approximately solvable by the finite element methods in numerous occasions. The potential of ASR simulation in detecting the possibility of concrete expansion and cracking at a fine scale gives new perspective to this deleterious phenomenon. With a reliable finite element simulation, the generation of expansive pressures and damage propagation due to ASR is possible.

1.2 SCOPE OF RESEARCH

This research aims to simulate three models for ASR expansion in concrete under the influence of thermo-hygro-chemoelastic loading for two different scales, the mesoscale and the macroscale. The first mesoscale model consists of a concrete prism modeled with material properties and boundary conditions determined from experimental settings by the Finger-Institute for Building Materials Science¹, which will be tested for the effects of thermal and moisture fluctuations under an accelerated condition to obtain rapid alkali-silica reactivity. The model is compared to experimental results as a validation procedure to prove the integrity of the simulation. The second mesoscale model compares the effects of different relative humidity values on ASR expansion in order to study the severity of damage caused by ASR in heterogeneous mediums.

The macroscale model consists of a simulation of an engineering example of a concrete gravity dam which will also be subjected to mechanical loading from hydrostatic pressure to test how ASR affected concrete behaves under such loading conditions. In order to achieve this aim, the ASR process is simulated to include the main influencing parameters that affect the stress states in the damage model, namely temperature, moisture and expansion due to chemical reactivity. The method that is implemented to solve both problems is the finite element technique.

This research was developed taking into account fluid flow and heat transfer analysis in the porous media. Understanding the relative humidity in concrete is crucial to predict the transport of pore fluid throughout concrete since it supplies hydroxide ions that causes silica to disintegrate and supplies the resulting ASR gel with water, causing it to expand. Traditional fluid flow simulation relies on the continuum approach and is represented by the Navier-Stokes equation. An extended version of this equation includes the effects of temperature as a buoyancy term in the right-hand side of the equation. Using the Navier-Stokes equation and the Penalty Method, the

¹ The Finger-Institute for Building Materials Science (FIB) is a centre of the research and teachings in the area of the building materials science at the Bauhaus-Universitaet Weimar in Germany. One of the researches conducted there is testing of the alkali-silica reaction using new testing methods.

temperature, velocity and pore pressure distributions throughout the model can be determined.

The heterogeneity of the concrete medium makes it difficult to replicate all the in field material and environmental parameters, hence some basic assumptions such as the porosity, environmental conditions and the aggregate size and distribution will be made. For this research, the mesoscale model was modeled from two phases, the aggregates and the bulk matrix. Although the chemical reaction between the alkali and silica in concrete is the main process in alkali-silica reactivity, the reaction, especially involving dissolved ionic species will not be modeled in the research. No phase changes will be considered in the simulation and moisture transport is treated as single-phased, which is water. The reaction rate of ASR gel follows the first-order kinetic model. Experimental results from concrete prism expansion tests conducted by the FIB yields ASR expansion rate values that will be used to validate the results from the numerical simulation.

The damage model for alkali-silica reactivity will be adapted from the isotropic damage model to include additional strains obtained from ASR expansion and thermal strains for both the mesoscale and macroscale model, and an additional hydrostatic pressure effect for the macroscale model. For matter of simplicity, the effects of creep and shrinkage are not considered in this research. The simulation of damage effects allows for the preliminary insights on the structure on the ASR damage initiation and orientation. This allows the investigation of the damage due to the combined effects of ASR chemoelastic strains, thermal strains and hydrostatic pressure at the material level as well as the structural level.

1.3 THESIS OUTLINE

This thesis has been divided into eight chapters. Following the introduction of the thesis in Chapter One, Chapter Two outlines the fundamental law for the finite element analysis. Since this research will include structural mechanics as well as transport of heat and fluid in the porous media, the Eulerian and Lagrangian descriptions of motion will be introduced. The constitutive equations are outlined, after which the weak variational formulations are presented. The constitutive equation for the mechanical response of a structure will also be stated. These fundamental

equations will later be extended for thermal and ASR expansion problems in the next chapters. The derivations of spatial and temporal discretization for plane elements are also outlined.

In Chapter Three, the Navier-Stokes equation for fluid flow and heat transfer in a viscous, incompressible Newtonian fluid is elaborated. The equations are written for fluid in a porous media region using a Cartesian coordinate system x_1, x_2, x_3 in an Eulerian reference frame. The derivation of the weak formulation of the Navier-Stokes equation and the appropriate boundary conditions will be outlined. This chapter also includes the Poisson's pressure equation, which will be used to obtain the hydrostatic pressure distribution in the model. The theory for the θ -parameter family, a method used for solution linearization and temporal discretization for finite element analysis is also introduced. The constitutive equation for the stress and strain relationship from Chapter Two is then extended for the inclusion of thermal stress.

Chapter Four describes the fundamental equations of the numerical simulation for ASR expansion. It outlines the formulation of the silica dissolution mechanism and ASR reaction rate. The main factors affecting the ASR expansion process such as temperature, relative humidity, external sources of alkali and applied stress are also discussed. The conservation equations for the ASR expansion process are also stated. To include the effects of ASR expansion on a structure, the constitutive equations from Chapter Two will be extended.

Chapter Five introduces the general concepts of continuum damage mechanics that are used in the isotropic damage model for brittle material, or in this case, concrete. The equation used for this research has additional strains from thermo-hygro-chemical coupling into the conventional stress and strain relationship. Constitutive relations of elasticity-based damage are first developed in a general format. These relations are then adapted to include the ASR strain, thermal strain and hydrostatic pressure.

Chapter Six presents a thermo-hygro-chemoelastic model developed on the macroscale level. The model will first be studied for thermal and ASR effects separately, and then the combined effects with hydrostatic pressure will be presented. The dam will be modeled as an isotropic damage model, allowing an explicit study of the initiation and orientation of ASR deterioration in a concrete structure.

Chapter Seven provides the details of the specimen preparation and the material parameters that were used in experiments to determine ASR expansion conducted by the FIB. The numerical model developed for this research is a two-dimensional mesoscale model of a concrete prism according to FIB specifications. The model was simulated as a validation model to prove the integrity of the simulation. This is followed by a study on a series of mesoscale models with different values of relative humidity in order to determine the severity that ASR damage brings to a concrete structure.

This is followed by a summary of conclusions in Chapter Eight.

2 OVERVIEW OF THE FINITE ELEMENT METHOD

2.1 INTRODUCTION

Numerical method is an approximate solution for engineering problems that is widely used nowadays because it lacks the complexities that come with using exact closed-form solutions. Evolution of the numerical method leads to methods of solution like the finite difference method, the finite volume method and the finite element method. Clough (1960) was the first person to use the term finite element method in the 1960s. In finite element simulation for structural mechanics, any physical problem can be represented in a mathematical model through a set of partial differential equations summing up the equilibrium, kinematic and constitutive equations. Various literatures can be found on the fundamentals of finite element analysis, for example by Cook (1995), Bathe (1996) and Reddy (2006). This chapter explains the kinematic equation for Eulerian description of motion which is used for heat and fluid transfer problems, and the Lagrangian description of motion which is used for mechanical problems of a structure. The constitutive equations for the stress and strain relationship for general three-dimensional problems will first be described and then adapted for plane elements. These equations are also applicable for various engineering fields and other problems like the convective heat transfer and ASR expansion problems which will be discussed in the next chapters. Spatial discretization of the equation of motion using weak formulation is also shown in this chapter.

2.2 DEFORMATION AND KINEMATIC EQUATIONS

There are two types of descriptions to express conservation laws, the Eulerian and the Lagrangian descriptions of motion. Meyer (1971) stated that the Eulerian description considers the fluid motion of all material passing through a fixed spatial location with respect to time for properties like velocity, pressure, temperature and density of the matter that instantly occupy the fixed spatial location. This makes it suitable for heat and fluid transfer problems. The Lagrangian description however, is used to study the deformation and kinematics for deforming solid bodies or porous medium continuum.

2.2.1 The Lagrangian Description of Motion

Lewis (1998) stated that in the Lagrangian or material description of motion, the current position of each material point \mathbf{x}^π is a function of its placement in an initial reference configuration point \mathbf{X}^π and of the current time, t :

$$\mathbf{X}^\pi = X_i^\pi \mathbf{e}_i \quad \mathbf{x}^\pi = \mathbf{x}^\pi(\mathbf{X}^\pi, t) \mathbf{e}_i \quad (2.1)$$

Where t denotes time and π represents the phase in the material which may be the skeleton, fluid or gas phase. The term \mathbf{e}_i is the Cartesian coordinate frame of orthogonal basis with $i=1,2,3$.

Assuming for skeleton deformation, the notation π in Equation (2.1) stands for the skeleton, s . By differentiating \mathbf{x}^s against \mathbf{X}^s , we get (Coussy 2004):

$$d\mathbf{x}^s = \frac{\partial \mathbf{x}^s}{\partial \mathbf{X}^s} d\mathbf{X}^s \mathbf{e}_i \quad (2.2)$$

With $\mathbf{J}^s = \frac{\partial x_i^s}{\partial X^s}$ or $\mathbf{J}^s = \text{grad } \mathbf{x}^s$. The term \mathbf{J}^s represents the skeleton deformation gradient tensor.

The motion of the skeleton is described by Bangert (2004) by introducing the displacement vector, \mathbf{x}'_s of the skeleton:

$$\mathbf{x}'_s = \mathbf{x}^s - \mathbf{X}^s \quad (2.3)$$

The first derivative of Equation (2.3) against time, t gives velocity, \mathbf{V}^s and the second derivative gives acceleration, \mathbf{a}^s (Lewis 1998):

$$\mathbf{V}^s = \frac{\partial \mathbf{x}'_s}{\partial t} \qquad \mathbf{a}^s = \frac{\partial^2 \mathbf{x}'_s}{\partial t^2} \qquad (2.4)$$

In considering structural deformation in this research, the Lagrangian description will be used.

2.2.2 The Eulerian Description of Motion

The Eulerian or spatial description of motion can be applied to heat transfer models in order to derive the relevant differential equations that describe its material behavior. Unlike the Lagrangian description, the Eulerian description does not involve the initial configuration point \mathbf{X}^π , but only the current configuration point \mathbf{x}^π . From Equation (2.1), the Eulerian description of motion (Lewis 1998) is obtained:

$$\mathbf{X}^\pi = \mathbf{X}^\pi(\mathbf{x}^\pi, t) \mathbf{e}_i \qquad (2.5)$$

The Eulerian description for velocity field, \mathbf{V}^π is determined as (Lewis 1998):

$$\mathbf{V}^\pi = \mathbf{V}^\pi(\mathbf{x}^\pi, t) \qquad (2.6)$$

And the time derivative of Equation (2.6) gives the acceleration, \mathbf{a}^π as:

$$\mathbf{a}^\pi = \frac{\partial \mathbf{V}^\pi}{\partial t} + \text{grad } \mathbf{V}^\pi \cdot \mathbf{V}^\pi \qquad (2.7)$$

Lewis (1998) stated that if α is a moving phase under consideration within a phase π in the material and assuming a differential function $f^\pi(\mathbf{x}, t)$, the material time derivative in its Eulerian description referring to a moving particle in phase π is described as:

$$\frac{D^\alpha f^\pi}{Dt} = \frac{\partial f^\pi}{\partial t} + f^\pi \text{ grad } \mathbf{V}^{\alpha\pi} \qquad (2.8)$$

Where $\mathbf{V}^{\alpha\pi} = \mathbf{V}^\alpha - \mathbf{V}^\pi$.

The motion of pore fluid and gas from the Eulerian description described relative to the deforming skeleton are given as:

$$\mathbf{V}^{fs} = \mathbf{V}^f - \mathbf{V}^s \qquad \mathbf{V}^{gs} = \mathbf{V}^g - \mathbf{V}^s \qquad (2.9)$$

In considering heat transfer problems in this research, where properties like velocity, pressure, temperature, and density of the material that occupy a fixed spatial location are to be studied, the Eulerian description will be used.

2.3 CONSTITUTIVE EQUATIONS FOR MECHANICAL MODELING

The constitutive equation is used to describe the response of a material to external forces applied onto a mechanical model. For ASR expansion analysis, the additional effects of thermal strain, ASR strain and hydrostatic pressure need to be adapted into the constitutive equation to provide a solution to the problem. This section briefs on the mechanical solution of the constitutive equation, while the adapted constitutive equation with additional thermal strains, ASR strains and hydrostatic pressure terms will be introduced in the following chapters.

To derive the constitutive equation for a three-dimensional body with a domain of Ω according to Reddy (1994), assume that a body force, F_i is prescribed onto the domain where $i=1,2,3$ in a global coordinate system. The domain boundary surface Γ_t is subjected to surface tractions and Γ_u is subjected to boundary displacements with the total domain boundary surface, $\Gamma = \Gamma_t \cup \Gamma_u$. Boundary conditions are a set of additional restraints used to define a problem and facilitate in the solution to a differential equation. For every boundary condition, two categories that are normally used are the Dirichlet or essential boundary condition and the Neumann or natural boundary condition (Reddy 1994):

$$\text{Dirichlet or essential boundary condition:} \quad u_i = \bar{u}_i \quad \text{on } \Gamma_u \qquad (2.10)$$

$$\text{Neumann or natural boundary condition:} \quad \sigma_{ij}n_j = \bar{t}_i \quad \text{on } \Gamma_t \qquad (2.11)$$

Where \bar{t}_i is the surface traction vector and \bar{u}_i is the boundary displacement vector. The term n_j denotes the vector normal to the boundary surface.

The Dirichlet boundary conditions, when imposed onto an ordinary or a partial differential equation specify the values that a nodal solution u_i is to take on the boundary Γ_u of the domain Ω . On the other hand the Neumann boundary conditions, when imposed onto an ordinary or a partial differential equation specify the values that the normal derivative of a solution σ_{ij} is to take on the boundary Γ_t of the domain Ω (Reddy 1994).

For constant material properties that are independent of body deformation and assuming small displacements and a linear relationship between stresses, σ and strains, ϵ the constitutive equation for the incremental stress and strain relationship resulting from the motion of this body is:

$$\sigma_{ij} = C_{ijkl} \epsilon_{kl} \quad \text{in } \Omega \quad (2.12)$$

Where $i, j, k, l = 1, 2, 3$. The term C_{ijkl} is the fourth-order linear elastic material tensor that can be written as:

$$C_{ijkl} = \lambda \delta_{ij} \delta_{kl} + \mu (\delta_{ik} \delta_{jl} + \delta_{il} \delta_{jk}) \quad (2.13)$$

The linear elastic material tensor, C_{ijkl} related to the undeformed state of the skeleton for isotropic material behavior is represented by:

$$C_{ijkl} = \frac{E(1-\nu)}{(1+\nu)(1-2\nu)} \begin{bmatrix} 1-\nu & \nu & \nu & 0 & 0 & 0 \\ \nu & 1-\nu & \nu & 0 & 0 & 0 \\ \nu & \nu & 1-\nu & 0 & 0 & 0 \\ 0 & 0 & 0 & \frac{1-2\nu}{2} & 0 & 0 \\ 0 & 0 & 0 & 0 & \frac{1-2\nu}{2} & 0 \\ 0 & 0 & 0 & 0 & 0 & \frac{1-2\nu}{2} \end{bmatrix} \quad (2.14)$$

The terms λ and μ denote the Lamé constants and δ represents the Kronecker delta which is defined as:

$$\delta_{ij} = \begin{cases} 1 & \text{if } i = j \\ 0 & \text{if } i \neq j \end{cases} \quad (2.15)$$

The Lamé constants, λ and μ in Equation (2.13) can be expressed in terms of Young's modulus, E and Poisson's ratio, ν :

$$\lambda = \frac{E\nu}{(1+\nu)(1-2\nu)} \quad \mu = \frac{E}{2(1+\nu)} \quad (2.16)$$

The strain state, ε_{ij} in terms of displacements is defined from:

$$\varepsilon_{ij} = \frac{1}{2} \left(\frac{\partial u_i}{\partial x_j} + \frac{\partial u_j}{\partial x_i} \right) \quad \text{in } \Omega \quad (2.17)$$

In solving a problem with the finite element method, spatial discretization needs to be performed onto a finite difference equation to give it a finite solution. This is achieved by introducing an interpolation function, N_i into the equation. Interpolation functions are used to determine the value of the field variable within an element by interpolating the nodal values. If V_E represents the element volume, the interpolation function, N_i is shown below:

$$\sum_{i=1}^N N_i(x_i) = \begin{bmatrix} N_1 & 0 & 0 & N_2 & 0 & 0 & \dots & N_N & 0 & 0 \\ 0 & N_1 & 0 & 0 & N_2 & 0 & \dots & 0 & N_N & 0 \\ 0 & 0 & N_1 & 0 & 0 & N_2 & \dots & 0 & 0 & N_N \end{bmatrix} \quad \text{in } V_E \quad (2.18)$$

Where $x_i = x_1, x_2, x_3$ is the global coordinate system coordinates and $\sum_{i=1}^N N_i(x_i) = 1$.

$$u_i(x_i) = \sum_{i=1}^N N_i(x_i) \hat{u}_i \quad \text{in } V_E \quad (2.19)$$

$$\begin{Bmatrix} u_1 \\ u_2 \\ u_3 \end{Bmatrix} = \begin{bmatrix} N_1 & 0 & 0 & N_2 & 0 & 0 & \dots & N_N & 0 & 0 \\ 0 & N_1 & 0 & 0 & N_2 & 0 & \dots & 0 & N_N & 0 \\ 0 & 0 & N_1 & 0 & 0 & N_2 & \dots & 0 & 0 & N_N \end{bmatrix} \begin{Bmatrix} \hat{u}_{11} \\ \hat{u}_{12} \\ \hat{u}_{13} \\ \hat{u}_{21} \\ \hat{u}_{22} \\ \hat{u}_{23} \\ \dots \\ \hat{u}_{N1} \\ \hat{u}_{N2} \\ \hat{u}_{N3} \end{Bmatrix}$$

By using the interpolation function, N_i from Equation (2.18) and a vector of global nodal displacement values, \hat{u}_i , the unknown nodal displacement field, u_i within an element can be approximated.

The strain-displacement matrix, B_{ij} is written as the linear gradient operator, ∂ multiplied with the interpolation function, N_i :

$$B_{ij}(x_i) = \partial N_i(x_i) \quad (2.20)$$

$$B_{ij} = \begin{bmatrix} \frac{\partial}{\partial x_1} & 0 & 0 \\ 0 & \frac{\partial}{\partial x_2} & 0 \\ 0 & 0 & \frac{\partial}{\partial x_3} \\ \frac{\partial}{\partial x_2} & \frac{\partial}{\partial x_1} & 0 \\ \frac{\partial}{\partial x_3} & 0 & \frac{\partial}{\partial x_1} \\ 0 & \frac{\partial}{\partial x_3} & \frac{\partial}{\partial x_2} \end{bmatrix} \begin{bmatrix} N_1 & 0 & 0 & N_2 & 0 & 0 & \dots & N_N & 0 & 0 \\ 0 & N_1 & 0 & 0 & N_2 & 0 & \dots & 0 & N_N & 0 \\ 0 & 0 & N_1 & 0 & 0 & N_2 & \dots & 0 & 0 & N_N \end{bmatrix}$$

The strain-displacement matrix, B_{ij} is used to transform nodal displacements, \hat{u}_i to strains at any point in the element in the domain, Ω . The relationship between the approximation of strains and displacements can be written as:

$$\varepsilon(x_i) = B_{ij}(x_i) \hat{u}_i \quad \text{in } V_E \quad (2.21)$$

$$\begin{bmatrix} \varepsilon_{11} \\ \varepsilon_{22} \\ \varepsilon_{33} \\ \gamma_{12} \\ \gamma_{13} \\ \gamma_{23} \end{bmatrix} = \begin{bmatrix} \frac{\partial N_1}{\partial x_1} & 0 & 0 & \frac{\partial N_2}{\partial x_1} & 0 & 0 & \dots & \frac{\partial N_n}{\partial x_1} & 0 & 0 \\ 0 & \frac{\partial N_1}{\partial x_2} & 0 & 0 & \frac{\partial N_2}{\partial x_2} & 0 & \dots & 0 & \frac{\partial N_n}{\partial x_2} & 0 \\ 0 & 0 & \frac{\partial N_1}{\partial x_3} & 0 & 0 & \frac{\partial N_2}{\partial x_3} & \dots & 0 & 0 & \frac{\partial N_n}{\partial x_3} \\ \frac{\partial N_1}{\partial x_2} & \frac{\partial N_1}{\partial x_1} & 0 & \frac{\partial N_2}{\partial x_2} & \frac{\partial N_2}{\partial x_1} & 0 & \dots & \frac{\partial N_n}{\partial x_2} & \frac{\partial N_n}{\partial x_1} & 0 \\ \frac{\partial N_1}{\partial x_3} & 0 & \frac{\partial N_1}{\partial x_1} & \frac{\partial N_2}{\partial x_3} & 0 & \frac{\partial N_2}{\partial x_1} & \dots & \frac{\partial N_n}{\partial x_3} & 0 & \frac{\partial N_n}{\partial x_1} \\ 0 & \frac{\partial N_1}{\partial x_3} & \frac{\partial N_1}{\partial x_2} & 0 & \frac{\partial N_2}{\partial x_3} & \frac{\partial N_2}{\partial x_2} & \dots & 0 & \frac{\partial N_n}{\partial x_3} & \frac{\partial N_n}{\partial x_2} \end{bmatrix} \begin{bmatrix} \hat{u}_{11} \\ \hat{u}_{12} \\ \hat{u}_{13} \\ \hat{u}_{21} \\ \hat{u}_{22} \\ \hat{u}_{23} \\ \dots \\ \hat{u}_{N1} \\ \hat{u}_{N2} \\ \hat{u}_{N3} \end{bmatrix}$$

The stress and strain relationship from Equation (2.12) can now be rewritten as:

$$\sigma_{ij}(x_i) = C_{ijkl} B_{ij}(x_i) \hat{u}_i = C_{ijkl} \varepsilon_{kl}(x_i) \quad (2.22)$$

$$\begin{bmatrix} \sigma_{11} \\ \sigma_{22} \\ \sigma_{33} \\ \sigma_{12} \\ \sigma_{13} \\ \sigma_{23} \end{bmatrix} = \frac{E(1-\nu)}{(1+\nu)(1-2\nu)} \begin{bmatrix} 1-\nu & \nu & \nu & 0 & 0 & 0 \\ \nu & 1-\nu & \nu & 0 & 0 & 0 \\ \nu & \nu & 1-\nu & 0 & 0 & 0 \\ 0 & 0 & 0 & \frac{1-2\nu}{2} & 0 & 0 \\ 0 & 0 & 0 & 0 & \frac{1-2\nu}{2} & 0 \\ 0 & 0 & 0 & 0 & 0 & \frac{1-2\nu}{2} \end{bmatrix} \begin{bmatrix} \varepsilon_{11} \\ \varepsilon_{22} \\ \varepsilon_{33} \\ \gamma_{12} \\ \gamma_{13} \\ \gamma_{23} \end{bmatrix}$$

2.3.1 Plane Elasticity

According to Kythe (2003) in considering plane elasticity, two-dimensional plane elements are considered as a thin body. For plane stress problems, the x_3 direction is negligible, therefore rendering the stress in x_3 direction as zero:

$$\sigma_{33} = \sigma_{23} = \sigma_{13} = 0, \quad \sigma_{11} = \sigma_{11}(x_1, x_2), \quad \sigma_{12} = \sigma_{12}(x_1, x_2), \quad \sigma_{22} = \sigma_{22}(x_1, x_2) \quad (2.23)$$

The corresponding strain field is obtained from the stress and strain relationship:

$$\begin{Bmatrix} \sigma_{11} \\ \sigma_{22} \\ \sigma_{12} \end{Bmatrix} = \begin{bmatrix} C_{11} & C_{12} & 0 \\ C_{21} & C_{22} & 0 \\ 0 & 0 & C_{66} \end{bmatrix} \begin{Bmatrix} \varepsilon_{11} \\ \varepsilon_{22} \\ \gamma_{12} \end{Bmatrix} \quad (2.24)$$

Where the fourth-order elastic stiffness, \mathbf{C} for plane stress problem is given as:

$$\mathbf{C} = \frac{E}{1-\nu^2} \begin{bmatrix} 1 & \nu & 0 \\ \nu & 1 & 0 \\ 0 & 0 & \frac{1-\nu}{2} \end{bmatrix} \quad (2.25)$$

As opposed to the plane stress problems, the plane elements for plane strain problems are assumed as a thick body where the strain in the x_3 direction is assumed as zero (Reddy 2006).

The strains are characterized by the displacement field, u_i , which is defined as:

$$u_1 = u_1(x_1, x_2), \quad u_2 = u_2(x_1, x_2), \quad u_3 = 0 \quad (2.26)$$

The resulting strains are defined as:

$$\varepsilon_{33} = \gamma_{23} = \gamma_{13} = 0, \quad \varepsilon_{11} = \frac{\partial u_1}{\partial x_1}, \quad \gamma_{12} = \frac{\partial u_1}{\partial x_2} + \frac{\partial u_2}{\partial x_1}, \quad \varepsilon_{22} = \frac{\partial u_2}{\partial x_2} \quad (2.27)$$

And the corresponding stress field is obtained from Equation (2.24), but with the fourth-order elastic stiffness, \mathbf{C} for plane strain problem given as:

$$\mathbf{C} = \frac{E}{(1+\nu)(1-2\nu)} \begin{bmatrix} 1-\nu & \nu & 0 \\ \nu & 1-\nu & 0 \\ 0 & 0 & \frac{1-2\nu}{2} \end{bmatrix} \quad (2.28)$$

2.4 SPATIAL DISCRETIZATION OF THE EQUATION OF MOTION

The finite element discretization is a process of dividing the solution region into nonoverlapping elements, reducing a continuum problem which has an infinite number of unknowns to one with a finite number of unknowns at specified points referred to as nodes. Each element is formed by the connection of a certain number of nodes, with a minimum of three nodes. The number of nodes to make an element depends on the type of element and interpolation function. The method states that a differential equation can be solved by a set of linearly combined unknown parameters of selected approximation functions that satisfy the boundary conditions in the entire domain of the problem. In order to perform this, any finite difference equation needs to be spatially discretized using the weak formulation.

Reddy (2006) gives the equilibrium equation for motion for plane strain and stress in terms of displacement vector \mathbf{u} , or also known as the principle of virtual displacements for static problems as:

$$\mathbf{BCBu} = \mathbf{F} \quad \text{on } \Omega \quad (2.29)$$

$$\frac{\partial}{\partial x_1} \left(c_{11} \frac{\partial u_1}{\partial x_1} + c_{12} \frac{\partial u_2}{\partial x_2} \right) + \frac{\partial}{\partial x_2} c_{66} \left(\frac{\partial u_1}{\partial x_2} + \frac{\partial u_2}{\partial x_1} \right) = F_1 \quad (2.30)$$

$$\frac{\partial}{\partial x_1} c_{66} \left(\frac{\partial u_1}{\partial x_2} + \frac{\partial u_2}{\partial x_1} \right) + \frac{\partial}{\partial x_2} \left(c_{12} \frac{\partial u_1}{\partial x_1} + c_{22} \frac{\partial u_2}{\partial x_2} \right) = F_2 \quad (2.31)$$

Where F_1 and F_2 are body force vectors per unit volume for x_1 and x_2 direction respectively. The respective vectors are defined as:

$$\partial = \begin{bmatrix} \frac{\partial}{\partial x_1} & 0 & \frac{\partial}{\partial x_2} \\ 0 & \frac{\partial}{\partial x_2} & \frac{\partial}{\partial x_1} \end{bmatrix}, \quad \sigma_{ij} = \begin{Bmatrix} \sigma_{11} \\ \sigma_{22} \\ \sigma_{12} \end{Bmatrix}, \quad F_i = \begin{Bmatrix} F_1 \\ F_2 \end{Bmatrix}, \quad u_i = \begin{Bmatrix} u_1 \\ u_2 \end{Bmatrix} \quad (2.32)$$

And the bracketed terms represent stresses with:

$$\sigma_{11} = c_{11} \frac{\partial u_1}{\partial x_1} + c_{12} \frac{\partial u_2}{\partial x_2}, \quad \sigma_{12} = c_{66} \left(\frac{\partial u_1}{\partial x_2} + \frac{\partial u_2}{\partial x_1} \right), \quad \sigma_{22} = c_{12} \frac{\partial u_1}{\partial x_1} + c_{22} \frac{\partial u_2}{\partial x_2} \quad (2.33)$$

The term $c_{ij} = h_e C_{ij}$, with h_e denoting the thickness of the plate.

The weak formulation of a differential equation fitted with its associated boundary conditions is a weighted-integral statement that is used to find a solution to that particular problem. The element matrix equations are assembled in such a way to obtain a system of simultaneous equations that represents the behavior of the entire solution region of the problem. The solution is then checked for convergence. For transient and nonlinear problems, the equations are also temporally discretized.

The weak variational formulation over a typical element domain, Ω for any function is obtained from three steps. In the first step, all nonzero terms are taken to one side of the equality and then integrated over the element domain Ω . From Equations (2.29) to (2.31), the equilibrium equations become (Reddy 2006):

$$0 = \int_{\Omega} \sigma_{ij} \delta \varepsilon_{ij} d\Omega - \int_{\Omega} F_i \delta u_i d\Omega - \oint_{\Gamma_t} t_i \delta u_i d\Gamma_t \quad (2.34)$$

In two-dimensional plane elements where the element thickness, h_e is zero, Equation (2.34) becomes:

$$0 = \int_{\Omega} h_e \left[\sigma_{11} \delta \varepsilon_{11} + \sigma_{22} \delta \varepsilon_{22} + 2\sigma_{12} \delta \varepsilon_{12} \right] dx_1 dx_2 - \int_{\Omega} h_e (F_1 \delta u_1 + F_2 \delta u_2) dx_1 dx_2 - \oint_{\Gamma_t} h_e (t_1 \delta u_1 + t_2 \delta u_2) d\Gamma_t \quad (2.35)$$

Where $\Omega = h_e dx_1 dx_2$. Here, \mathbf{F} becomes body forces per unit area and \mathbf{t} becomes the boundary forces per unit length.

The second step in weak formulation is to multiply Equation (2.35) with a weight function, w_i . The weight function, w_i is arbitrary but must satisfy the homogeneous essential boundary condition on \mathbf{u} (Reddy 2006). The weighted integral statements over an element domain Ω now become:

$$0 = \int_{\Omega} h_e \left(\frac{\partial w_1}{\partial x_1} \sigma_{11} + \frac{\partial w_1}{\partial x_2} \sigma_{12} - w_1 F_1 \right) dx_1 dx_2 - \oint_{\Gamma_t} h_e w_1 (\sigma_{11} n_1 + \sigma_{12} n_2) d\Gamma_t \quad (2.36)$$

$$0 = \int_{\Omega} h_e \left(\frac{\partial w_2}{\partial x_1} \sigma_{12} + \frac{\partial w_2}{\partial x_2} \sigma_{22} - w_2 F_2 \right) dx_1 dx_2 - \oint_{\Gamma_t} h_e w_2 (\sigma_{12} n_1 + \sigma_{22} n_2) d\Gamma_t \quad (2.37)$$

For the last step in the weak formulation, the boundary terms are simplified by using boundary conditions. This affects the boundary integral in Equations (2.36) and (2.37). The final weak formulation then becomes:

$$0 = \int_{\Omega} h_e \left[\frac{\partial w_1}{\partial x_1} \left(c_{11} \frac{\partial u_1}{\partial x_1} + c_{12} \frac{\partial u_2}{\partial x_2} \right) + c_{66} \frac{\partial w_1}{\partial x_2} \left(\frac{\partial u_1}{\partial x_2} + \frac{\partial u_2}{\partial x_1} \right) \right] dx_1 dx_2 - \int_{\Omega} h_e w_1 F_1 dx_1 dx_2 - \oint_{\Gamma_t} h_e w_1 t_1 d\Gamma_t \quad (2.38)$$

$$0 = \int_{\Omega} h_e \left[c_{66} \frac{\partial w_2}{\partial x_1} \left(\frac{\partial u_1}{\partial x_2} + \frac{\partial u_2}{\partial x_1} \right) + \frac{\partial w_2}{\partial x_2} \left(c_{12} \frac{\partial u_1}{\partial x_1} + c_{22} \frac{\partial u_2}{\partial x_2} \right) \right] dx_1 dx_2 - \int_{\Omega} h_e w_2 F_2 dx_1 dx_2 - \oint_{\Gamma_t} h_e w_2 t_2 d\Gamma_t \quad (2.39)$$

From the weak formulations above, the finite element model is obtained.

The weight function is defined by Reddy (2006) as:

$$\mathbf{w} = \partial \mathbf{u} = \begin{Bmatrix} w_1 = \partial u_1 \\ w_2 = \partial u_2 \end{Bmatrix} = N_i \partial u_i \quad (2.40)$$

Where the terms N_i and u_i are defined in Section 2.3.

Substituting Equation (2.40) into (2.38) and (2.39), we obtain (Reddy 2006):

$$0 = \int_{\Omega} h_e \left[\delta u_1 \left(c_{11} \frac{\partial N_i}{\partial x_1} \frac{\partial N_j}{\partial x_1} u_1 + c_{66} \frac{\partial N_i}{\partial x_2} \frac{\partial N_j}{\partial x_2} u_1 \right) + \delta u_1 \left(c_{12} \frac{\partial N_i}{\partial x_1} \frac{\partial N_j}{\partial x_2} u_2 + c_{66} \frac{\partial N_i}{\partial x_2} \frac{\partial N_j}{\partial x_1} u_2 \right) \right] dx_1 dx_2 - \int_{\Omega} h_e N_i \delta u_1 F_1 dx_1 dx_2 - \oint_{\Gamma_t} h_e N_i \delta u_1 t_1 d\Gamma_t \quad (2.41)$$

$$0 = \int_{\Omega} h_e \left[\delta u_2 \left(c_{66} \frac{\partial N_i}{\partial x_1} \frac{\partial N_j}{\partial x_1} u_2 + c_{22} \frac{\partial N_i}{\partial x_2} \frac{\partial N_j}{\partial x_2} u_2 \right) + \delta u_2 \left(c_{12} \frac{\partial N_i}{\partial x_1} \frac{\partial N_j}{\partial x_2} u_1 + c_{66} \frac{\partial N_i}{\partial x_2} \frac{\partial N_j}{\partial x_1} u_1 \right) \right] dx_1 dx_2 - \int_{\Omega} h_e N_i \delta u_2 F_2 dx_1 dx_2 - \oint_{\Gamma_t} h_e N_i \delta u_2 t_2 d\Gamma_t \quad (2.42)$$

Which can be represented in matrix form as below:

$$\begin{bmatrix} K_{11} & K_{12} \\ K_{21} & K_{22} \end{bmatrix} \begin{Bmatrix} u_1 \\ u_2 \end{Bmatrix} = \begin{Bmatrix} F_1 \\ F_2 \end{Bmatrix} \quad (2.43)$$

Where:

$$F_i^1 = \int_{\Omega} h_e N_i F_1 dx_1 dx_2 + \oint_{\Gamma_t} h_e N_i t_1 d\Gamma_t, \quad F_i^2 = \int_{\Omega} h_e N_i F_2 dx_1 dx_2 + \oint_{\Gamma_t} h_e N_i t_2 d\Gamma_t \quad (2.44)$$

$$K_{ij}^{11} = \int_{\Omega} h_e \left(c_{11} \frac{\partial N_i}{\partial x_1} \frac{\partial N_j}{\partial x_1} + c_{66} \frac{\partial N_i}{\partial x_2} \frac{\partial N_j}{\partial x_2} \right) dx_1 dx_2,$$

$$K_{ij}^{12} = K_{ij}^{21} = \int_{\Omega} h_e \left(c_{12} \frac{\partial N_i}{\partial x_1} \frac{\partial N_j}{\partial x_2} + c_{66} \frac{\partial N_i}{\partial x_2} \frac{\partial N_j}{\partial x_1} \right) dx_1 dx_2, \quad (2.45)$$

$$K_{ij}^{22} = \int_{\Omega} h_e \left(c_{66} \frac{\partial N_i}{\partial x_1} \frac{\partial N_j}{\partial x_1} + c_{22} \frac{\partial N_i}{\partial x_2} \frac{\partial N_j}{\partial x_2} \right) dx_1 dx_2$$

By replacing the strain-displacement matrix, \mathbf{B} and linear elastic material tensor, \mathbf{C} into Equations (2.41) and (2.42), we obtain:

$$\begin{aligned} 0 &= \delta u_i^T \left(\int_{\Omega} h_e \mathbf{B}^T \mathbf{C} \mathbf{B} u_i dx_1 dx_2 - \int_{\Omega} h_e N_i^T \mathbf{F} dx_1 dx_2 - \oint_{\Gamma_i} h_e N_i^T \mathbf{t} d\Gamma_i \right) \\ 0 &= \delta u_i^T (\mathbf{K} \mathbf{u} - \mathbf{F} - \mathbf{Q}) \end{aligned} \quad (2.46)$$

Since $\delta u_i^T = 0$, the relationship between the nodal unknowns and the corresponding acting forces is represented in the form of the following matrix:

$$\mathbf{K} \mathbf{u} = \mathbf{F} + \mathbf{Q} \quad (2.47)$$

Where \mathbf{u} is a vector of unknown variables and \mathbf{K} , \mathbf{F} and \mathbf{Q} are represented by:

$$\mathbf{K} = \int_{\Omega} h_e \mathbf{B}^T \mathbf{C} \mathbf{B} dx_1 dx_2 \quad (2.48)$$

$$\mathbf{F} + \mathbf{Q} = \int_{\Omega} h_e N_i^T \mathbf{F} dx_1 dx_2 + \oint_{\Gamma_i} h_e N_i^T \mathbf{t} d\Gamma_i \quad (2.49)$$

The element interpolation functions can also be stated in the natural coordinate system r and s , corresponding to the global coordinate system x_1 and x_2 . In the natural coordinate system r and s , the displacement field, u_i can be written as:

$$u_i(r, s) = \sum_{i=1}^N N_i(r, s) \hat{u}_i \quad (2.50)$$

$$x_{1i}(r, s) = \sum_{i=1}^N N_i(r, s) \hat{x}_{1i}, \quad x_{2i}(r, s) = \sum_{i=1}^N N_i(r, s) \hat{x}_{2i} \quad (2.51)$$

Where \hat{x}_i is the vector of global coordinates of node i .

Differentiating Equation (2.51), we obtain:

$$\frac{\partial x_1}{\partial r} = \sum_{i=1}^N x_{1i} \frac{\partial N_i}{\partial r}, \quad \frac{\partial x_2}{\partial r} = \sum_{i=1}^N x_{2i} \frac{\partial N_i}{\partial r} \quad (2.52)$$

$$\frac{\partial x_1}{\partial s} = \sum_{i=1}^N x_{1i} \frac{\partial N_i}{\partial s}, \quad \frac{\partial x_2}{\partial s} = \sum_{i=1}^N x_{2i} \frac{\partial N_i}{\partial s} \quad (2.53)$$

By applying the chain rule, the derivatives of the interpolation functions with respect to the global coordinates is obtained (Eckardt 2009):

$$\begin{bmatrix} \frac{\partial N}{\partial x_1} \\ \frac{\partial N}{\partial x_2} \end{bmatrix} = \underbrace{\begin{bmatrix} \frac{\partial r}{\partial x_1} & \frac{\partial s}{\partial x_1} \\ \frac{\partial r}{\partial x_2} & \frac{\partial s}{\partial x_2} \end{bmatrix}}_{\mathbf{J}^{-1}} \begin{bmatrix} \frac{\partial N}{\partial r} \\ \frac{\partial N}{\partial s} \end{bmatrix} \quad (2.54)$$

Where \mathbf{J} is the Jacobian matrix that acts as the connector between the two coordinates. This gives:

$$\frac{\partial N}{\partial x_1} = \frac{1}{|\mathbf{J}|} \left(\frac{\partial x_2}{\partial s} \frac{\partial N}{\partial r} - \frac{\partial x_2}{\partial r} \frac{\partial N}{\partial s} \right) \quad (2.55)$$

$$\frac{\partial N}{\partial x_2} = \frac{1}{|\mathbf{J}|} \left(-\frac{\partial x_1}{\partial s} \frac{\partial N}{\partial r} + \frac{\partial x_1}{\partial r} \frac{\partial N}{\partial s} \right) \quad (2.56)$$

Where $|\mathbf{J}| \neq 0$ denotes the determinant of \mathbf{J} which is nonsingular and defined as:

$$\det \mathbf{J} = \frac{\partial x_1}{\partial r} \frac{\partial x_2}{\partial s} - \frac{\partial x_1}{\partial s} \frac{\partial x_2}{\partial r} \neq 0 \quad (2.57)$$

Where $r, s = \pm 1$ from the center of an element are dimensionless coordinates with the element area given as:

$$dA = dx_1 dx_2 = |\mathbf{J}| dr ds \quad (2.58)$$

Assuming the boundary surfaces with surface tractions to be described as a function of r and s and using integration by substitution, in the natural coordinate system, Equations (2.48) to (2.49) become:

$$\mathbf{K} = \int_{\Omega} \mathbf{B}^T(r, s) \mathbf{C} \mathbf{B}(r, s) \det \mathbf{J}(r, s) dr ds \quad (2.59)$$

$$\mathbf{F}_{\text{ext},i} = \int_{\Omega} \mathbf{N}^T(r, s) \mathbf{F}(r, s) \det \mathbf{J}(r, s) dr ds + \oint_{\Omega} \mathbf{N}^T(r, s) \mathbf{t}(r, s) \sqrt{a_1(r, s)a_2(r, s) - a_3(r, s)^2} dr ds \quad (2.60)$$

The surface area, A of the element boundary is expressed by (Eckardt 2009):

$$A = \int_{\Omega} \sqrt{a_1(r,s)a_2(r,s) - a_3(r,s)^2} dr ds \quad (2.61)$$

Where

$$a_1 = \left(\frac{\partial x_1}{\partial r}\right)^2 + \left(\frac{\partial x_2}{\partial r}\right)^2, \quad a_2 = \left(\frac{\partial x_1}{\partial s}\right)^2 + \left(\frac{\partial x_2}{\partial s}\right)^2, \quad a_3 = \frac{\partial x_1}{\partial r} \frac{\partial x_1}{\partial s} + \frac{\partial x_2}{\partial r} \frac{\partial x_2}{\partial s} \quad (2.62)$$

2.4.1 Material Nonlinearity

For the stress and strain relationship in Equation (2.22), the material is assumed to be linear. However, as a consequence of body deformation, material can portray nonlinear behavior. This causes the stress and strain relationship to also become nonlinear. In this case, stress does not only depend on the current state of the material but it depends on the material deformation history as well. The weak form for the stress and strain relationship for nonlinear material as adapted from Equation (2.46) can be written as (Eckardt 2009):

$$0 = \delta u_i^T \left(\underbrace{\int_{\Omega} h_e \mathbf{B}^T \mathbf{C} \mathbf{B} u_i(x_1, x_2) dx_1 dx_2}_{\mathbf{F}_{\text{int}}} - \underbrace{\int_{\Omega} h_e N_i^T \mathbf{F} dx_1 dx_2 - \oint_{\Gamma_t} h_e N_i^T \mathbf{t} d\Gamma_t}_{\mathbf{F}_{\text{ext}}} \right) \quad (2.63)$$

The body force vector, \mathbf{F} consists of two vectors, the external body force, \mathbf{F}_{ext} and internal body force, \mathbf{F}_{int} , with $\mathbf{F}_{\text{int}}(u_i) = \mathbf{F}_{\text{ext}}$. An approximation of \mathbf{F}_{int} can be obtained from:

$$\begin{aligned} \mathbf{F}_{\text{int}}(u_i + \delta u_i) &= \int_{\Omega} \mathbf{B}^T \mathbf{C} \mathbf{B} u_i(x_1, x_2) dx_1 dx_2 + \int_{\Omega} \mathbf{B}^T \boldsymbol{\sigma}(\boldsymbol{\varepsilon}(x_1, x_2)) \delta \boldsymbol{\varepsilon}_k dx_1 dx_2 \\ &= \int_{\Omega} \mathbf{B}^T \mathbf{C} \mathbf{B} u_i(x_1, x_2) dx_1 dx_2 + \int_{\Omega} \mathbf{B}^T \boldsymbol{\sigma}(\boldsymbol{\varepsilon}(x_1, x_2)) dx_1 dx_2 \delta u_i \\ &= \mathbf{F}_{\text{int}}^i(u_i) + \mathbf{K}_{,il}(u_i) \delta u_i \end{aligned} \quad (2.64)$$

Where $\mathbf{K}_{,il}(u_i)$ is the tangential stiffness matrix.

As can be seen from Equation (2.64), \mathbf{F}_{int} is dependent on the strain state, hence also on the material nonlinearity. The stress values for material nonlinearity cases can be determined from the truncated Taylor series linearization method (Most 2005):

$$\sigma_i(\varepsilon + \delta\varepsilon) = \sigma_i(\varepsilon) + \frac{\partial\sigma_i}{\partial\varepsilon_j}(\varepsilon)\delta\varepsilon_j = \sigma_i(\varepsilon) + C_{ij}(\varepsilon)\delta\varepsilon_j \quad (2.65)$$

From the discretized formulations shown in this chapter, any problem can be solved within the finite element scope.

2.5 ITERATION METHODS FOR FINITE ELEMENT ANALYSIS

2.5.1 DIRECT ITERATION METHOD

Element coefficient matrixes that contain nonlinearity or unsymmetrical properties, for example, unknown velocity or thermal components in the coefficient matrix need to be solved with nonlinear iteration methods. One method of solution for this is the direct iteration method. One direct iteration method that can be used is the Picard method, which is written by Reddy (2006) as:

$$\mathbf{K}(\mathbf{u}^i)\mathbf{u}^{i+1} = \mathbf{F} \quad (2.66)$$

The term \mathbf{F} denotes the vector of externally applied nodal point loads and \mathbf{u}^i denotes the solution at the i th iteration, which is already known for the $(i+1)$ th iteration. The tangential stiffness matrix \mathbf{K} is dependent on \mathbf{u}^i and is first determined from Equation (2.66). Then the values of displacements for the next iteration, \mathbf{u}^{i+1} is determined. The new displacement values \mathbf{u}^{i+1} are determined from:

$$\mathbf{u}^{i+1} = \left(\mathbf{K}(\mathbf{u}^i)\right)^{-1} \mathbf{F} \quad (2.67)$$

The iteration is continued by solving Equation (2.66) for an updated tangential element stiffness matrix, \mathbf{K} until the difference between \mathbf{u}^i and \mathbf{u}^{i+1} is reduced to a predetermined error tolerance, ϵ , usually taken around 0.010 (Reddy 2006).

At this point, the simulation is said to have reached a converged solution where:

$$\frac{|\mathbf{u}_{n+1} - \mathbf{u}_n|}{|\mathbf{u}_{n+1}|} < \epsilon \quad (2.68)$$

Hence in this method, Equation (2.67) can be used to determine temperature, fluid and pressure distribution vectors.

2.5.2 NEWTON-RAPHSON ITERATION METHOD

Another method of solving for the nonlinear equation of motion for static analysis and implicit time integration can be performed with the Newton-Raphson iteration method. The Newton-Raphson iteration method is used for nonlinear problems to find the state of equilibrium of the body corresponding to the applied loads. This section introduces the concept of the Newton-Raphson procedure for a single degree of freedom problem and can be easily used for multiple degrees of freedom as well. It is based on the Taylor's series of expansion of the algebraic term $\mathbf{Ku}=\mathbf{F}$ (Bathe 1996). Detailed explanation regarding the Newton-Raphson iteration procedure can be found in literatures, for example by Cook (1995), Bathe (1996) and Reddy (2006). The equilibrium condition of a system of finite elements representing the body under consideration is expressed by Bathe (1996) as:

$$\mathbf{F}_{n+1} - \mathbf{R}^i = 0 \quad (2.69)$$

Where:

- \mathbf{R}^i = The vector of internal nodal point loads in the configuration that corresponds to the element stresses at iteration step, i
- \mathbf{F}_{n+1} = The vectors of externally applied nodal point loads in the configuration at iteration step, i

The basic approach in an incremental step-by-step solution is to assume that the solution for an iteration step, i is known and that the solution for the discrete iteration step ($i+1$) is required.

According to Bathe (1996), the vector \mathbf{F}_{n+1} is independent of the solid body deformation. The vector \mathbf{R}^i is approximated using a tangential stiffness matrix, \mathbf{K} which corresponds to the geometrical and material conditions at iteration step, i . The Newton-Raphson iteration procedure can be rewritten as (Lopes 2004):

$$\mathbf{K}\Delta\mathbf{u}_{n+1}^i = \mathbf{F}_{n+1} - \mathbf{R}^i \quad (2.70)$$

Where:

\mathbf{K} = The strain incremental tangential element stiffness matrix

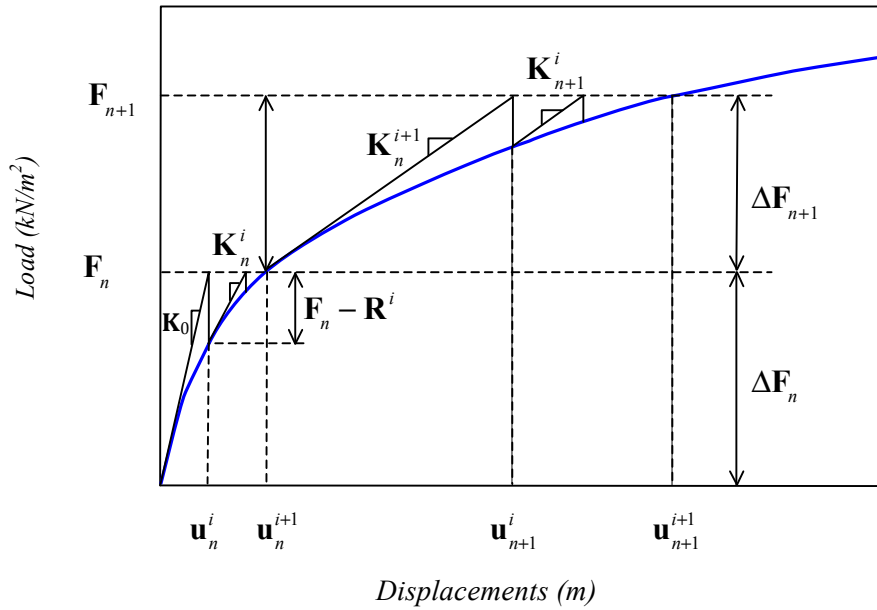
$\Delta\mathbf{u}_{n+1}^i$ = The vector of increments in the nodal point displacements

The Newton-Raphson iteration method requires that a new tangent stiffness matrix, \mathbf{K} to be calculated with each iteration as can be seen in Figure 2.1 (a). However for multiple degrees of freedom, this causes major computational cost per iteration due to the calculation and factorization of the tangent stiffness matrix, \mathbf{K} (Bathe 1996). Hence the modified Newton-Raphson iteration method can be used instead. In the modified Newton-Raphson iteration method, only the initial tangential stiffness matrix for each load level is calculated. This means that \mathbf{K} only needs to be constructed and reduced once for all iterations at a given load level. The modified Newton-Raphson iteration method involves fewer stiffness reformations than the full version and bases the tangential stiffness matrix update on an accepted equilibrium configuration, but it also needs more iteration numbers, as shown in Figure 2.1.

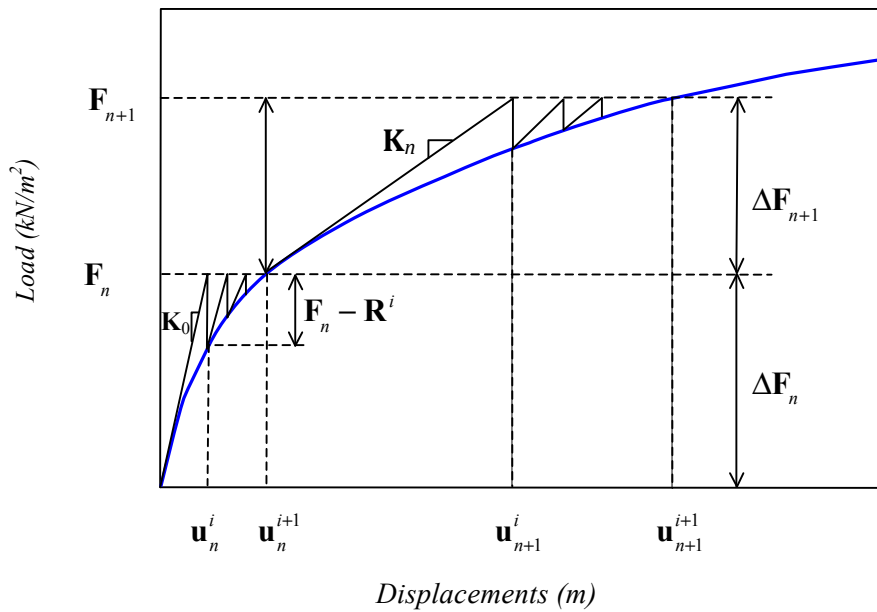
Once the matrix \mathbf{K} is determined, the approximation of displacements, $\Delta\mathbf{u}_{n+1}^i$ at the next iteration step ($i+1$) can be determined from (Lopes 2004):

$$\Delta\mathbf{u}_{n+1}^i = \mathbf{K}^{-1}(\mathbf{F}_{n+1} - \mathbf{R}^i) \quad (2.71)$$

Where \mathbf{u}_{n+1}^i and \mathbf{u}_{n+1}^{i+1} are vectors of nodal points displacements.



(a) Full Newton-Raphson iteration



(b) Modified Newton-Raphson iteration

Figure 2.1: Newton-Raphson iteration for the solution of a single degree of freedom system (Cook 1995)

The resulting nodal displacements vector obtained from Equation (2.71) will then be added into the displacement vector of the previous iteration step, \mathbf{u}_{n+1}^i :

$$\mathbf{u}_{n+1}^{i+1} = \mathbf{u}_{n+1}^i + \Delta\mathbf{u}_{n+1}^i \quad (2.72)$$

Where the out of balance load vector $\mathbf{F}_{n+1} - \mathbf{R}^i \neq 0$ means that element stress is not yet in equilibrium. Therefore an increment of the nodal point displacements is required. This updating of the nodal point displacements in the iteration is continued until the out-of-balance loads and incremental displacements are small or converged, meaning that $\mathbf{F}_{n+1} - \mathbf{R}^i = 0$. The convergence criteria is also written as Equation (2.68) or as given by Lopes (2004):

$$\frac{|\mathbf{F}_{n+1}^i - \mathbf{F}_n^i|}{|\mathbf{F}^0|} \leq \epsilon \quad (2.73)$$

The iteration is done until the convergence criterion is satisfied.

3 FLUID FLOW AND HEAT TRANSFER ANALYSIS

3.1 INTRODUCTION

A porous medium may deform under the act of external forces due to loading and pressure, e.g. from fluid-structure interaction and from internal pressure developing from pore fluid or chemical reactions like alkali-aggregate reactivity. The porous medium consists of different phases of continua, namely the skeleton, the pore fluid and for unsaturated cases, the pore gas. In considering the heat and mass transfer in porous medium, the balance equations for mass, linear momentum and energy need to be established. From these equations, a spatial and temporal discretization can be developed, allowing us to solve this problem with the finite element analysis. Numerous descriptions of heat and fluid transfer can be found in literature, some of which include Meyer (1971), Reddy and Gartling (1994), Lewis (2004) and Kythe (2004). This chapter presents the fundamental equations for heat and fluid transfer analysis using the Navier-Stokes equations, the penalty method for the fluid pressure field, and the constitutive equations for thermal stresses and strains.

3.2 CONSERVATION EQUATIONS FOR FLUID FLOW AND HEAT TRANSFER ANALYSIS

At the macroscale, concrete can be assumed as a homogeneous solid material. When exposed to temperature boundary conditions, thermal distribution in the concrete structure can be modeled as conductive heat transfer. However, when the concrete is modeled at a finer scale, one can see that concrete is actually a porous medium consisting of aggregates, pores and the cementitious matrix, making it a heterogeneous material that is influenced by pore pressure and fluid transfer.

Two main boundary conditions for heat transfer problems are stated by the Dirichlet boundary conditions in which the temperature on the boundaries is known, and the heat flux boundary condition which is stated by the Neumann boundary condition. Assume a porous medium as a domain that consists of two regions, a solid region and a fluid region with the domain $\Omega = \Omega_s \cup \Omega_f$ where s stands for solid and f stands for fluid. The porous medium is subjected to thermal boundary conditions of either temperature at the fluid surface or heat flux at the solid surface throughout the whole region enclosing the heated area. The boundary conditions for heat conduction are stated as (Lewis 2004):

$$\text{Dirichlet or essential boundary condition: } T = \hat{T}(s, t) \quad \text{on } \Gamma_T \quad (3.1)$$

$$\text{Neumann or natural boundary condition: } \left(k_{ij} \frac{\partial T}{\partial x_j} \right) n_j = q(s, t) \quad \text{on } \Gamma_q \quad (3.2)$$

Where t represents time, k_{ij} is the thermal conductivity coefficient, Γ_T is the temperature surface, s is the coordinate along the boundary, n_i is the outward unit normal to the boundary, and q is the heat flux at the surface, Γ_q .

In cases where convective heat transfer are being considered, the boundary condition falls into the Neumann boundary condition with an additional term added into Equation (3.2) such as the following:

$$\text{Neumann or natural boundary condition: } \left(k_{ij} \frac{\partial T}{\partial x_j} \right) n_j + q_c = q(s, t) \quad \text{on } \Gamma_q \quad (3.3)$$

The parameter q_c in Equation (3.3) is the convective component and is given by:

$$q_c = k_c(s, T, t)(T - T_c) \quad (3.4)$$

The term T_c is the sink temperature for convective heat transfer, and k_c is the convective heat transfer coefficient that depends on the boundary location, temperature and time. In heat conduction problems, the initial conditions are in the first-order term and needs to be specified all over the domain, Ω . In transient convective heat flow cases, initial conditions can be initiated from a known steady state temperature and velocity distribution. The dependent variables must be known for all \mathbf{x} at $t=0$ and must satisfy the basic conservation equations (Gartling 1994).

3.2.1 Conservation of Mass

According to the theory of porous media, an unsaturated porous medium is formed by the concrete skeleton with pore fluid and gas occupying the porous space. If the constituents are homogenized over a Representative Elementary Volume (REV), the total constituents, ϕ can be summed up by $\phi = \phi^s + \phi^f + \phi^g$ with ϕ^s , ϕ^f and ϕ^g representing the skeleton, fluid and gas constituents respectively. Lewis (1998) stated that any constituent ϕ^π could be represented by the volume fraction, ϕ^π :

$$\phi^\pi(\mathbf{X}^\pi, t) = \frac{dV^\pi}{dV} = \frac{1}{dV} \int \gamma^\pi(\mathbf{x}^\pi, t) dV_m \quad (3.5)$$

Where t represents time, \mathbf{x}^π denotes the position vector that represents the centre of a REV in a global coordinate system, \mathbf{X}^π denotes the initial reference configuration point, dV_m is the microscopic volume element, and dV^π is the average volume element of the π th constituent within a REV. The term γ in Equation (3.5) is the phase distribution function that must satisfy:

$$\gamma^\pi(\mathbf{x}^\pi, t) = \begin{cases} 1 & \text{for } \mathbf{x}^\pi \in dV^\pi \\ 0 & \text{for } \mathbf{x}^\pi \in dV^\alpha \quad \pi \neq \alpha \end{cases} \quad (3.6)$$

Where $\mathbf{x}^s = \mathbf{x}' + \mathbf{X}^s$ is the current position of the microscopic volume element, dV_m with \mathbf{x}' being the displacement of the material. The term dV^α is the volume element that is occupied by any constituent ϕ^α within the volume element, dV .

The degree of fluid or gas saturation, s^π in concrete pore space that is partially saturated with gas and fluid is given by:

$$s^\pi = \frac{dV^\pi}{dV^f + dV^g} \quad (3.7)$$

The volume fraction for solid can be written as:

$$\phi^s = 1 - \phi^v \quad (3.8)$$

Where ϕ^v represents the porosity and is determined from $\phi^v = \frac{dV^f + dV^g}{dV}$ for unsaturated material. The volume fraction for water is written as:

$$\phi^f = \phi^v s^f \quad (3.9)$$

The volume fraction for gas is written as:

$$\phi^g = \phi^v s^g \quad (3.10)$$

Where the sum of the volume fraction is stated by $\sum_{\pi=1}^i \phi^\pi = 1$.

The material density, ρ^π of a given phase is defined by the local mass, dm^π of the average volume element of the π th constituent, dV^π . The partial density, ρ^π as given by Bangert (2004) is stated as:

$$\rho^\pi = \frac{dm^\pi}{dV^\pi} \quad (3.11)$$

$$\rho^\pi = \frac{dm^\pi}{dV} = \frac{dV^\pi}{dV} \frac{dm^\pi}{dV^\pi} = \phi^\pi \rho^\pi$$

Lewis (1998) defined that the law of conservation of mass or the continuity equation for a multiphase fluid is represented by the local rate of change of mass in a fixed region is zero and mathematically written in the Eulerian description as:

$$\frac{\partial \rho^\pi}{\partial t} + \rho^\pi \operatorname{div} \mathbf{V}^{\alpha\pi} = \rho^\pi e^\pi(\rho) \quad (3.12)$$

Where $\mathbf{V}^{\alpha\pi}$ is the mass-averaged velocity of the material in the phase, π , and α is a phase under consideration within a phase π , and $\rho^\pi e^\pi(\rho)$ represents the exchange term for density.

If the macroscopic densities for solid, fluid and gas are ϱ^s , ϱ^f and ϱ^g respectively, according to Equation (3.12) and assuming that the mass exchange between solid and fluid are negligible and the pore gas compressible, hence from the Eulerian description, with the terms \mathbf{V}^s , \mathbf{V}^f and \mathbf{V}^g denoting the velocity of the skeleton, fluid and gas respectively, the mass balance equation for the skeleton from Equation (3.12) becomes:

$$\frac{\partial [\phi^s \varrho^s]}{\partial t} + \operatorname{div}(\phi^s \varrho^s \mathbf{V}^s) = 0 \quad (3.13)$$

And the mass balance equations for pore fluid and gas are defined as:

$$\frac{\partial [\phi^f]}{\partial t} + \operatorname{div}(\phi^f \mathbf{V}^f) = 0 \quad (3.14)$$

$$\frac{\partial [\phi^g \varrho^g]}{\partial t} + \operatorname{div}(\phi^g \varrho^g \mathbf{V}^g) = 0 \quad (3.15)$$

Assuming rapid change for pore fluid transfer and for homogenous cases where the volume fraction, ϕ^π can be neglected, the first term in Equation (3.14) can be omitted and therefore the mass balance equation for fluid is defined as:

$$\frac{\partial V_i}{\partial x_i} = 0 \quad (3.16)$$

Where $i = 1, 2, 3$ in the Cartesian coordinate system x_1 , x_2 and x_3 .

The development of the weak variational formulation follows the procedure outlined in Chapter Two, where the equation is multiplied with a weight function w_1 and then integrated over the element domain, Ω . The weighted integral statements over an element domain Ω of Equation (3.16) as given by Reddy (1994) is stated below as:

$$\int_{\Omega} w_1 \left[\frac{\partial V_i}{\partial x_i} \right] d\Omega = 0 \quad (3.17)$$

The term w_1 in Equation (3.17) is taken as the weight function. Reddy also stated that no integration-by-parts are used in the conservation of mass equation because no relaxation of differentiability on V_i can be accomplished.

3.2.2 Conservation of Linear Momentum

The law of conservation of linear momentum or Newton's second law of motion states that the total force acting on a material region is equal to the rate of change of linear momentum for the material:

$$\rho \frac{\partial \mathbf{V}}{\partial t} = -\nabla \sigma + \mathbf{F} \quad (3.18)$$

Where σ is the Cauchy stress tensor, ρ is the material density, \mathbf{V} is the fluid velocity and \mathbf{F} is the body force vector measured per unit mass. Equation (3.18) is known as the Navier equation.

Adapting the equation for incompressible flow of Newtonian fluids, we get (Mikelic 2003):

$$\rho \frac{\partial \mathbf{V}}{\partial t} + \rho(\mathbf{V}\nabla\mathbf{V}) = -\nabla \sigma + \mu_f \Delta \mathbf{V} + \mathbf{F} \quad (3.19)$$

Here, μ_f is the dynamic viscosity of fluid and the second term in the equation represents convection, which can be omitted if convection is not considered in the problem. Equation (3.19) is an adapted version of Equation (3.18) and is known as the Navier-Stokes equation.

For fluid transfer influenced by temperature, an additional term is added into the equation to accommodate for density change. This term is referred to as the Boussinesq approximation. Hence the body force vector \mathbf{F} in Equation (3.19) is represented by:

$$\mathbf{F} = \rho_0 \mathbf{g} \beta_T (T - T_0) \quad (3.20)$$

Where ρ_0 is the initial material density, T is the temperature with T_0 being the initial temperature, β_T represents the volumetric coefficient of thermal expansion of the fluid and \mathbf{g} represents gravity. Since gravity only influences the x_2 direction, hence \mathbf{g} is only added into the x_2 direction, while the values for \mathbf{g} in other directions are taken as zero.

The Boussinesq approximation also allows fluid density, ρ to vary with temperature, Reddy (1994) stated that the Boussinesq term could only be added into the body force term, which is in the right-hand side of the momentum equation. The densities in all other situations are assumed to be of the reference state ρ_0 . Adding the Boussinesq approximation into the Navier-Stokes equation in (3.19) and rewriting the equation in Cartesian coordinates, we obtain:

$$\begin{aligned} \rho_0 \frac{\partial V_i}{\partial t} + \rho_0 \left(V_j \frac{\partial V_i}{\partial x_j} \right) = \frac{\partial}{\partial x_j} \left[-P \delta_{ij} + \mu_{f,e} \left(\frac{\partial V_i}{\partial x_j} + \frac{\partial V_j}{\partial x_i} \right) \right] + \\ \rho_0 g_i \beta_T T_0 - \rho_0 g_i \beta_T (T - T_0) \end{aligned} \quad (3.21)$$

In developing the weak forms, the nonzero terms will be moved to one side of the equality and the resulting equations will be multiplied with a weight function w_2 and then integrated over the element domain Ω . The weighted integral statements are then reduced to weak statements by integration-by-parts to transfer the differentiation from the dependent variable V_i , P and T to the test function w_2 . This step also yields boundary terms that determine the nature of the essential and natural boundary conditions for the problem. The weak variational form for the conservation of momentum law can be stated as (Reddy 1994):

$$\begin{aligned} w_2 \int_{\Omega} \left[\rho_0 \left(\frac{\partial V_i}{\partial t} + V_j \frac{\partial V_i}{\partial x_j} \right) + \frac{\partial}{\partial x_j} \left(P \delta_{ij} - \mu_f \left(\frac{\partial V_i}{\partial x_j} + \frac{\partial V_j}{\partial x_i} \right) \right) - \rho_0 g_i \beta_T T_0 + \rho_0 g_i \beta_T (T - T_0) \right] d\Omega \\ - \oint_{\Gamma} w_2 T_i ds = 0 \end{aligned} \quad (3.22)$$

With the boundary conditions stated as:

$$\begin{aligned}
 T_i = \mu_f & \left[2 \frac{\partial V_1}{\partial x_1} n_{x1} + \left(\frac{\partial V_1}{\partial x_2} + \frac{\partial V_2}{\partial x_1} \right) n_{x2} + \left(\frac{\partial V_1}{\partial x_3} + \frac{\partial V_3}{\partial x_1} \right) n_{x3} \right] + (-P n_{x1}) + \\
 \mu_f & \left[\left(\frac{\partial V_2}{\partial x_1} + \frac{\partial V_1}{\partial x_2} \right) n_{x1} + 2 \frac{\partial V_2}{\partial x_2} n_{x2} + \left(\frac{\partial V_3}{\partial x_1} + \frac{\partial V_1}{\partial x_3} \right) n_{x3} \right] + (-P n_{x2}) + \\
 \mu_f & \left[\left(\frac{\partial V_3}{\partial x_1} + \frac{\partial V_1}{\partial x_3} \right) n_{x1} + \left(\frac{\partial V_3}{\partial x_2} + \frac{\partial V_2}{\partial x_3} \right) n_{x2} + 2 \frac{\partial V_3}{\partial x_3} n_{x3} \right] + (-P n_{x3})
 \end{aligned} \tag{3.23}$$

3.2.3 Conservation of Energy

Conductive heat transfer occurs when interaction of adjacent molecules due to a temperature gradient within a solid region generates thermal energy. The interaction will continue as long as thermal equilibrium has not been reached. Conductive heat transfer abides to the Fourier's Law, which states that the heat flux transferred throughout a material is directly proportional to the negative gradient of the temperature and to the area of the section at right angles to the direction of the transfer. This is shown in Equation (3.24), where the local heat flux, \mathbf{q} is equal to the product of the thermal conductivity coefficient, \mathbf{k} and the negative local temperature gradient, $-\nabla T$.

$$\mathbf{q} = -\mathbf{k} \text{ grad } T \tag{3.24}$$

The two types of convective heat transfer phenomena are: the natural convection, which occurs when heat is transferred by fluid circulation due to buoyancy from the density changes induced by heating and forced convection, where heat is transferred due to the movement in the fluid or gas that results from other forces like a pump. Since the convective heat transfer process depends directly on the motion of a fluid medium, the Navier-Stokes and the advection-diffusion equation that describes thermal energy transport must be considered in the development of a computational scheme.

The law of conservation of energy or the first law of thermodynamics states that the rate of the total energy is equal to the sum of the rate of work done by applied forces and the change of heat content per unit time:

$$(\rho_0 C_v)_e \left(\frac{\partial T}{\partial t} + \mathbf{V} \nabla T \right) = \nabla (k_e \nabla T) + Q \quad (3.25)$$

Where C_v is the fluid specific heat at constant volume and Q is the rate of heat generation. If the domain in consideration is solid, Ω_s , the second term in the left-hand side of Equation (3.25) is omitted for a conductive heat transfer solution.

In developing the weak forms, the nonzero terms will be moved to one side of the equality and the resulting equations will be multiplied with a weight function w_3 and then integrated over the element domain Ω . The weighted integral statements are then reduced to weak statements by integration-by-parts to transfer the differentiation from the dependent variable V_i and T to the test function w_3 . The weak variational form for the conservation of momentum law can be stated as (Reddy 1994 and Gartling 1994):

$$w_3 \int_{\Omega} \rho_0 C_v \left(\frac{\partial T}{\partial t} + \left(V_1 \frac{\partial T}{\partial x_1} + V_2 \frac{\partial T}{\partial x_2} + V_3 \frac{\partial T}{\partial x_3} \right) \right) + \left(\frac{\partial}{\partial x_1} k_{11} \frac{\partial T}{\partial x_1} + \frac{\partial}{\partial x_2} k_{22} \frac{\partial T}{\partial x_2} + \frac{\partial}{\partial x_3} k_{33} \frac{\partial T}{\partial x_3} - Q \right) dV - \oint_{\Gamma} w_3 q_n ds = 0 \quad (3.26)$$

For the energy equation, the boundary conditions can be stated as (Reddy 1994):

$$q_n = k_{11} \frac{\partial T}{\partial x_1} n_{x1} + k_{22} \frac{\partial T}{\partial x_2} n_{x2} + k_{33} \frac{\partial T}{\partial x_3} n_{x3} \quad (3.27)$$

The values for thermal conductivity coefficients are only taken as k_{ii} for isotropic material while anisotropic material will have an additional term of k_{ij} .

3.3 POISSON'S PRESSURE EQUATION

Another method to solve for the fluid pressure in a porous media is to use the Poisson's pressure equation. Badia (2008) suggested that instead of the continuity equation and the classical Navier-Stokes equation, one might also opt for the use of the

Poisson's pressure equation together with the Navier-Stokes equation. The Poisson's pressure equation is a method for determining the pore fluid pressure distribution and is given as:

$$\nabla^2 P = \nabla \cdot (\mathbf{F} + \nu \nabla^2 \mathbf{V} + \mathbf{V} \nabla \mathbf{V}) \quad (3.28)$$

Where ν is the Poisson's ratio.

Here, known values of velocities are substituted into the momentum equation in (3.28), which results in the equation being expressed in terms of pressure where a residual will be developed according to Reddy (1994) as:

$$\mathbf{R} \equiv M_1 \mathbf{e}_1 + M_2 \mathbf{e}_2 + M_3 \mathbf{e}_3 \quad (3.29)$$

With M_i being the components of the momentum equation and \mathbf{e}_i is the unit vector along the x_i direction.

The momentum equation M_i is written as:

$$M_i = \rho_0 \left(\frac{\partial V_i}{\partial t} + V_j \frac{\partial V_i}{\partial x_j} \right) - \frac{\partial}{\partial x_j} \left[-P \delta_{ij} + \mu_f \left(\frac{\partial V_i}{\partial x_j} + \frac{\partial V_j}{\partial x_i} \right) \right] + \rho_0 F_i \quad (3.30)$$

From Equation (3.30), the only unknown variable is the variable P , while the velocity, V_i has been determined from a previous iteration. Equation (3.30) integrated over an element with respect to P can be written as (Reddy 1994):

$$\int_{\Omega} M_i \frac{\partial M_i}{\partial P} d\Omega = 0 \quad (3.31)$$

Substituting $P = \sum_{l=1}^L \phi_l P_l$ into Equation (3.31):

$$\int_{\Omega} M_i \frac{\partial \phi_l}{\partial x_i} d\Omega = 0 \quad (3.32)$$

Equation (3.32) represents the l th equation of the system of L equations for the nodal values $P_1, P_2, P_3, \dots, P_L$ (Reddy 1994). In matrix form it can be written as:

$$\mathbf{K} \mathbf{P} = \mathbf{F} \quad (3.33)$$

With:

$$K_{lk} = \int_{\Omega} \frac{\partial \phi_l}{\partial x_i} \frac{\partial \phi_k}{\partial x_i} d\Omega, \quad F_l = \int_{\Omega} \frac{\partial \phi_l}{\partial x_i} M_i d\Omega \quad (3.34)$$

The vector \mathbf{F} consists of the body forces, inertial forces and viscous forces. Equation (3.33) is used to solve the Poisson's pressure equation in (3.28).

3.4 CONSTITUTIVE EQUATIONS FOR FLUID FLOW AND HEAT TRANSFER ANALYSIS

To include the effects of pore gas and fluid pressure in a porous media, the pressure values need to be deducted from the total stress tensor of the skeleton obtained from Equation (2.12), giving us the formulation for effective stress, σ for the solid phase at macroscopic level as:

$$\sigma = (1 - \eta) \sigma^s - \phi [s^g P^g + s^f P^f] \mathbf{1} \quad (3.35)$$

Where σ^s is the total stress tensor for the skeleton, ϕ is the volume fraction of a phase, $\mathbf{1}$ is the second order unit tensor and $P^s = s^g P^g + s^f P^f$ is the average pressure of fluid and gas at the surrounding matrix.

Lewis (1998) introduced the hypothesis of incompressible gas, meaning that gas will not undergo deformation from P^s , hence the volume fraction term is negligible, and when considering only pore fluid pressure, Equation (3.35) becomes:

$$\sigma = \sigma^s - P^f \mathbf{1} \quad (3.36)$$

To include thermal stress in the constitutive equation, once the temperature distribution throughout a medium is known, its influence on the static finite element analysis can be determined.

Thermal strains can be implemented in the form of the initial strain into the system such as in the following:

$$\sigma = \mathbf{C}(\varepsilon - \varepsilon^{th}) - P^f \mathbf{1} \quad (3.37)$$

Where σ is the stress tensor, ε is the total strain tensor, ε^{th} is the initial thermal strain tensor and \mathbf{C} is the material properties matrix.

Lund (2002) and Mulligan (1988) stated that the total thermal strain increment could be summed up over the current and history temperature range:

$$\varepsilon_{ij}^{th} = \left[\int_{T_0}^T \alpha_T (T - T_0) \right] \delta_{ij} \quad (3.38)$$

The post-computation of the thermoelastic strain starts with the iteration of Equation (3.38), resulting in thermal strain values, ε^{th} . The numerical solution of the equation for temperature $T + dT$ can be solved using the Backward Euler method:

$$\varepsilon_{ij}^{th}(T + dT) = \varepsilon_{ij}^{th}(T) + \alpha_T (T + dT) dT \delta_{ij} \quad (3.39)$$

Where α_T is a thermal expansion coefficient matrix, T is the temperature at a given point and T_0 is the temperature at which the structure is free of thermally induced strain.

In stress calculation, thermal strains cannot be merged directly into the mechanical strains. Lund (2002) explained that this is because the structural boundary conditions and internal resistance of the object needs to be considered. Therefore the thermally induced strains, ε^{th} are added into the consistent global nodal force vector \mathbf{F}^{th} :

$$\mathbf{F}^{th} = \int_{\Omega} \mathbf{B}^T \mathbf{C} \varepsilon^{th} d\Omega \quad (3.40)$$

Where \mathbf{B} is the strain-displacement matrix and \mathbf{C} is the elastic matrix of the mechanical properties. This nodal force vector will produce unrestraint response due to heating (Grill 1979) and is added to the mechanical nodal force vector when solving the static equilibrium equation $\mathbf{K}\mathbf{u} = \mathbf{F}$ with \mathbf{u} representing the vector of nodal displacements:

$$\mathbf{K}\mathbf{u} = \mathbf{F}^{mech} + \mathbf{F}^{th} \quad (3.41)$$

As outlined in Chapter Two, \mathbf{K} is the global stiffness matrix, \mathbf{u} is the nodal displacement vector and \mathbf{F} is the global consistent nodal force vector consisting of both

mechanical loads \mathbf{F}^{mech} which includes the hydrostatic pressure and the consistent global nodal force vector \mathbf{F}^{th} due to thermally induced strains (Lund 2002), with:

$$\mathbf{F}^{mech} = \int_{\Omega} \mathbf{B}^T \mathbf{C} \boldsymbol{\varepsilon} d\Omega \quad (3.42)$$

The term $\boldsymbol{\varepsilon} = \mathbf{B}\mathbf{u}$ is the total strain tensor.

3.5 FINITE ELEMENT IMPLEMENTATION

3.5.1 Spatial Discretization for Fluid Flow and Heat Transfer Equations

The Navier-Stokes equation can be approximated using a mixed finite element method or also called the velocity-pressure model because velocity variables are mixed with pressure in a single simulation. It can also be coupled to the temperature equation when necessary. For three-dimensional problems, the model will have five unknowns which include V_1 , V_2 , V_3 , P and T . Suppose that the dependent variables V_i , P and T are approximated by expansions in the form given by Reddy (1994) as:

$$V_i(\mathbf{x}, t) = \sum_{n=1}^N \psi_n(\mathbf{x}) V_i^n(t) = \boldsymbol{\Psi}^T \mathbf{V}_i \quad (3.43)$$

$$P(\mathbf{x}, t) = \sum_{l=1}^L \phi_l(\mathbf{x}) P_l(t) = \boldsymbol{\Phi}^T \mathbf{P} \quad (3.44)$$

$$T(\mathbf{x}, t) = \sum_{m=1}^M \theta_m(\mathbf{x}) T_m(t) = \boldsymbol{\Theta}^T \mathbf{T} \quad (3.45)$$

The terms $\boldsymbol{\Psi}$, $\boldsymbol{\Phi}$ and $\boldsymbol{\Theta}$ are vectors of interpolation functions for vectors of nodal values of velocity components, \mathbf{V} , pressure, \mathbf{P} and temperature, \mathbf{T} . The weight functions w_i in Equations (3.17), (3.22) and (3.26) represent $w_1 = \phi_l$, $w_2 = \psi_n$, $w_3 = \theta_m$ and will be equated to the interpolation functions used for \mathbf{V} , \mathbf{P} and \mathbf{T} .

Substituting Equations (3.43) to (3.45) into (3.17), (3.22) and (3.26) result in (Reddy 1994):

Conservation of mass:

$$-\left[\int_{\Omega} \Phi \frac{\partial \Psi^T}{\partial x_i} d\Omega \right] V_i = 0 \quad (3.46)$$

In matrix form, Equation (3.46) becomes:

$$-\mathbf{Q}^T \mathbf{V} = 0 \quad (3.47)$$

With:

$$\mathbf{Q} = \left[\int_{\Omega} \Phi \frac{\partial \Psi^T}{\partial x_i} d\Omega \right] \quad (3.48)$$

Conservation of momentum:

$$\begin{aligned} & \left[\int_{\Omega} \rho_0 \Psi \Psi^T d\Omega \right] \dot{V}_i + \left[\int_{\Omega} \rho_0 \Psi (\Psi^T V_j) \frac{\partial \Psi^T}{\partial x_j} d\Omega \right] V_i + \left[\int_{\Omega} \mu_f \frac{\partial \Psi}{\partial x_j} \frac{\partial \Psi^T}{\partial x_j} d\Omega \right] V_i \\ & + \left[\int_{\Omega} \mu_f \frac{\partial \Psi}{\partial x_j} \frac{\partial \Psi^T}{\partial x_i} d\Omega \right] V_j - \left[\int_{\Omega} \frac{\partial \Psi}{\partial x_i} \Phi^T d\Omega \right] P = - \left[\int_{\Omega} \rho_0 g_i \beta_T \Psi \Theta^T d\Omega \right] T \\ & + \left\{ \int_{\Omega} \rho_0 g_i \beta_T T_0 \Psi d\Omega \right\} + \left\{ \oint_{\Gamma} \Psi T_i ds \right\} \end{aligned} \quad (3.49)$$

In matrix form, Equation (3.49) becomes:

$$\underbrace{\mathbf{M}}_{\mathbf{M}_u} \dot{\mathbf{V}} + \underbrace{\mathbf{C}(\mathbf{V})\mathbf{V} + \mathbf{KV} - \mathbf{QP} + \mathbf{BT}}_{\mathbf{K}_u} = \underbrace{\mathbf{F}}_{\mathbf{F}} \quad (3.50)$$

$$\begin{bmatrix} \mathbf{M} & 0 & 0 & 0 \\ 0 & \mathbf{M} & 0 & 0 \\ 0 & 0 & \mathbf{M} & 0 \\ 0 & 0 & 0 & 0 \end{bmatrix} \begin{bmatrix} \dot{\mathbf{V}}_1 \\ \dot{\mathbf{V}}_2 \\ \dot{\mathbf{V}}_3 \\ \dot{\mathbf{P}} \end{bmatrix} + \begin{bmatrix} \mathbf{C}(\mathbf{V}) & 0 & 0 & 0 \\ 0 & \mathbf{C}(\mathbf{V}) & 0 & 0 \\ 0 & 0 & \mathbf{C}(\mathbf{V}) & 0 \\ 0 & 0 & 0 & 0 \end{bmatrix} \begin{bmatrix} \mathbf{V}_1 \\ \mathbf{V}_2 \\ \mathbf{V}_3 \\ \mathbf{P} \end{bmatrix}$$

$$+ \begin{bmatrix} 2\mathbf{K}_{11} + \mathbf{K}_{22} + \mathbf{K}_{33} & \mathbf{K}_{21} & \mathbf{K}_{31} & -\mathbf{Q}_1 \\ \mathbf{K}_{12} & \mathbf{K}_{11} + 2\mathbf{K}_{22} + \mathbf{K}_{33} & \mathbf{K}_{32} & -\mathbf{Q}_2 \\ \mathbf{K}_{13} & \mathbf{K}_{23} & \mathbf{K}_{11} + \mathbf{K}_{22} + 2\mathbf{K}_{33} & -\mathbf{Q}_3 \\ -\mathbf{Q}_1^T & -\mathbf{Q}_2^T & -\mathbf{Q}_3^T & 0 \end{bmatrix} \begin{bmatrix} \mathbf{V}_1 \\ \mathbf{V}_2 \\ \mathbf{V}_3 \\ \mathbf{P} \end{bmatrix} = \begin{bmatrix} \mathbf{F}_1(\mathbf{T}) \\ \mathbf{F}_2(\mathbf{T}) \\ \mathbf{F}_3(\mathbf{T}) \\ 0 \end{bmatrix}$$

With:

$$\begin{aligned} \mathbf{M} &= \left[\int_{\Omega} \rho_0 \Psi \Psi^T d\Omega \right], \quad \mathbf{C}(\mathbf{V}) = \left[\int_{\Omega} \rho_0 \Psi (\Psi^T V_j) \frac{\partial \Psi^T}{\partial x_j} d\Omega \right], \\ \mathbf{K} &= \left[\int_{\Omega} \mu_f \frac{\partial \Psi}{\partial x_i} \frac{\partial \Psi^T}{\partial x_j} d\Omega \right], \quad \mathbf{Q} = \left[\int_{\Omega} \frac{\partial \Psi}{\partial x_i} \Phi^T d\Omega \right], \\ \mathbf{B} &= \left[\int_{\Omega} \rho_0 \beta_T g_i \Psi \Theta^T d\Omega \right], \quad \mathbf{F}(\mathbf{T}) = \left\{ \int_{\Omega} \rho_0 g_i \beta_T T_0 \Psi d\Omega \right\} + \left\{ \oint_{\Gamma} \Psi T_i ds \right\} \end{aligned} \quad (3.51)$$

In situations where convective heat transfer is not being considered, the term $\mathbf{C}(\mathbf{V})$ in Equation (3.50) can be omitted.

Conservation of energy:

$$\begin{aligned} \left[\int_{\Omega} (\rho_0 C_v)_e \Theta \Theta^T d\Omega \right] \dot{T} + \left[\int_{\Omega} \rho_0 C_v (\Psi^T V_j) \frac{\partial \Theta^T}{\partial x_j} d\Omega \right] T + \left[\int_{\Omega} k_{ij} \frac{\partial \Theta}{\partial x_i} \frac{\partial \Theta^T}{\partial x_j} \right] T \\ = \left\{ \int_{\Omega} \Theta Q d\Omega \right\} + \left\{ \oint_{\Omega} \Theta q_n ds \right\} \end{aligned} \quad (3.52)$$

In matrix form, Equation (3.52) becomes:

$$\underbrace{\mathbf{N}\dot{\mathbf{T}}}_{\dot{\mathbf{M}}\mathbf{u}} + \underbrace{\mathbf{D}\mathbf{T} + \mathbf{L}\mathbf{T}}_{\mathbf{K}\mathbf{u}} = \underbrace{\mathbf{G}}_{\mathbf{F}} \quad (3.53)$$

With:

$$\begin{aligned} \mathbf{N} &= \int_{\Omega} (\rho_0 C_v)_e \Theta \Theta^T d\Omega, \quad \mathbf{L} = \int_{\Omega} k_{ij} \frac{\partial \Theta}{\partial x_i} \frac{\partial \Theta^T}{\partial x_j} d\Omega; \\ \mathbf{D}(\mathbf{V}) &= \int_{\Omega} \rho_0 C_v \Theta (\Psi^T \mathbf{V}_j) \frac{\partial \Theta^T}{\partial x_j} d\Omega, \quad \mathbf{G} = \int_{\Omega} \Theta Q d\Omega + \oint_{\Gamma} \Theta q_n ds \end{aligned} \quad (3.54)$$

Equations (3.50) and (3.53) need to be temporally discretized from the form of $\mathbf{M}\dot{\mathbf{u}} + \mathbf{K}\mathbf{u} = \mathbf{F}$ to $\mathbf{K}\mathbf{u} = \mathbf{F}$, which is also the form Equation (3.47) is in, before being able to solve it using the iteration methods explained in Section 2.5.1. The method of temporal discretization will be explained in the next section.

3.5.2 Temporal Discretization for Fluid Flow and Heat Transfer Equations

Temporal discretization is applied to equations for two reasons, the first reason being that the system is transient and hence to obtain a transient response, the equations from the above sections should be integrated with respect to time. The equations will be further approximated in time to obtain a set of algebraic equations in terms of nodal displacements to achieve a fully discretized model. The second reason is that coupled, nonlinear equations need to be linearized first before it can be solved iteratively. The solution method depends on the model, computational resources, the nonlinearity of the system and the strength of coupling between the equations.

The superposed dot in Equations (3.50) and (3.53) denotes the derivative of time, meaning that the equation $\mathbf{M}\dot{\mathbf{u}} + \mathbf{K}\mathbf{u} = \mathbf{F}$ must first be temporally discretized to $\mathbf{K}\mathbf{u} = \mathbf{F}$ before being solved with the finite element method. In this section, $\mathbf{M}\dot{\mathbf{u}} + \mathbf{K}\mathbf{u} = \mathbf{F}$ will be discretized using one of the most common time integration methods, which is the θ -parameter family of approximation. Changing the values of the parameter θ from 0 to 1 gives us different time approximation schemes as outlined below (Reddy 1994):

$\theta = 0$ The forward difference scheme (conditionally stable)

$\theta = 1/2$ The Crank-Nicholson scheme (unconditionally stable)

$\theta = 2/3$ The Galerkin scheme (unconditionally stable)

$\theta = 1$ The backward difference scheme (unconditionally stable)

In the θ -parameter family of approximation, it is assumed that within the limit of $0 \leq \mathbf{V} \leq t_{end}$ and time interval dt , the velocities and accelerations are allowed to linearly vary according to the backward difference approximation (Reddy 1994):

$$\dot{\mathbf{u}}^{n+1} = \frac{\mathbf{u}^{n+1} - \mathbf{u}^n}{dt} \quad (3.55)$$

Where $n+1$ denotes the iteration number and the superposed dot represents the rate of velocity change over change of time, dt .

Evaluating $\mathbf{M}\dot{\mathbf{u}} + \mathbf{K}\mathbf{u} = \mathbf{F}$ at the $(n+1)$ th time step and inserting Equation (3.55) into $\mathbf{M}\dot{\mathbf{u}} + \mathbf{K}\mathbf{u} = \mathbf{F}$ produces:

$$\mathbf{M}\left(\frac{\mathbf{u}^{n+1} - \mathbf{u}^n}{dt}\right) + \mathbf{K}\mathbf{u}^{n+1} = \mathbf{F}^{n+1} \quad (3.56)$$

For transient fluid analysis, the body force vector at the right-hand side of Equation (3.56) is added with the buoyancy terms. Hence vector \mathbf{F} is influenced by temperature. The hydrostatic pressure is also included at the right-hand side of the equation.

$$\mathbf{M}(\mathbf{u}^{n+1})\left(\frac{\mathbf{u}^{n+1} - \mathbf{u}^n}{dt}\right) + \mathbf{K}(\mathbf{u}^{n+1})\mathbf{u}^{n+1} = \mathbf{F}(\mathbf{T}^{n+1}) \quad (3.57)$$

From Equation (3.57), nonlinear fluid analysis has stiffness and mass matrices \mathbf{K} and \mathbf{M} with material properties that depend on the velocity distribution.

In the general nonlinear cases, the matrix problem presented in Equation (3.57) requires an iterative solution for \mathbf{u}^{n+1} within each time step. The linear case as in (3.56) can be solved without a nonlinear iteration. Modeling the fluid flow and heat transfer in this research uses the finite element method developed using the backward Euler difference scheme. The backward Euler method is an implicit method, meaning that we have to solve an equation to find a solution at every t^{n+1} . The advantage of implicit methods is that they are usually more stable for solving a stiff equation so that a larger step size dt can be used, and that there is no time restriction. Equation (3.55) now becomes (Reddy 1994):

$$\mathbf{u}^{n+1} = \mathbf{u}^n + dt\left[(1-\theta)\dot{\mathbf{u}}^n + \theta\dot{\mathbf{u}}^{n+1}\right], \quad 0 \leq \theta \leq 1 \quad (3.58)$$

Equation (3.58) is used by inserting it into any transient equation $\mathbf{M}\dot{\mathbf{u}} + \mathbf{K}\mathbf{u} = \mathbf{F}$ to transform an ordinary differential equation into a set of algebraic equations at time t^{n+1} :

$$\hat{\mathbf{K}}^{n+1}\mathbf{u}^{n+1} = \hat{\mathbf{F}}^{n,n+1} \quad (3.59)$$

Where:

$$\hat{\mathbf{K}}^{n+1} = \mathbf{M} + a_1 \mathbf{K}^{n+1} \quad (3.60)$$

$$\hat{\mathbf{F}}^{n,n+1} = dt(\theta \mathbf{F}^{n+1} + (1-\theta) \mathbf{F}^n) + (\mathbf{M} - a_2 \mathbf{K}^n) \mathbf{V}^n$$

$$a_1 = \theta dt, \quad a_2 = (1-\theta) dt \quad (3.61)$$

After assembling and the imposition of the boundary conditions, Equation (3.60) is solved at each time step for the nodal values u_j at time $t^n = (n+1)dt$. At time $t = 0$, the right-hand side of the equation is computed using the initial values \mathbf{u}_0 , and the vector \mathbf{F} is always known for both times t^n and t^{n+1} . This completes the development of the finite element model for a fluid flow and heat transfer problem.

4 ALKALI-SILICA REACTION

4.1 INTRODUCTION

ASR expansion in an affected concrete structure may happen rapidly and cause deformation to the structure well before its serviceability limit is reached, hence understanding the process is crucial. ASR deformation can be identified by a random network of crack patterns on its surface known as map cracking, leaching of the ASR gel and concrete spalling. The ASR process occurs when hydroxide ions in the pore solution interact with silica from the aggregates. Hydroxide ions, being alkaline in nature attack the reactive silica sites at the aggregate surface, producing a hydrophilic gel. This gel accumulates at the reaction sites and fills into adjacent voids, replacing the silica it consumed in producing the gel. When moisture diffuses into the affected concrete, this gel expands and migrates into the connecting porous medium resulting in an internal build up of tensile stresses in the matrix. This will eventually lower the concrete stiffness. The amount of pressure exerted by the ASR gel expansion varies depending on a number of factors which include the relative humidity, temperature, the type and proportions of reacting materials and gel composition. This chapter briefs on the ASR mechanisms and factors affecting its reactivity. The most known literatures on ASR are from Dent-Glasser and Kataoka (1981), Diamond (1981), Swamy (1992) and Larive (1998), which are all referred to in this thesis. Then, the fundamental equations for ASR modeling are outlined. Previous works for ASR simulation can be found from the works of Capra (1998), Ulm (2000), Bazant (2000), Bangert (2004) and Fairbairn (2004).



Figure 4.1: Map cracking due to ASR deterioration on a concrete wall (Stark 2008)

4.2 FACTORS INFLUENCING ASR

Alterations in the concrete mix have a significant impact on ASR. By changing the proportions of the constituents in a mix, the alkali and reactive silica contents, and the hydroxyl ion concentration resulting from cement hydration are also changed, which will in turn influence the ASR reaction rate. Mixing also determines concrete porosity, which has a direct influence on transport. External factors like temperature, relative humidity and external sources of constituents also affect the ASR process.

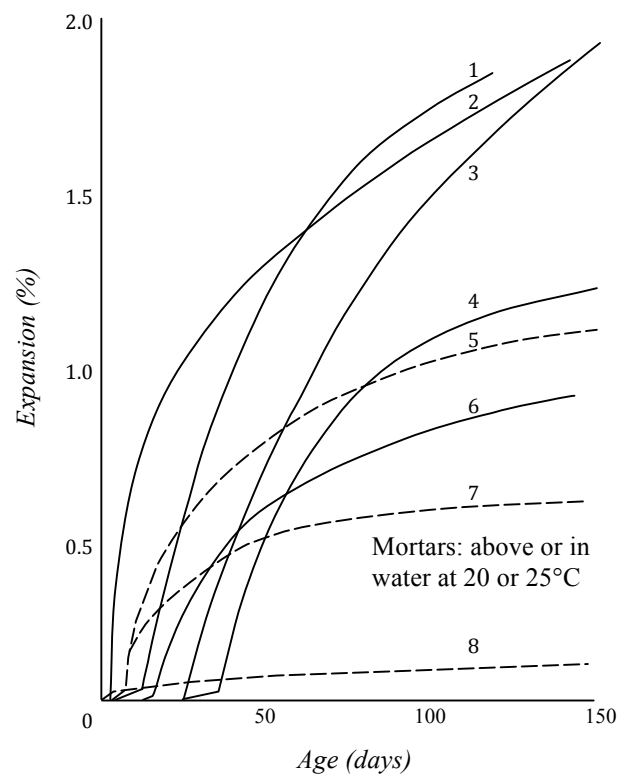
4.2.1 Alkali Content

A major contributor of alkali in concrete is the Portland cement. Cement hydration produces metal alkali sodium, potassium and calcium hydroxides in the pore solution, which concentrations depend on the type and alkalinity of the Portland cement used. Additional sources of alkali can also be released by aggregates that naturally contain alkali. Swamy (1992) explained that high alkali cements could produce a pH that range from 13.5 to 13.9, while low alkali cements produce a pH ranging from 12.7 to 13.1. The acid soluble content of Portland cement is calculated as the equivalent sodium oxide using the following formula as outlined by Hobbs (1988):

$$\begin{array}{rcccl}
 (\text{Na}_2\text{O})_e & \rightarrow & \text{Na}_2\text{O} & + & 0.658 \cdot \text{K}_2\text{O} \\
 \text{sodium oxide} & & \text{sodium oxide} & & 0.658 \times \text{potassium oxide} \\
 \text{equivalent} & & \text{weight percentage} & & \text{weight percentage}
 \end{array} \quad (4.1)$$

Previous researches on ASR, for instance by Stanton (1940) have discovered that the ASR process is only initiated if the alkali concentration in concrete is at a certain threshold value. He concluded from mortar bar tests conducted with cement content of over 600 kg/m^3 that expansion due to ASR does not occur when the cement acid soluble alkali content is less than 0.60% by mass, a threshold that is also recommended in the Hawkin's Report (1999). Kagimoto (2004) on the other hand, conducted NBRI tests on reactive aggregates and discovered that the threshold hydroxyl ion concentration required for ASR initiation varies depending on the aggregate and is set at 250 mmol/l for natural aggregates.

4.2.2 Silica Content



Reactive Rock	Alkali Content (kg/m^3)
1. Beltane opal, 4.5%	5.3
2. Beltane opal, 12%	9.8
3. V17 opaline rock, 5%	6.2
4. Beltane opal, 4.5%	4.5
5. A Danish flint, 20%	9.8
6. Schleswig-Holstein sandstone, 4%	4.6
7. Siliceous magnesium limestone, 10%	5.6
8. Thames Valley	15.5

Figure 4.2: Expansion produced by five aggregates containing opaline material (Hobbs 1988)

The alkali-silica reactivity depends on the stability of existing silica in the aggregates. Hobbs (1988) explained that under normal circumstances, stable silica has an ordered arrangement of silicon oxygen tetrahedra making it more resistant to alkali attack while reactive silica has a random network of tetrahedra with voids between the groups of molecules making it susceptible to reaction. Minerals that are known for its reactive potency include silica minerals, opal, chalcedony and quartz, among others (Hobbs 1988). The graph in Figure 4.2 shows expansion results for silica from mortar bar tests. Different aggregates with different reactivity were used at different percentages. The curve using beltane opal, being highly reactive aggregates, tends to expand at a much faster and higher rate even with a lower alkali content compared to the less reactive aggregates, like the one from Thames Valley. This means that even a small quantity of reactive silica can deplete all metal alkali in the pore solution. Swamy (1992) agreed with this theory, having observed reports in certain cases that as little as 2% of reactive component causing severe distress to the concrete.

4.2.3 Relative Humidity

Water has dual role in the ASR process; firstly as a carrier of the alkali cations and hydroxyl ions and secondly, as a swelling agent for the ASR gel. Since all influencing constituents are still available in the initial state, ASR reaction rate is the highest at this point. Figure 4.3 shows the relationship between water content in gels at equilibrium as a function of relative humidity (Hobbs 1988). The resultant gel is hydrophilic in nature; hence it absorbs water and increases in volume which is what causes the gel to have its expansive characteristic. It was suggested by Grattan-Bellew (1989) that the optimum water/cement ratio for expansion of mortar bars containing alkali-reactive aggregates to be in the range of 0.4 to 0.6, depending on the physical and chemical properties of the aggregates. Experiments have also shown that a relative humidity of above 80% has a significant expansion effect due to ASR.

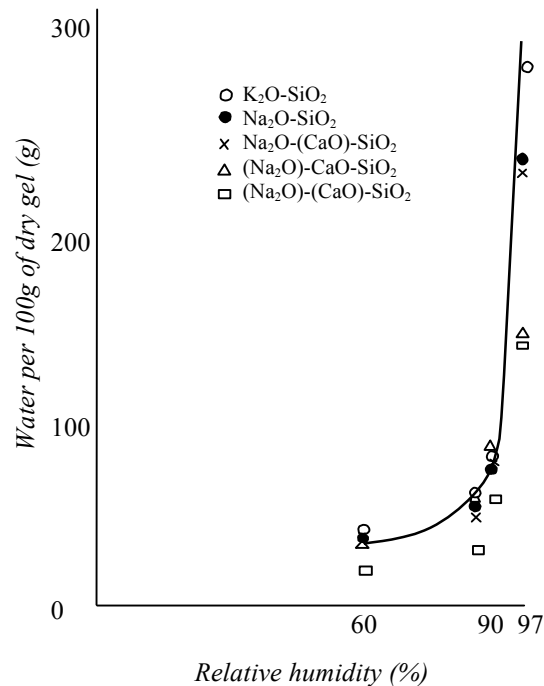


Figure 4.3: Relationship between water content in gels at equilibrium and relative humidity (Hobbs 1988)

4.2.4 External Sources of Reactants

The ASR process needs both alkali and hydroxide ions in order to react. However, the initial contents of the constituents are rarely enough to promote major expansions before either constituent depletes. Therefore ASR also depends on alkali obtained from other sources like mineral additions, mixing water and in cold climates, from deicing solutions. The Hawkin's Report (1999) suggested that if the external sources of alkali exceed 0.2 kg/m^3 of the concrete, it should be taken into account when calculating the total reactive alkali available. The age of the concrete during the time of introduction of the external sources of reactants also has an effect on the ASR process. Hobbs (1998) presented an example that exhibits this effect.

Figure 4.4 (a) shows that early exposure of the uncracked mortar to salt water causes large expansions, but lower than if the salt water was added into the mixing water instead. This could be due to the mortar being somewhat impervious in the initial stages due to its uncracked condition, making alkali migration into the reactive silica sites restricted. But when salt water was added into the mixing water, the mortar will have a higher content of alkali resulting from the hydration products, making the initiation of the ASR process faster and its reaction rate higher.

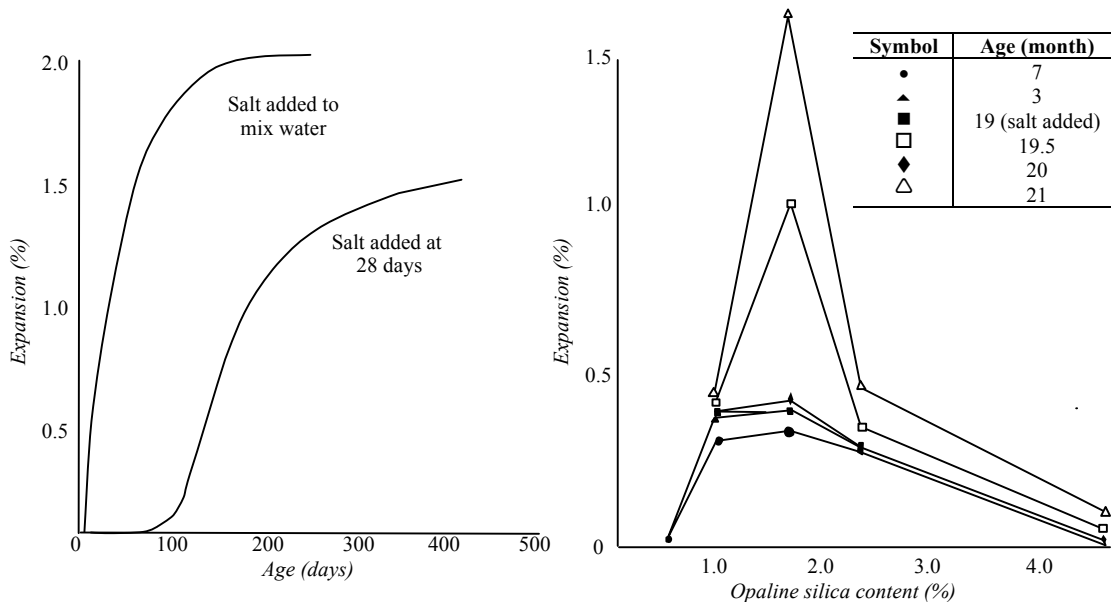


Figure 4.4 (a): Influence of sodium chloride on ASR expansion in mortars in water at 20°C (opaline silica reactive, 150-300µm); sodium oxide = 5.2 kg/m³, w/c = 0.41 and a/c = 2.75 (Hobbs 1988)

Figure 4.4 (b): Influence of salt added at 19 months on expansion due to ASR in concrete in water at 20°C (opaline silica reactive, 150-300µm); w/c = 0.41 and a/c = 2.75, sodium oxide ~5+2 kg/m³ (Hobbs 1988)

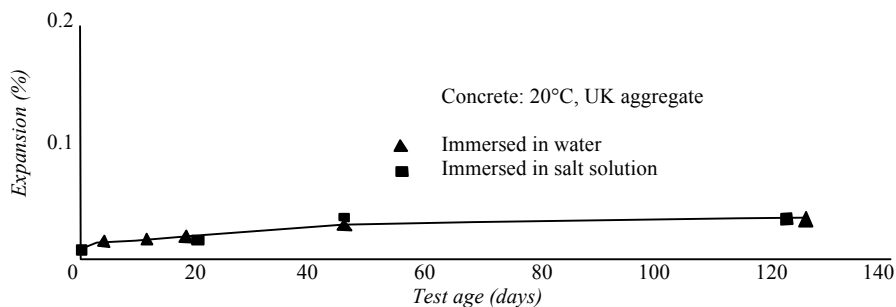


Figure 4.4 (c): Influence of salt on expansion; 150 mm cubes immersed in water for 14.5 years, dried for 6 months at 65% RH, 20°C, then placed either in water or a sodium chloride solution; expansion of cubes at 14.5 years: 0.2 to 0.3% (Hobbs 1988)

Figure 4.4 (b) shows the salt water being added to cracked mortar at 20 months. Hobbs (1988) explained that large increases in expansion were developed in mortars containing a pessimum proportion of reactive aggregates, while on the other hand low increases in expansion in mortars containing low opaline silica content were produced, proving that even with the additional alkali supplied by the salt water, the reaction can continue only if the amount of reactive silica is also available. Figure 4.4 (c) shows that when salt water is applied to cracked mortar at the age of 15 years, no measurable increase in expansion was observed, perhaps because old concrete already has excess alkali or all the silica has already depleted.

4.2.5 Concrete Permeability and Porosity

Porosity and permeability control the movement and storage of fluid and air in concrete. Although the material packing, shape and sorting influence porosity and permeability, they both have different definitions. Porosity is the ratio of the volume of voids in the concrete to the total volume of the concrete itself. Permeability is a measurement of the ease with which a liquid or gas is able to travel through a porous solid material. Hence permeability of concrete also depends on the porosity. Although the concrete may be highly porous, if the voids are not interconnected, then the pore fluid is not free to flow, making the concrete impermeable. Permeability is often directional in nature. Pores can be filled with pore solution or entrained air. The availability of air voids enables the gel to migrate through undamaged concrete to fill air voids, hence reduce the risk of cracking. Porosity and permeability of the concrete also influences the absorption of alkali from external sources.

4.2.6 Temperature

Temperature influences the rate of water absorption by the ASR gel. Diamond, Barneyback Jr. and Struble (1981) reported that ASR reaction and expansion rates are initiated early and develop rapidly when subjected to high temperature. However, as the reaction continues both reaction and expansion rates slow down as can be seen in Figure 4.5. When subjected to lower temperature, the reaction and expansion rates are slower in the initial state and continue until it reaches the same level of expansion as for the higher temperature. Hobbs (1988) explained that this effect might be due to the migratory characteristics of the ASR gel for lower temperature having slower development rates, having more time to disperse into the porous medium without exerting pressure. On the other hand, gel at higher temperature is produced and dispersed throughout the porous medium rapidly and exerts pressure to the surrounding matrix. However, at a lower temperature the expansion exceeds the expansion attained at higher temperature. Hobbs (1988) suggested that the gel reaches its maximum swelling pressure at a certain stage and at lower temperature, the period at which the gel exerts its maximum pressure is prolonged, causing higher expansions. He also proved from tests on a concrete dam that rapid and drastic variation of

temperature due to seasonal changes is very small and only affects the surface of the structure since change in concrete due to temperature is slow and limited.

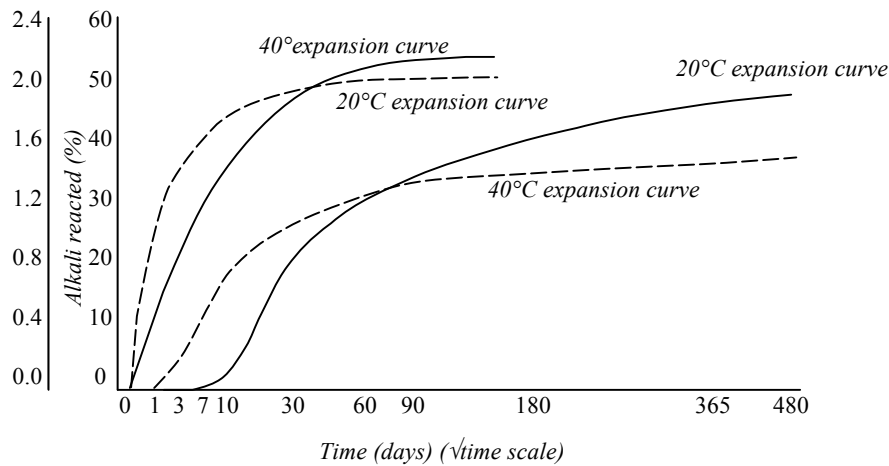
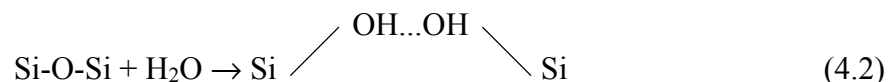


Figure 4.5: Comparison of reaction parameter curves versus expansion curves for sealed mortars specimens with 8% beltane opal at 20°C and 40°C (Hobbs 1988)

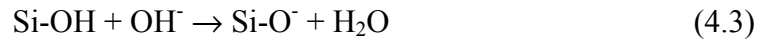
4.3 THE CHEMISTRY OF ASR

The physical deterioration caused by ASR expansion is a consequence of a chemical reaction between the constituents of concrete like aggregate, cement and water under external influences like relative humidity and temperature. There are many diverging theories on ASR, but so far the explanation given by Dent-Glasser and Kataoka (1981) has been widely accepted. They suggested that exposure to alkali subject reactive silica to initial depolymerization which will weaken the silica bonds. The positive charges resulting from the depolymerization then react with the metal alkali hydroxide ions, resulting in a calcium-silicate-hydrate (C-S-H) gel at the interfacial zone between the aggregate and cementitious matrix. This gel has the capability to imbibe water and ions like potassium, sodium and calcium, all byproducts of hydration, in order to maintain the ionic equilibrium.

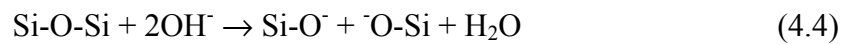
Swamy (1992) summarized that ASR occurs in three stages. The first stage is where hydroxyl ions react with Si-O-Si bonds to form silanol molecules. These silanol molecules being acidic in nature react with more hydroxyl ions:



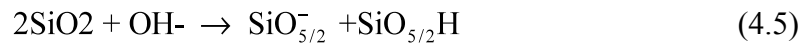
In the second stage, the silanol molecules react further with the available hydroxyl ions releasing more water into the system:



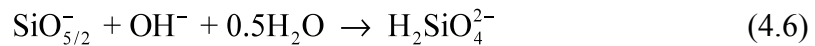
This produces a gel-like substance at the reaction site. The negatively charged Si-O⁻ attracts positive charges from sodium, potassium and calcium to diffuse into the gel to balance the charge, producing C-S-H, C-K-S-H or C-N-S-H gels (Dent-Glasser and Kataoka 1981). In the third stage, the disintegration of silica continues:



Garcia-Diaz, Riche and Bulteel (2004) on the other hand, consider two main stages in the ASR process. The first stage is the formation of the negatively charged Q₃ tetrahedron due to the breaking up of the siloxane bonds by the hydroxyl ions:



The second stage includes the dissolution of the Q₃ tetrahedrons due to the continued attack by hydroxyl ions to form Q₀ tetrahedrons, which are the silica ions:



Then, reaction between the Q₀ tetrahedron anions and the cations in the pore solution will precipitate into C-S-H, C-K-S-H or C-N-S-H gels formation.

This reaction will continue as long as the main reactants are available. Once either silica or alkali concentrations deplete, or when water is unavailable, the reaction ceases. However, reintroduction of alkali or silica and water from external sources will cause the reaction to commence provided there is excess silica or alkali in the matrix to begin with. The reaction will continue until physical equilibrium is achieved or when the supply of one of the reactants is fully consumed.

4.4 ASR MODELING CONSIDERATIONS

Two main aspects to be considered in ASR modeling is the kinetics of chemical reactions and the mechanical damage caused by the resulting expansion. The chemistry of ASR depends on the number of moles consumed from the disintegration of the weak siliceous bond and the number of moles of gel formed. The effects of ASR on the mechanical properties of concrete are on the compressive strength, tensile strength, flexural strength and modulus of elasticity. Li and Coussy (2004) developed a thermo-hydro-chemo-mechanical model to study the behavior of ASR affected concrete based on the Biot-Coussy theory on mechanics of reactive porous medium. They represented the solid skeleton successively with an elastic and plastic medium using the first-order law for gel formation and swelling.

Moranville-Regourd (1997) suggested that the use of thermodynamics as an irreversible process associated with the continuum damage theory will enable ASR deteriorated zones to be identified. Capra and Bournazel (1998) suggested that ASR gel composition is heterogeneous from one reactive site to another, depending on time and the initial content of silica and alkali. He wrote an equation for free linear expansion for alkali-aggregate reaction, ε^a that contains the principal parameters for the representation of chemical reaction affinity between the reactants and products, A , temperature, T , relative humidity, H , and from structural point of view, function of stress, F_σ .

$$\varepsilon^a = \varepsilon^a(A, T, H, F_\sigma) \quad (4.7)$$

In order to develop a parametric model to simulate concrete expansion as stated in Equation (4.7), its relationships have to be identified.

4.4.1 Relationship of ASR Strain to Reaction Extent

The graph in Figure 4.6 shows the expansion evolution for two different temperatures and the percentage of alkali reacted against time. Both graphs have similar curves with the values almost coincidental proving that temperature does not have a significant role in the curve development. Capra (1998) claimed that expansion

and reaction are disassociated with the argument that expansion does not occur as long as pores are available.

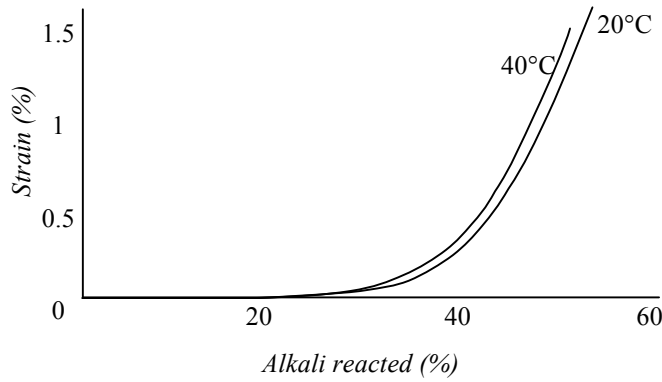


Figure 4.6: Evolution of strains and alkali for two temperature values (Diamond 1981)

Dron and Brivot (1981) proved from experimentation that silica dissolution could be interpreted as a chemical reaction that follows a first-order kinetic law which was defined by Dent-Glasser and Kataoka (1993) to be:

$$\xi|_{t=0} = 0 \qquad \xi|_{t \rightarrow \infty} = 1 \qquad (4.8)$$

Where the reaction extent, $\xi \in [0, 1]$ with 0 representing the start of reaction and 1 representing the end.

The reaction extent, ξ for constant condition can be interpreted as:

$$\xi = 1 - e^{-k^a t} \qquad (4.9)$$

Where t is the time and k^a , which is a coefficient that denotes the reaction velocity that depends on silica reactivity, pore liquid alkalinity, temperature and humidity.

The evolution of reaction extent, ξ in terms of time, t is stated as:

$$\dot{\xi} = k^a(T)[1 - \xi] \qquad (4.10)$$

Here, the reaction velocity, $k^a(T)$ varies according to the temperature. The higher the relative humidity and temperature are, the more the reaction is accelerated and a higher value of $k^a(T)$ is obtained.

Li (2000) represents the chemical reaction affinity, A to be:

$$A(\xi) = k_d \frac{d\xi}{dt} \quad (4.11)$$

Where $k_d > 0$ is a coefficient and $A(\xi)$ expresses the local imbalance driving the ASR gel formation. It decreases from an initial value $A(\xi=0) = A_0$ and reaches an equilibrium at $A(\xi=1) = 0$, at which the reaction stops. $A(\xi)$ defines the reaction order and follows the first-order kinetic law with respect to the reaction extent, ξ :

$$1 - \xi = \tau_c \frac{d\xi}{dt} \quad (4.12)$$

Where $\tau_c = k_d / A_0$ is the characteristic time constant of the reaction that is determined from experiment. The relationship between ASR strain, ε^a and reaction affinity, A is modeled by a bilinear law:

$$\begin{cases} \varepsilon^a = 0 & \text{for } A < A_0 \\ \varepsilon^a = \frac{\varepsilon_0}{A_0} (A - A_0) & \text{for } A > A_0 \end{cases} \quad (4.13)$$

The parameters ε_0 and A_0 are defined in Figure 4.7.

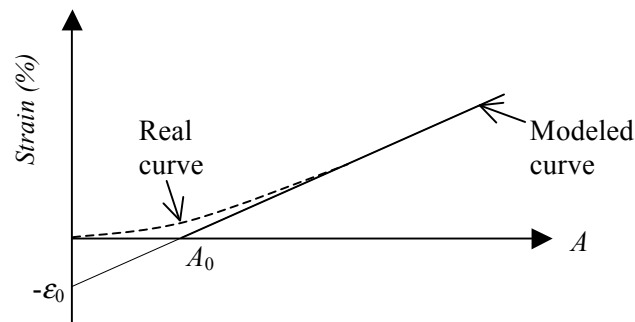


Figure 4.7: Determination of ε_0 and A_0 (Moranville-Regourd 1997)

4.4.2 Relationship of ASR Strain to Temperature

The parameter $k^a(T)$ from Equation (4.10) is a kinetic constant following the Arrhenius's law with T being the temperature, R is the ideal gas constant, the initial kinetic constant is denoted by k_0^a and U_a is the activation energy:

$$k^a(T) = k_0^a e^{\frac{-U_a}{RT}} \quad (4.14)$$

To include temperature effects, Equation (4.13) becomes:

$$\begin{cases} \varepsilon^a(t, T) = 0 & \text{for } A < A_0 \\ \varepsilon^a(t, T) = \frac{\varepsilon_0}{A_0} \left(1 - A_0 - e^{-k_0^a e^{\frac{U_a}{RT}} t} \right) & \text{for } A > A_0 \end{cases} \quad (4.15)$$

Larive (1998) conducted reactivity tests for over 600 specimens with various mixes for ambient and mechanical conditions and developed a thermodynamically-based model for the expansion evolution calibrated with experimental data. Her work is greatly acknowledged in the ASR field and has been used as a basis for numerous other works which include the determination of time parameters used to calculate the ASR reaction extent, ξ . Assuming an isothermal stress-free condition with constant temperature, the ASR reaction extent, ξ when plotted against time in Figure 4.8 defines two time parameters, the latency time, τ_L and the characteristic time, τ_C .

Ulm (2000) defined τ_L as the latency time that corresponds to the inflexion point, which is the time that is needed for the initial expansion of the gel in concrete pores in the presence of water. τ_C is the characteristic time that is defined by the intersection of the tangent at τ_L with the asymptotic unit value of the reaction extent, ξ . τ_C and τ_L are thermally dependent and can be expressed in terms of absolute temperature ($TK = 273 + T^\circ C$) and the corresponding activation energies that abide the Arrhenius concept:

$$\tau_L(T) = \tau_L(T_0) \exp \left[U_L \left(\frac{1}{T} - \frac{1}{T_0} \right) \right], \quad \tau_C(T) = \tau_C(T_0) \exp \left[U_C \left(\frac{1}{T} - \frac{1}{T_0} \right) \right] \quad (4.16)$$

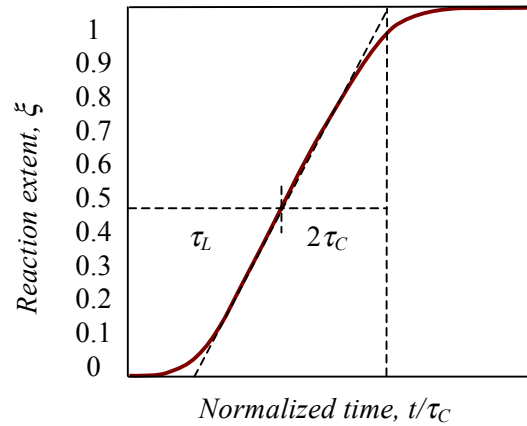


Figure 4.8: ASR reaction extent against time (Ulm 2000)

The variables U_L and U_C are the activation energies which represent the minimum energy required to trigger the reaction for the latency time, τ_L and the characteristic time, τ_C respectively and were determined from Larive tests to be $U_L = 9400 \pm 500K$ and $U_C = 5400 \pm 500K$. The latency and characteristic time constants, τ_C and τ_L tend to have different intensities for drying, sealed, humid and immersed in water conditions, for example given by Comi (2009) in Table 4.1:

Moisture conditions	τ_C (days)	τ_L (days)
Drying	47	200
Sealed	32	127
Humid	31	95
Immersed in water	27	58

Table 4.1: Initial latency and characteristic time constants at different moisture ambient conditions at 38°C (Comi 2009)

As can be seen, the time constant values are shorter when the moisture content is higher. For a large structure with a heterogeneous moisture distribution from one location to the other, this will result in a faster ASR reaction rate for high moisture regions, causing a heterogeneous deformation in the structure as opposed to where the time constants and relative humidity are assumed to be constant.

Larive (1998) represented a one-dimensional chemical expansion evolution, $\dot{\epsilon}^a$ for stress-free conditions as a function of latency and characteristic times, τ_L and τ_C , and asymptotic volumetric strain, ϵ_{∞} , which according to her findings has a value

ranging from $0.1 \pm 0.04\%$ to $0.4 \pm 0.15\%$ with the lower range for sealed conditions and the upper bound for immersed conditions.

$$\dot{\varepsilon}^a(t) = \frac{\varepsilon_\infty (e^{t/\tau_c} + e^{-(t+\tau_L)/\tau_c})}{\tau_c (1 + e^{-(t+\tau_L)/\tau_c})^2} \quad (4.17)$$

A coefficient λ is introduced from isothermal experiments for different temperatures and is represented by:

$$\lambda(\xi, T) = \left(\frac{k_d}{A_0} \right) = \tau_c(T_0) \frac{1 + \exp[-\tau_L(T_0)/\tau_c(T_0)]}{\xi + \exp[-\tau_L(T_0)/\tau_c(T_0)]} \quad (4.18)$$

And the reaction extent, ξ is determined from:

$$\xi(t) = \frac{\varepsilon}{\varepsilon_\infty} = \frac{1 - \exp(-t/\tau_c)}{1 + \exp(-t/\tau_c + \tau_L/\tau_c)} \quad (4.19)$$

Thus the kinetic law of reaction rate (Li 2000) is:

$$\dot{\xi} = \frac{1 - \xi}{\lambda(\xi, T)} \quad (4.20)$$

Equation (4.20) can be integrated step-by-step through approximation, for instance using the backward Euler difference scheme for any given temperature history, $T(t)$, making determination of the ASR reaction extent, ξ for varying temperature possible.

4.4.3 Relationship of ASR Strain to Applied Stress

Hobbs (1988) suggested an exponential function to describe the effect of applied stress, F_σ in alkali-silica reactivity:

$$F_\sigma = f(\sigma) = \exp\left(\frac{A_1 \sigma}{f_{c0}}\right) \quad (4.21)$$

Where f_{c0} is the initial compressive strength, A_1 is a material constant and σ is the average of the principle stresses.

In calculating the stress, Hobbs (1988) suggested that the effect of tension to be neglected and the applied stresses become (Mostagh 2008):

$$\begin{cases} F_{\sigma} = 1 & \text{if } \sigma \geq 0 \\ F_{\sigma} = f(\sigma) & \text{if } \sigma < 0 \end{cases} \quad (4.22)$$

4.4.4 Relationship of ASR Strain to Relative Humidity

Poole (1992) published a curve showing the evolution of expansion due to relative humidity, H . He concluded that ASR reactions are not initiated if H is lower than 50% and that significant expansion can only be seen if H is greater than 85%. He described the relation between expansion and relative humidity as a simple power function:

$$\frac{\varepsilon^a}{\varepsilon_{100}} = H^8 \quad (4.23)$$

Where ε_{100} is the free expansion at 100% H and 8 is the parameter of wedging.

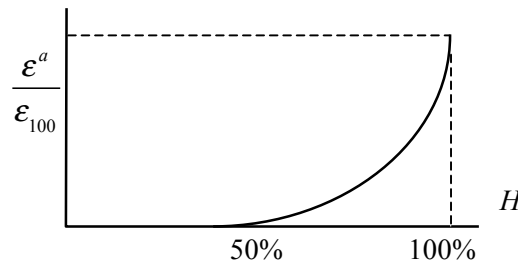


Figure 4.9: Graph of ε^a against relative humidity (Capra 1998)

In light of Equation (4.7) and the principal parameters outlined in the previous sections, the following equation is proposed by Capra to determine ASR strain, ε^a :

$$\varepsilon^a(A, T, H, \sigma) = H^8 \frac{\varepsilon_0}{A_0} \left(1 - A_0 - e^{-k_0^a e^{-\frac{U_{a_s}}{RT}}} \right) f(\sigma) \quad (4.24)$$

4.5 CONSERVATION EQUATIONS FOR ASR PROBLEMS

4.5.1 Conservation of Mass

Bangert (2004) suggested that in terms of alkali-silica reactivity, the volume fraction of solid, ϕ^s can be represented by the total of the volume fractions of the unreacted and reacted materials, ϕ^u and ϕ^r . The partial density then becomes:

$$\rho^s = \phi^s \varrho^s = \phi^u \varrho^u + \phi^r \varrho^r \quad (4.25)$$

At the start of the reaction, the material density of the reacted material, ϱ^r is taken as zero and the material density of solid represents the unreacted material, $\varrho^u = \varrho^s$. Once the reaction starts, ϱ^u changes into reacted material, where now $\varrho^r \neq 0$. He also stated that since the material density of the reacted material, ϱ^r is larger than that of the unreacted material, ϱ^u , making $\phi^s \varrho^s < \phi^u \varrho^u + \phi^r \varrho^r$, hence the material tends to swell. If both materials are assumed to be incompressible, the mass balance equations that have been explained in Chapter Three can be adapted for the ASR process into the following (Bangert 2004):

$$\frac{\partial \phi^u}{\partial t} + \text{div}(\phi^u \mathbf{V}^s) = \frac{\partial \phi^{u \rightarrow r}}{\partial t}, \quad \frac{\partial \phi^r}{\partial t} + \text{div}(\phi^r \mathbf{V}^s) = \frac{\partial \phi^{r \leftarrow u}}{\partial t} \quad (4.26)$$

Where \mathbf{V}^s is the velocity of solid.

Bangert further suggested that to ensure that the summation of the balances in Equation (4.26) is achieved, the following constraint must hold:

$$\varrho^u \frac{\partial \phi^{u \rightarrow r}}{\partial t} + \varrho^r \frac{\partial \phi^{r \leftarrow u}}{\partial t} = 0 \quad (4.27)$$

The terms $\varrho^u \frac{\partial \phi^{u \rightarrow r}}{\partial t}$ and $\varrho^r \frac{\partial \phi^{r \leftarrow u}}{\partial t}$ represent the mass exchange between the phases ϕ^u and ϕ^r due to the dissolution process.

If the velocity of the skeleton is assumed as $\mathbf{V}^s \approx 0$, and if the kinetics of the dissolution of silica as well as the mass exchange between ϕ^u and ϕ^r are assumed to follow the first-order kinetic law, hence:

$$\frac{\partial \phi^{u \rightarrow r}}{\partial t} = -k^a \phi^u, \quad \frac{\partial \phi^{r \leftarrow u}}{\partial t} = \frac{\rho^u}{\rho^r} k^a \phi^u \quad (4.28)$$

For constant environmental conditions, Equation (4.28) can be integrated analytically using ϕ_0^u as the initial value (Bangert 2004):

$$\phi^u = \phi_0^u [1 - \xi], \quad \phi^r = \frac{\rho^u}{\rho^r} \phi_0^u \xi \quad (4.29)$$

Where ξ is the ASR reaction extent determined from Equation (4.9).

According to Bangert, ASR expansion, ε^a and ASR expansion rate, $\dot{\varepsilon}^a$ can be determined from:

$$\varepsilon^a = \left[\frac{\rho^u}{\rho^r} - 1 \right] \xi \quad \frac{\partial \varepsilon^a}{\partial t} = k^a [1 - \xi] \left[\frac{\rho^u}{\rho^r} - 1 \right] \quad (4.30)$$

Where k^a is the coefficient for reaction velocity as explained in Section 4.4.1 and $\left[\frac{\rho^u}{\rho^r} - 1 \right]$ is the asymptotic ASR strain in a stress-free expansion test.

Both variables are assumed to be the chemical material parameters for ASR and can be obtained from experimental results as in the following:

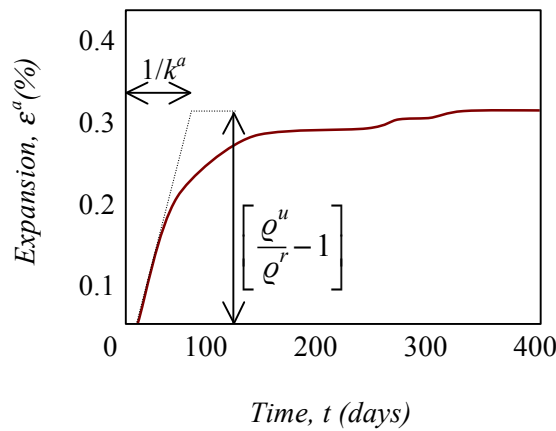


Figure 4.10: Chemical parameters obtained from an ASR expansion plot according to experimental results by Larive (1998) and Steffens et al. (2003), (Bangert 2004)

Or, they can also be obtained in relation to the water saturation value, s^l from the relationship below (Bangert 2004):

$$\frac{\varrho^u}{\varrho^r} - 1 = 1.27s^l - 0.754 \text{ [%]}, \quad \frac{1}{k^a} = -300s^l + 326 \text{ [days]} \quad (4.31)$$

4.5.2 Conservation of Linear Momentum

The partial momentum balance for the quasistatic case with the body forces neglected are given by:

$$\text{div } \boldsymbol{\sigma}^\pi + \mathbf{F}^\pi = 0 \quad (4.32)$$

Where π denotes the phase in the material, $\boldsymbol{\sigma}^\pi$ is the partial stress tensor and \mathbf{F}^π is the momentum production which can be interpreted as the local interaction force per unit volume between the constituent φ^π and the other constituents. The overall stress tensor of porous material, $\boldsymbol{\sigma}$ is given by the sum of the partial stress tensors, $\boldsymbol{\sigma}^\pi$, where $\boldsymbol{\sigma} = \boldsymbol{\sigma}^s + \boldsymbol{\sigma}^f + \boldsymbol{\sigma}^g$ with s, f and g representing the solid, fluid and gaseous phases respectively. The overall conservation of momentum is stated by $\text{div } \boldsymbol{\sigma} = 0$ with $\mathbf{F}^s + \mathbf{F}^f + \mathbf{F}^g = 0$ as the constraint. According to the theory of porous medium, the stress state of the skeleton can be separated into two parts; the first part governed by the skeleton deformation and the stress induced by pore fluid and gas diffusion and the second part governed by pore pressure:

$$\boldsymbol{\sigma} = \boldsymbol{\sigma}^s - \phi^s P \mathbf{1} \quad (4.33)$$

Where $P = s^f P^f + s^g P^g$ with s^π denoting the saturation.

The pore pressure, P^f is determined from Equation (3.33) and gas pressure, P^g is related to the material density, ϱ^g by the following constitutive law for an ideal gas:

$$\varrho^g = \frac{M^g}{RT} P^g \quad (4.34)$$

Where R is the ideal gas constant, T is the absolute temperature and M is the molar mass.

4.6 CONSTITUTIVE EQUATIONS FOR ASR ANALYSIS

Assume that the swelling pressure imposed by the ASR gel is represented by P^a . Under stress-free conditions, P^a is self-balanced by the tension, σ^s in the skeleton. This can be seen in Figure 4.11.

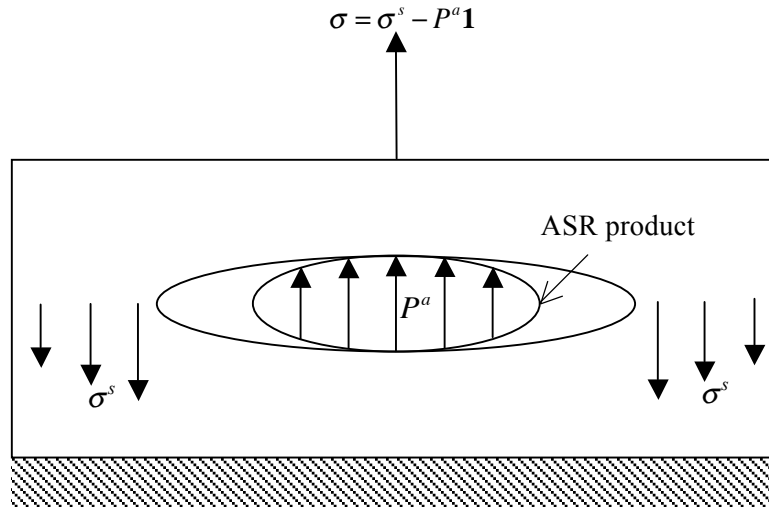


Figure 4.11: Mesoscopic mechanism of ASR swelling (Li 2000)

Ignoring the effects of pore fluid and gas, Equation (4.33) can be adapted to find the difference between the skeleton stress and gel pressure:

$$\sigma = \sigma^s - P^a \mathbf{1} \quad (4.35)$$

For mesoscopic modeling, the volume fraction term ϕ can be omitted. As stated in Section 4.5.1, the reacted material has a larger density than the unreacted material, causing the pressure from the gel, P^a to build up at the location sites. Since P^a is larger than σ^s , the overall material swells. If C_a is defined as the compliance of the ASR gel, the following constitutive equation is written (Fairbairn 2004):

$$P^a = C_a \langle -(\varepsilon - \varepsilon^a) \rangle \quad (4.36)$$

Where $\langle x \rangle = \frac{1}{2}(x + |x|)$.

Assuming that the pore deforms with the same strain as the whole domain, hence the skeleton strain is determined from:

$$\varepsilon = \frac{u}{l_0} \quad (4.37)$$

Where ε is the strain at the pore, u is the deformation, and l_0 is the initial length of the pore.

Fairbairn (2004) gives the three-dimensional pore pressure, P^a as:

$$P^a = B^a \begin{bmatrix} 3\varepsilon^a - \varepsilon^v & 0 & 0 \\ 0 & 3\varepsilon^a - \varepsilon^v & 0 \\ 0 & 0 & 3\varepsilon^a - \varepsilon^v \end{bmatrix} \quad (4.38)$$

Where $B^a = \frac{E^a}{3(1-2\nu^a)}$ is the bulk modulus of the gel multiplied by porosity, ϕ^v .

The gel's Poisson's ratio, ν^a can be taken as 0, and E^a is the Young's Modulus of the gel which is taken from 60 to 120 N/mm² (Wen 2000). The volumetric strain, ε^{vol} is expressed by:

$$\varepsilon^{vol} = \varepsilon_x + \varepsilon_y + \varepsilon_z \quad (4.39)$$

Where $i = x, y, z$ represents the global coordinate system.

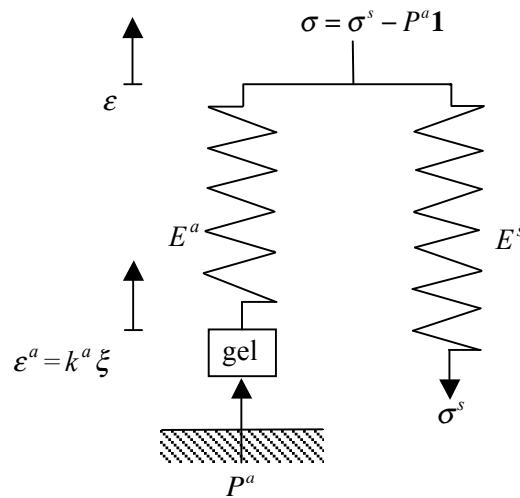


Figure 4.12: Chemoelastic pressure-spring device of ASR swelling (Ulm 2000)

The macroscopic representation of the solid skeleton response to ASR swelling can be translated into a one-dimensional rheological model as shown in Figure 4.12 by Ulm (2000). This model represents the chemoelastic model of ASR expansion. The analogue for ASR gel and concrete behavior is in form of a parallel chemical pressure cell-spring device, where one spring models the gel while the other spring models the concrete solid skeleton. The material is assumed to be linear elastic. The spring C^s represents the stiffness of the solid skeleton with σ^s being the macroscopic stress due to external forces, and ε is the corresponding overall strain:

$$\sigma^s = C^s \varepsilon \quad (4.40)$$

Equation (4.40) for stress and strain relationship obeys the Hooke's law for elastic behavior.

Assume that F^D is the thermodynamic force of the chemical reaction:

$$F^D = \sum_{\alpha=R_{i=1,m}} \nu^\alpha M^\alpha A_m^\alpha - \nu^a M^a A_m^a \quad (4.41)$$

Where M^a and M^α are the molar masses of reactants and product, $R_{i=1,m}$ represents the reactants with $\nu_{i=1,m}$ as their stoichiometric coefficients and A_m^a and A_m^α for their chemical potential (Ulm 2000). The system free energy, ψ reads:

$$\psi(\varepsilon, \xi) = \frac{1}{2} C^s (\varepsilon - \varepsilon_\infty \xi)^2 + \frac{1}{2} C^a \varepsilon^2 + \frac{1}{2} F_0^D (1 - \xi)^2 \quad (4.42)$$

The third term in Equation (4.42) represents the chemical energy stocked in the chemical pot as can be seen in Figure 4.12.

Neglecting free expansion, $\sigma \neq 0$ where the material cannot freely expand, the stress equilibrium of the chemoelastic device is (Ulm 2000):

$$\left\{ \begin{array}{l} \sigma = \frac{\partial \psi}{\partial \varepsilon} = C(\varepsilon - \varepsilon_\infty \xi) \\ F^D = -\frac{\partial \psi}{\partial \xi} = \left(\frac{\varepsilon_\infty C^a}{C^a + C^s} \right) \sigma + F_0^D (1 - \xi) \doteq F_0^D (1 - \xi) \end{array} \right. \quad (4.43)$$

Where σ is the total stress acting on a unit volume of concrete and ASR gel. Rearranging Equation (4.43)¹ for stress-free conditions, $\sigma=0$ will result in:

$$\varepsilon^a(t) = \varepsilon_\infty \xi(t) \quad (4.44)$$

Where ε^a is linear to the reaction extent, ξ . Equation (4.44) shows that ASR strain evolution is only governed by the noninstantaneous kinetics of the chemical reaction. In a stress-free condition, the only unknown is the reaction extent, ξ .

The mechanical behavior due to ASR strain under stress-free condition may consist of an elastic stain, ε^e , a mechanical inelastic strain which is independent of ASR, ε^{pl} , and an ASR strain, ε^a , giving the value of total strain, ε as:

$$\varepsilon = \varepsilon^e + \varepsilon^{pl} + \varepsilon^a \quad (4.45)$$

The term ε^a is represented by a six dimension vector referring to a global reference system (x_1, x_2, x_3) and defined as $\varepsilon^a = \varepsilon^{a,Vol} / 3 \{1 \ 1 \ 1 \ 0 \ 0 \ 0\}^T$.

For numerical investigation of the ASR process, it can be implemented in the form of the initial strain into the system. Rewriting the term in Equation (4.43)¹, the equation for stress due to ASR strain is determined from:

$$\sigma = \mathbf{C}(\varepsilon - \varepsilon^a) \quad (4.46)$$

Where σ is the stress tensor, ε is the total strain tensor, ε^a is the initial ASR strain tensor obtained from Equation (4.44) and \mathbf{C} is the elastic matrix of the mechanical properties.

Similar to the case for the thermal strain, ASR strains can be added into the consistent global nodal force vector \mathbf{F}^a :

$$\mathbf{F}^a = \int_{\Omega} \mathbf{B}^T \mathbf{C} \varepsilon^a d\Omega \quad (4.47)$$

Where \mathbf{B} is the strain-displacement matrix.

This nodal force vector is added to the mechanical nodal force vector when solving the static equilibrium equation $\mathbf{Ku} = \mathbf{F}$ similar to Equation (3.59) for thermal stress with:

$$\mathbf{Ku} = \mathbf{F} = \mathbf{F}^{mech} + \mathbf{F}^a \quad (4.48)$$

According to Ulm (2000), due to the assumed independence of the kinetic law on stresses and strains, the implementation of ASR for modeling the local value of reaction extent only requires a stable time integration scheme. Therefore, applying the backward Euler formulation to Equation (4.20) for stress-free condition yields:

$$\xi_{n+1} = \xi_n + \frac{\Delta t (1 - \xi_n)}{\tau_c (T_{n+1}) \lambda(\xi_n, T_{n+1})} \quad (4.49)$$

With ξ_{n+1} and ξ_n being the ASR reaction extent at time t_n and $t_{n+1} = t + \Delta t$. The term $\lambda(\xi_n, T_{n+1})$ is defined by Equation (4.18).

The post-computation of the chemoelastic strain starts with the iteration of Equation (4.49), resulting in ASR reaction extent values, ξ that may vary with temperature history, T . If only the thermal effect is taken into account, then the strain values, ε^a are determined from Equation (4.17). Inclusion of the effects of relative humidity, H and others are calculated using Equation (4.24). If temperatures are kept constant, ASR strain can be modeled to include the effect of relative humidity, H and the chemical reaction extent, ξ .

Assuming isotropic chemoelastic behavior for ASR swelling, the strain energy of an element can be written as:

$$U_e = \frac{1}{2} t \int_{\Omega} (\varepsilon - \varepsilon_0^a - \varepsilon_0^{th})^T \sigma d\Omega = \frac{1}{2} t \int_{\Omega} (\varepsilon - \varepsilon_0^a - \varepsilon_0^{th})^T \mathbf{C} (\varepsilon - \varepsilon_0^a - \varepsilon_0^{th}) d\Omega \quad (4.50)$$

With thermal strain, $\varepsilon_0^{th} = \alpha_T (T - T_0)$ and ASR strain, $\varepsilon_0^a = \varepsilon_{\infty} \xi$.

If the strain-displacement matrix is $\boldsymbol{\varepsilon} = \mathbf{B}\mathbf{u}$ and the stiffness matrix $\mathbf{K} = t \int_{\Omega} \mathbf{B}^T \mathbf{C} \mathbf{B} d\Omega$, Equation (4.50) becomes:

$$\begin{aligned} U_e = & \frac{1}{2} \mathbf{u}^T \mathbf{K} \mathbf{u} - t \mathbf{u}^T \int_{\Omega} \mathbf{B}^T \mathbf{C} \boldsymbol{\varepsilon}_0^a d\Omega - t \mathbf{u}^T \int_{\Omega} \mathbf{B}^T \mathbf{C} \boldsymbol{\varepsilon}_0^{th} d\Omega \\ & + \frac{1}{2} t \int_{\Omega} \boldsymbol{\varepsilon}_0^{a,T} \mathbf{C} \boldsymbol{\varepsilon}_0^a d\Omega + \frac{1}{2} t \int_{\Omega} \boldsymbol{\varepsilon}_0^{th,T} \mathbf{C} \boldsymbol{\varepsilon}_0^{th} d\Omega + t \mathbf{u}^T \int_{\Omega} \boldsymbol{\varepsilon}_0^{a,T} \mathbf{C} \boldsymbol{\varepsilon}_0^{th} d\Omega \end{aligned} \quad (4.51)$$

The element potential energy can be written as:

$$\Pi = U_e - W = \frac{1}{2} \underbrace{\mathbf{u}^T \mathbf{K} \mathbf{u} - \bar{\mathbf{F}}^{a,T} \mathbf{u} - \bar{\mathbf{F}}^{th,T} \mathbf{u}}_{U_e} - \underbrace{\mathbf{F}^T \mathbf{u}}_W \quad (4.52)$$

With $\bar{\mathbf{F}}^a = t \int_{\Omega} \mathbf{B}^T \mathbf{C} \boldsymbol{\varepsilon}_0^a d\Omega$ and $\bar{\mathbf{F}}^{th} = t \int_{\Omega} \mathbf{B}^T \mathbf{C} \boldsymbol{\varepsilon}_0^{th} d\Omega$.

Minimizing the potential energy results, initial ASR and thermal strains are implemented:

$$\mathbf{K} \mathbf{u} = \mathbf{F}^{mech} + \mathbf{F}^a + \mathbf{F}^{th} \quad (4.53)$$

Where \mathbf{F}^{mech} is determined from Equation (3.42).

Hence, the total combined effect for thermal and ASR can be determined from the equation for stress:

$$\boldsymbol{\sigma} = \mathbf{C} (\boldsymbol{\varepsilon} - \boldsymbol{\varepsilon}^a - \boldsymbol{\varepsilon}^{th}) \quad (4.54)$$

The velocity distribution asserts additional pressure to the cementitious matrix, which affects the deformation of the structure. In order to calculate the thermal strain distribution with an additional hydrostatic pressure effect, the pore pressure distribution can be incorporated into the stress equation in (4.54) as an additional stress vector:

$$\boldsymbol{\sigma} = \mathbf{C} (\boldsymbol{\varepsilon} - \boldsymbol{\varepsilon}^a - \boldsymbol{\varepsilon}^{th}) - P^f \mathbf{1} \quad (4.55)$$

4.7 HEAT AND MOISTURE DIFFUSION LENGTHS

Determination of characteristic and latency time constants are set by first determining the lengths of heat and water diffusion into a structure. Ulm (2000) defined the one-dimensional Fick's law of diffusion taken for longest length and neglecting latent heat related to the exothermic or endothermic nature of ASR to be:

$$\frac{\partial(T - T_0)}{\partial t} = D_0 \frac{\partial^2(T - T_0)}{\partial x^2} \quad (4.56)$$

Where $D_0 = k/C_v$ denotes the thermal diffusivity with k being the thermal conductivity coefficient and C_v is the specific heat capacity.

When $t=0$, the temperature throughout the structure is the initial temperature, T_0 . Since the boundary condition of the structure is fixed, when time, $t>0$, the boundary temperature is kept constant but the temperature throughout the structure changes to T_s , where $T_s > T_0$. If x is the semi-infinite half-space with $x \geq 0$, then:

$$\begin{aligned} \text{For } x \ll \sqrt{D_0 t}, T &= T_s \\ \text{For } x > \sqrt{D_0 t}, T &= T_0 \end{aligned} \quad (4.57)$$

Where $\sqrt{D_0 t}$ is the heat diffusion length in the structure.

The relationship between the time and latency time constants can be explained with the conditions below (Ulm 2000):

$$\begin{aligned} \text{For } 0 < t < \tau_L(T_s), \xi(t) &= 0 \text{ everywhere} \\ \text{For } \tau_L(T_s) \ll t < \tau_L(T_0), \\ \text{For } x < \sqrt{D_0 \tau_L(T_s)}, \xi(t) &= 1 \\ \text{For } x > \sqrt{D_0 t}, \xi(t) &= 0 \\ \text{For } t > \tau_L(T_0), \xi(t) &= 1 \text{ everywhere} \end{aligned} \quad (4.58)$$

The first term in Equation (4.58) means that the ASR process only begins when t reaches the value of $\tau_L(T_s)$. Once the reaction begins and t is between $\tau_L(T_s)$ and $\tau_L(T_0)$, where $\tau_L(T_s)$ is much faster than $\tau_L(T_0)$ since $T_s > T_0$, therefore the points which are located inside the range of the heat diffusion length, x , have all reacted to ASR and the

reaction extent, ξ is 1 at these points and is 0 at points further from the heat diffusion length. This reaction continues until t is larger than $\tau_L(T_0)$, in which case, all the reaction has finished and ξ is 1 at all points in the model. From Equation (4.58) and according to Ulm, the characteristic length, l_l can be defined as the zone where both effects of thermal diffusion and ASR occur, where ASR is thermally activated and is determined by:

$$l_l = \sqrt{D_0 \tau_L(T_s)} \quad (4.59)$$

The same rule applies for water diffusion. Steffens (2003) outlined that if H_0 is the initial relative humidity at $t=0$, therefore:

$$\frac{\partial(H - H_0)}{\partial t} = D \frac{\partial^2(H - H_0)}{\partial x^2} \quad (4.60)$$

Where D is the diffusion coefficient, which is a nonlinear function of internal humidity, H .

According to Carslaw and Jaeger (1960):

$$\begin{aligned} \text{For } x \ll \sqrt{Dt}, H &= H_s \\ \text{For } x > \sqrt{Dt}, H &= H_0 \end{aligned} \quad (4.61)$$

Where \sqrt{Dt} is the water diffusion length in the structure and H_s is larger than H_0 since water diffusion causes the relative humidity to increase.

The relationship between the time, characteristic and latency time constants can be explained with the conditions below:

$$\begin{aligned} \text{For } 0 < t \leq \tau_L(H_s) + \tau_C(H_s), \xi(t) &= 0 \text{ everywhere} \\ \text{For } t > \tau_L(H_s) + \tau_C(H_s), \\ \text{For } x < \sqrt{D[\tau_L(H_s) + \tau_C(H_s)]}, \xi(t) &= 1 \\ \text{For } x > \sqrt{D[\tau_L(H_s) + \tau_C(H_s)]}, \xi(t) &= 0 \\ \text{For } t > \tau_L(H_0) + \tau_C(H_0), \xi(t) &= 1 \text{ everywhere} \end{aligned} \quad (4.62)$$

The first term in Equation (4.62) means that the ASR process only begins when t reaches the value of $\tau_L(H_s) + \tau_C(H_s)$, where $\tau_L(H_s)$ is much faster than $\tau_L(H_0)$ since $H_s > H_0$. Once the reaction begins and t is larger than $\tau_L(H_s) + \tau_C(H_s)$, the points which are located inside the range of the water diffusion length, x , will have all reacted to ASR and the reaction extent, ξ is 1 at these points and 0 at points further from the water diffusion length. This reaction continues until t is larger than $\tau_L(H_0) + \tau_C(H_0)$, in which case all the reactions have finished and ξ is 1 at all points in the model. From Equation (4.62) and according to Steffens, the characteristic length, l_H can be defined as the zone where the swelling can be affected by the humidity gradient and is determined by:

$$l_H = \sqrt{D[\tau_L(H_0) + \tau_C(H_0)]} \quad (4.63)$$

Therefore, from Equation (4.63), the spatial changes of the latency and characteristic time constants due to heat and water diffusion can be determined.

The time step value is determined from the equation below:

$$\Delta t = \epsilon \tau_C(T_{n+1}) \quad (4.64)$$

With $\epsilon \ll 1$, typically 0.01. Larive (1998) outlined in her work that the relationship between time, t and latency time constant, τ_L is as the following. In the event that $0 < t < \tau_L(T_0)$, the ASR reaction extent, ξ is assumed to be 0 everywhere in the cross-section since the reaction has not started. However, if $\tau_L(T_s) \ll t < \tau_L(T_0)$, where T_s is the temperature in the any given cross-section, the ASR reaction extent, ξ would range from between 0 to 1 depending on the temperature, T_s at a particular point in the cross-section. If $t \gg \tau_L(T_0)$, the ASR reaction extent, ξ is equal to 1 everywhere, meaning that the reaction is complete in all locations.

5 DAMAGE MECHANICS

5.1 INTRODUCTION

Two fields that study the mechanics of concrete deformation are the fracture mechanics and damage mechanics. Fracture mechanics enables the prediction of the propagation of pre-existing cracks. Damage mechanics on the other hand, is used to investigate the situation of a given structure before any cracks appear. The continuum damage mechanics can be used to investigate the mechanical behavior of a structure. In addition to that, prediction of physical and chemical behavior of a structure can also be investigated. This makes it a suitable solution to study structural behavior under the influence of alkali-aggregate reactivity. The theory of continuum damage mechanics is first proposed by Kachanov (1958) to determine creep deformation in metals. Then its usage was extended, where in the late 1970s, damage mechanics has begun to be used for strain softening investigations. Damage mechanics was later developed for elasticity-based damage, for instance by Lemaitre and Mazars (1982). Since then, the continuum damage mechanics have been used to investigate numerous deformation problems, be it for ductile materials like metal or brittle material like concrete. In this chapter, the fundamental equations for the isotropic damage model will be stated, starting off with the local damage formulation and extending it into the nonlocal damage formulation. The equations include a coupling between the isotropic damage model with an additional strain value obtained from ASR expansion and hydrostatic pressure as a result from fluid flow and heat transfer simulation.

5.2 DAMAGE FORMULATION

Past researches conducted on ASR using damage or fracture mechanics include that of Adeghe (1993), who developed a three-dimensional finite element model to simulate the effects of ASR expansion using inverse analysis for the determination of its parameters, where he considers solely the influence of the stresses on the evolution of ASR. Bazant and Stefans (2000) developed a model based on fracture mechanics using a coupled approach to describe the kinetics of the reaction. Both Huang and Pietrusczak, and Capra (1998) developed damage models that introduce probabilistic and fracture mechanic concepts that allow the representation of anisotropic behavior of ASR swelling. Bangert, Kuhl and Meschke (2004) modeled ASR deterioration at a macroscopic level under the influence of chemo-hygro-mechanical loading. They categorized the cementitious matrix into unreacted and reacted phases of alkali-silica reactivity. Since the ASR reacted phase has a larger density than the unreacted phase, the material swells. They also concluded that ASR expansion is influenced by chemical material parameters that are influenced by water saturation in a linear relationship. From their findings, it was discovered that ASR was influenced by both the activation of moisture diffusion and reaction kinetics.

Damage of the concrete structure is nonuniform, which means that different points throughout the spatial distribution of the structure have different mechanical resistance towards loading which will result in heterogeneity of the deformation. This causes the elastic properties of the material to spatially differ, resulting in the material anisotropy. It was based on this theory that Cordebois and Sidoroff (1982) defined damage to be a variable of the fourth-order tensor that corresponds to the elastic coefficient tensor containing 21 independent components. Since damage is a permanent and nonrecoverable deformation, when represented by a variable, the variable would be an increasing value. The damage variable, represented with the symbol ω may be considered as an internal state variable that characterizes the irreversible deterioration of a material point in accordance with the thermodynamic formulation in order to describe the deformation process. An assumption made by Krajcinovic (1984) in damage modeling is that response of the material depends only on the current state of the microstructural arrangement. Another assumption made in this research is that since

ASR and thermal strains affect the structure through asymptotic expansion, it is assumed that damage is mostly influenced by tensile strains.

The damage variable is taken as a scalar value when the material is assumed to have isotropic damage deformation in all directions, for example for concrete. However, some materials like wood have anisotropic stiffness degradation according to the grain of the material. Therefore in this case, damage variable, ω is presented as a vector. Kachanov (1986) clarified that damage could take place either under elastic deformation, elastic-plastic deformation or creep damage. However, for brittle materials like concrete the plastic strains could be neglected (Aliabadi 2001). Hence only the evolution law for elasticity needs to be added to the constitutive law. Lemaitre and Chaboche (1990) and Lemaitre (1996) made an assumption that the material should be considered as linear elastic, neglecting all other behaviors like viscous and nonmechanical effects. This results in an elasticity-based damage model which is applicable for usage in materials without plastic strains, like brittle material such as concrete.

Assume that for the isotropic damage model, thermal and nonmechanical effects like chemical expansion are omitted. The strain is also assumed to be small. The material is assumed to be perfectly brittle solid under static loading and isothermal conditions. Cracks and voids are assumed to be equally distributed in all directions. Kachanov (1986) and Skrzypek (1999) defined the damage variable, ω in terms of A as:

$$\omega = \frac{A}{A_0} \quad \text{where } \omega \in [0,1] \quad (5.1)$$

Or can be written as:

$$\vartheta = 1 - \omega = \frac{A_0 - A}{A_0} \quad (5.2)$$

Where A_0 is the initial area of the intersection of a plane within the volume element of an undamaged material and A is the effective area of intersections lost to damage in the element.

The damage variable, ω ranges from $\omega(\vartheta=1)=0$ for undamaged material and $\omega(\vartheta=0)=1$ for completely damaged material. This means that as the damage variable, ω increases, the material deforms, resulting in the lowering of the material stiffness until microcracks occur. Coupling between isotropic damage and elasticity can be introduced using the concept of effective stresses and strain equivalence (Kachanov 1986). Assuming that $\bar{\sigma}$ is the effective stress related to the undamaged area and $\sigma = F/A$ is the Cauchy stress and from uniaxial tension test we obtain:

$$\bar{\sigma} = \frac{F}{A_0 - A} = \frac{F}{A_0(1-\omega)} = \frac{F}{A_0\vartheta} = \frac{\sigma}{\vartheta} \quad (5.3)$$

Therefore $\vartheta = \frac{\sigma}{\bar{\sigma}}$ and F is the force acting on the material.

Lemaitre (1985) assumed that damage growth rate is determined primarily from the level of effective stress, which in turn modifies the strain response. The stress and strain behavior of the damaged material can be represented from the Hooke's law by replacing the Cauchy stress, σ with effective stress, $\bar{\sigma}$ (Kachanov 1986). Hence:

$$\varepsilon = \frac{\bar{\sigma}}{E} = \frac{1}{E} \frac{\sigma}{\vartheta} \quad (5.4)$$

Where ε is the strain tensor. Rearranging Equation (5.4), we get:

$$\bar{\sigma} = \left\{ \frac{1}{1-\omega} \right\} \sigma \quad (5.5)$$

5.2.1 Strain-based Local Damage Formulation

The Helmholtz free energy per unit mass, ψ under isothermal condition is:

$$\psi(\varepsilon, \omega) = \frac{1}{2}(1-\omega)\varepsilon : C_0 : \varepsilon \quad (5.6)$$

Where C_0 is the undamaged stiffness tensor. If damage variable, $\omega = 0$, no damage has occurred in the system and therefore, Equation (5.6) is reduced to the equation for the strain energy of undamaged material (Comi, Aliabadi 2001).

The derivative of Equation (5.6) against ε produces the classical stress-strain relation $\bar{\sigma} = C_0 \varepsilon$ from Hooke's Law multiplied with $\vartheta = 1 - \omega$:

$$\sigma = \frac{\partial \psi}{\partial \varepsilon} = (1 - \omega) C_0 : \varepsilon \quad (5.7)$$

From Equation (5.7), it can be seen that $(1 - \omega)$ acts as a stiffness reduction factor. When the value for damage variable increases, $(1 - \omega) C_0$ decreases until it becomes zero when $\omega = 1$. When $\omega = 1$, that material point is cracked, meaning that particular point becomes stress-free and therefore stress can no longer be transferred.

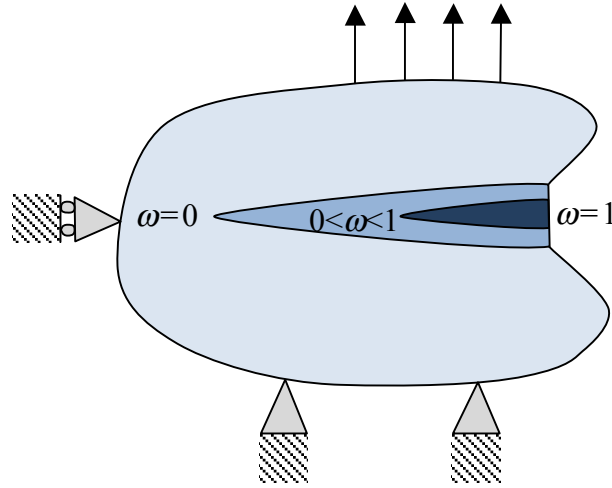


Figure 5.1: Damage variable (Peerlings 1999)

Damage evolution is usually related to the energy release rate, \dot{U} that is associated to the damage variable, for which elasticity-based damage is given by Lemaitre and Chaboche (1990) as:

$$\dot{U}(\varepsilon) = -\frac{\partial \psi}{\partial \omega} = \frac{1}{2} \varepsilon : C_0 : \varepsilon \quad (5.8)$$

The energy release rate in Equation (5.8) depends only on the strain components and can be regarded as an equivalent strain measure that uses the elastic modulus to weigh the different strain components. For isothermal and pure mechanical process, the entropy of the system is determined from:

$$\dot{\eta} = \sigma_{ij} \dot{\varepsilon}_{ij} - \dot{\psi} \geq 0 \quad (5.9)$$

Equation (5.9) is also known as the Clausius-Duham Inequality. Inserting the time derivative of Equation (5.7) into (5.8) we get:

$$\sigma_{ij}\dot{\varepsilon}_{ij} - \frac{\partial\psi}{\partial\varepsilon_{ij}}\dot{\varepsilon}_{ij} - \frac{\partial\psi}{\partial\omega}\dot{\omega} \geq 0 \quad (5.10)$$

It must fulfill $\sigma_{ij} - \frac{\partial\psi}{\partial\varepsilon_{ij}} = 0$ and $-\dot{U}\dot{\omega} \geq 0$ so that the inequality for $\dot{\varepsilon}_{ij}$ values hold.

The damage rate vector that can be expressed by the following flow rule:

$$\dot{\omega} = -\frac{\partial f}{\partial \dot{U}} \dot{\kappa} \quad (5.11)$$

5.2.2 Stress-based Local Damage Formulation

The stress-based free energy per unit mass, ψ under isothermal condition is:

$$\psi(\sigma_{ij}, \omega) = \frac{1}{2(1-\omega)} C_{ijkl} \sigma_{ij} \sigma_{kl} \quad (5.12)$$

Where σ_{ij} is the stress tensor, ω is the damage variable and C_{ijkl} is the elastic stiffness tensor. If damage variable, $\omega = 0$, no damage has occurred in the system and therefore Equation (5.6) is reduced to the equation for the stress energy of undamaged material.

The Clausius-Duham Inequality function for isothermal case is stated as:

$$\psi = \dot{\sigma}_{ij} \varepsilon_{ij} \geq 0 \quad (5.13)$$

It must fulfill $\varepsilon_{ij} - \frac{\partial\psi}{\partial\sigma_{ij}} = 0$ and $-\dot{U}\dot{\omega} \geq 0$ so that the inequality for $\dot{\sigma}_{ij}$ values hold.

The energy release rate, \dot{U} is given as:

$$\dot{U}(\sigma_{ij}) = \frac{\partial\psi}{\partial\omega} = \frac{1}{(1-\omega)^2} C_{ijkl} \sigma_{ij} \sigma_{kl} \quad (5.14)$$

The equivalent strain has a direct effect on the failure surface, which represents the boundary of the elastic domain (Eckardt 2009).

Mazars (1986) determined the equivalent strain, $\tilde{\varepsilon}$:

$$\tilde{\varepsilon}(\varepsilon) = \frac{1}{E} \max_{i=1,2,3} \langle C : \varepsilon \rangle_i \quad \text{or} \quad \tilde{\varepsilon}(\varepsilon) = \frac{1}{E} \sqrt{\sum_{i=1}^3 \langle C : \varepsilon \rangle_i^2} \quad (5.15)$$

Where ε_i is the principal strains and $\langle x \rangle = \frac{1}{2}(x + |x|)$ is the McAuley brackets which represents the positive Eigen values of the effective stress tensor.

Concrete can be defined as a quasi-brittle material, which means that although plasticity can be negligible, it needs more energy for cracking to initiate. Figure 5.2 shows a typical loading and unloading curve for strain and stress response for a concrete tensile testing when the load is removed at regular intervals. Upon loading, the slope increases linearly until it reaches the proportional limit. At this stage, no plastic deformation exists and the material will return to its original state after the load is released. Beyond the proportional limit to the yield point, both elastic and plastic deformation starts to accumulate. After the yield point, the material goes through a term called strain hardening.

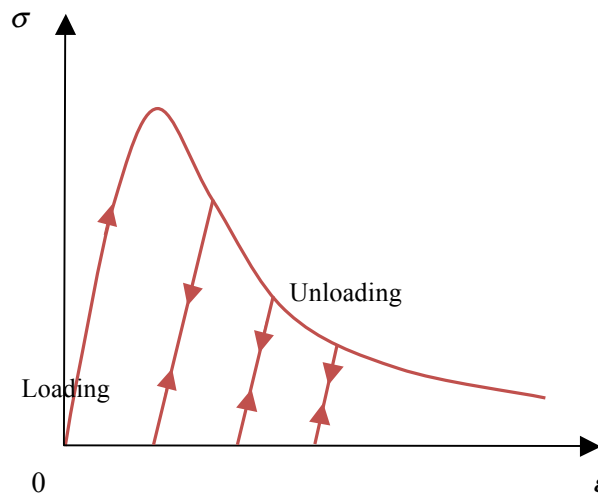


Figure 5.2: Typical stress-strain response for loading/unloading tensile test for concrete

At this stage, the slope begins to decrease steadily and monotonically with the load and eventually becomes negative. This is when the ultimate yield strength is reached, after which beyond this point, softening begins. At this stage, if load is removed at different stress levels, unloading does not return to the original strain value

but leaves a residual strain. The slope starts to decrease with the increase of deformation until it reaches a zero value at the fracture energy point, G_f after which only strain increases while stress decreases. At this stage, application of reloading causes the values to restart at the last point where unloading starts and the slope is lesser, meaning that the elastic stiffness is reduced, which agrees with Equation (5.6) where $(1 - \omega)$ acts as a stiffness reduction factor.

Equation (5.2) shows how damage variable affects the stress and strain relationship. However, damage growth may increase under the influence of stresses and strains. Whether this growth is due to happen or not possibly depends on this function based on strain components (Peerlings 1999, Florez-Lopez, Aliabadi 2001):

$$f(\varepsilon, \kappa) = \tilde{\varepsilon}(\varepsilon) - \kappa(\omega) \quad (5.16)$$

Where $\tilde{\varepsilon}$ is the positive equivalent strain and κ is a threshold value which is the largest value of the equivalent strain ever reached by the material at the considered point to characterize the previous loading history, and $f = 0$ describes a loading surface in a strain space. The shape of the loading surface is determined by the equivalent strain, $\tilde{\varepsilon}$ and the size of the loading surface is determined by the threshold variable, κ . When the strain states are within the loading surface, where $f < 0$, the material portrays elastic behavior, which means that no damage growth has occurred. When the strain states reach the threshold value of $\tilde{\varepsilon} = \kappa$, where $f \geq 0$, the damage variable increases.

From the stress-strain graph in Figure 5.2, it shows that in the softening stage where damage is increasing, for the strain state to remain in the $f = 0$ loading surface zone, the elastic domain in the strain space must increase to allocate for the increasing strain. Therefore in order to maintain this condition, the value of damage threshold, κ is always equal to the largest value of equivalent strain, $\tilde{\varepsilon}$ which was locally attained during the loading history. These definitions can also be described by the Karush-Kuhn-Tucker conditions:

$$f \leq 0, \quad \dot{\kappa} \geq 0, \quad f\dot{\kappa} = 0 \quad (5.17)$$

For the initial value of the damage threshold, $\kappa = \kappa_0$. By complying with the Karush-Kuhn-Tucker conditions, the current state equivalent strain is ensured to never be larger than κ . Increment of κ can only be obtained from $\kappa = \varepsilon_{eq}$.

Once the conditions above are satisfied, damage evolution can be determined from this following law:

$$\dot{\omega} = \begin{cases} g(\omega, \varepsilon_{eq}) \dot{\varepsilon}_{eq} & \text{if } f = 0 \text{ and } \dot{f} = 0 \\ 0 & \text{if } f = 0 \text{ and } \dot{f} < 0 \text{ or } f < 0 \end{cases} \quad (5.18)$$

The evolution of the scalar damage variable, ω can also be described as a function of equivalent strain, $\tilde{\varepsilon}$ by means of three softening functions as stated below:

Exponential softening function:

$$\omega(\kappa) = \begin{cases} 0.0 & \kappa < \varepsilon_0 \\ 1.0 - \frac{\varepsilon_0}{\kappa} \exp\left(\frac{\varepsilon_0 - \kappa}{\varepsilon_f - \varepsilon_0}\right) & \kappa \geq \varepsilon_0 \end{cases} \quad (5.19)$$

Linear softening function:

$$\omega(\kappa) = \begin{cases} 0.0 & \kappa < \varepsilon_0 \\ 1.0 + \frac{f}{E} \cdot \frac{\kappa - 2G}{\kappa(\varepsilon_f - \varepsilon_0)} & \varepsilon_0 \leq \kappa \leq \varepsilon_f \\ 1.0 & \kappa > \varepsilon_f \end{cases} \quad (5.20)$$

Hordjick softening function:

$$\varepsilon_c = 2.57(\varepsilon_f - \varepsilon_0) \quad (5.21)$$

$$\omega(\kappa) = \begin{cases} 0.0 & \kappa < \varepsilon_0 \\ 1.0 - \left[1.0 + \left(c_1 \frac{\kappa}{\varepsilon_c} \right)^3 \right] \cdot \dots \cdot \exp\left(-c_2 \frac{\kappa}{\varepsilon_c} \right)^{\frac{\varepsilon_0}{\kappa}} + \dots & \varepsilon_0 \leq \kappa \leq \varepsilon_c \\ \dots + (1.0 + c_1^3) \exp\left(-c_2 \right)^{\frac{\varepsilon_0}{\varepsilon_c}} & \\ 1.0 & \kappa > \varepsilon_c \end{cases}$$

Where κ is the maximum equivalent strain value since the start of the loading where $\omega=0$ until the current time where ω is being calculated.

The term ε_0 is the elastic limit defined by $\varepsilon_0 = f_{ct} / E$ and ε_f is a parameter that controls the material's ductility, defined by $\varepsilon_f = 2G_f / f_{ct}$, with f_{ct} being the tensile or compressive strength and G_f being the specific fracture energy dissipated per crack surface. The specific fracture energy is equivalent to the area under the plot in Figure 5.3:

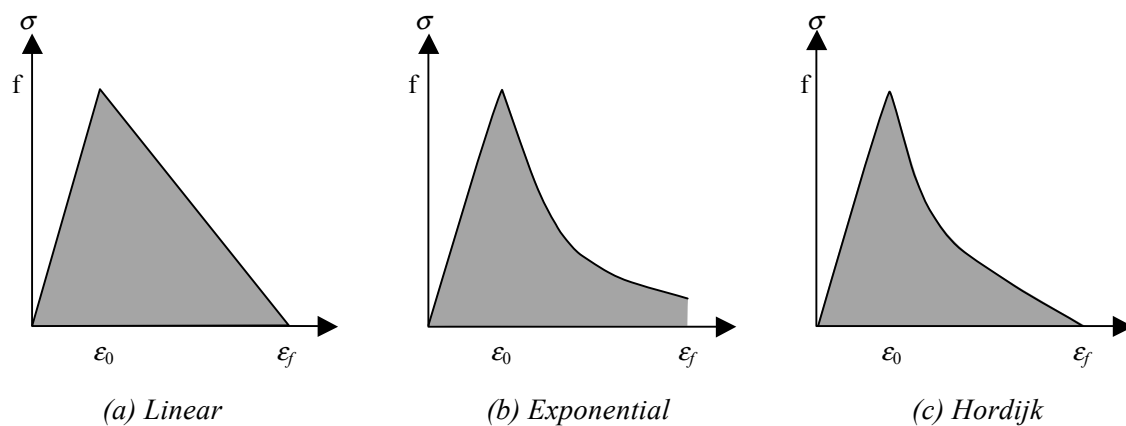


Figure 5.3: Softening functions

Since damage depends only on the strain history of the particular volume element under consideration, it is called the local damage formulation.

5.2.3 Nonlocal Damage Formulation

A few researchers that are well established in the field of nonlocal damage formulation are Bazant, Mazars and Kachanov. Bazant (1987) in his research presented extensively on the theory on nonlocal damage and its usage. The theory behind the need to perform nonlocal damage analysis is that the drawback of local damage formulation in Section 5.2.2 is that it leads to numerical problems because it shows mesh dependency of the response in a finite element analysis. Strain softening at the continuum level due to damage accumulation causes damage to accumulate within narrow bands or called as localized zones. In structures, these localized zones will be the microstructural regions. In numerical simulation schemes, these localized zones are

what cause mesh dependency. Using a refined mesh will reduce the localization zone to zero. In order to overcome these problems, the nonlocal damage formulation is developed by modifying the constitutive law through regularization of the damage model. With this, the local action can be neglected.

Rodríguez-Ferran (2003) stated that for nonlocal damage, the damage parameter that describes the loss of stiffness depends on the strain state in a neighbourhood associated to a characteristic length of the point under consideration. Comi (2003) stated that the long-range nature of the microscopic interaction forces is taken into account on the macroscale by expressing the material constitutive law in terms of one or more nonlocal variables defined as suitable weighted averages of their local values over the interaction domain.

Peerlings (1999) stated that spatial interactions resulting from nonlocality prevents damage growth from localizing in a surface. Instead, damage growth occupies a finite band, the width of which is related to the internal length scale provided by nonlocality. Hence damage can now be assumed to depend on the state of a particular volume element as well as on the state in a limited zone enclosing the specific point under consideration. Damage evolution law in terms of nonlocal equivalent strain, $\tilde{\varepsilon}(\bar{\varepsilon})$ is stated as:

$$f(\bar{\varepsilon}, \kappa) = \tilde{\varepsilon}(\bar{\varepsilon}) - \kappa(\omega) \quad (5.22)$$

Damage evolution can be determined from this following law:

$$\dot{\omega} = \begin{cases} g(\omega, \tilde{\varepsilon}(\bar{\varepsilon})) \dot{\tilde{\varepsilon}}(\bar{\varepsilon}) & \text{if } f = 0 \text{ and } \dot{f} = 0 \\ 0 & \text{if } f = 0 \text{ and } \dot{f} < 0 \text{ or } f < 0 \end{cases} \quad (5.23)$$

In the nonlocal formulation of the material law, the strain tensor, ε is replaced by the averaged strain tensor, $\bar{\varepsilon}$ for the calculation of equivalent strain:

$$\tilde{\varepsilon}(\bar{\varepsilon}) = \frac{1}{E} \max_{i=1,2,3} \langle C : \bar{\varepsilon} \rangle_i \quad (5.24)$$

Or:

$$\tilde{\varepsilon}(\bar{\varepsilon}) = \frac{1}{E} \sqrt{\sum_{i=1}^3 \langle C : \bar{\varepsilon} \rangle_i^2} \quad (5.25)$$

Only the damage evolution law is modified with respect to the local modeling. What makes local and nonlocal calculation different is the calculation of the average equivalent strain.

The anisotropy of material properties due to damage evolution results in the progressive degradation of the elastic modulus and uniaxial compressive/tensile strength. Skrypek (1999) derived a function for stiffness degradation from uniaxial effective stress, $\bar{\sigma}$ based on strain equivalence principle (Lemaitre 1971). Say that the Cauchy stress is represented by $\sigma = \bar{E}\varepsilon$ and the effective stress by $\bar{\sigma} = E\bar{\varepsilon}$ and assuming that $\varepsilon = \bar{\varepsilon}$, therefore from Equation (5.5):

$$E\varepsilon = \frac{\bar{E}\varepsilon}{1-\omega} \quad (5.26)$$

Which can be rearranged into $\bar{E} = E(1-\omega)$. The evolution of the uniaxial compressive/tensile strength can be written as:

$$\bar{f}_{ct} = f_{ct}(1-\omega) \quad (5.27)$$

Where E is the Young's modulus of elasticity of the undamaged material with $\omega = \alpha_c\omega_c + \alpha_t\omega_t$ with c representing compression and t representing tension (Moranville-Regourd 1997). Now, the degradation of the elastic modulus and compressive/tensile strength can be determined from the damage variable, ω .

5.3 CONSTITUTIVE EQUATION FOR DAMAGE IN ASR ANALYSIS

Assume that the damage at a given temperature value, T and relative humidity, H remains elastic and has isotropic behavior. Determination of the local ASR reaction extent, ξ at each time step, dt is performed with a stable time integration method as outlined in Section 4.6, taking into account the corresponding moisture and temperature profiles for each time step of the numerical procedure. The stress and damage states from the mechanical response are obtained from the rheological modeling coupled with the damage law and adding the effect of thermal strain, ε^{th} , ASR strain, ε^a , pore

pressure, P^f acting as a hydrostatic loading and self-weight of the dam, Equations (4.55) and (5.26) can be modified into:

$$\boldsymbol{\sigma} = (1 - \omega) \left[\mathbf{C} (\boldsymbol{\varepsilon} - \boldsymbol{\varepsilon}^a - \boldsymbol{\varepsilon}^{th}) - P^f \mathbf{1} \right] \quad (5.28)$$

Where \mathbf{C} is the fourth order linear elastic material tensor and ω denotes the scalar damage parameter. $\boldsymbol{\varepsilon}$ is the overall strain tensor, which in determining the overall stress tensor, must have the values of additional effects of thermal strains, $\boldsymbol{\varepsilon}^{th}$, ASR strains, $\boldsymbol{\varepsilon}^a$, and pore pressure, P^f subtracted from it.

5.4 FINITE ELEMENT IMPLEMENTATION OF THE DAMAGE ANALYSIS

The nonlocal strain is calculated from (Peerlings 1999):

$$\bar{\boldsymbol{\varepsilon}}(\mathbf{x}) = \int_{\Omega} w(\mathbf{y}, \mathbf{x}) \boldsymbol{\varepsilon}(\mathbf{y}) d\Omega \quad (5.29)$$

Where $w(\mathbf{y}, \mathbf{x})$ is a weight function which usually decays rapidly with the distance $|\mathbf{y} - \mathbf{x}|$.

The constitutive law linking different state variables of the model is defined from Equation (5.7):

$$\sigma_{ij} = (1 - \omega(\tilde{\boldsymbol{\varepsilon}}(\bar{\boldsymbol{\varepsilon}}))) C_{ijkl}^{el} \varepsilon_{kl} \quad (5.30)$$

The finite element implementation of nonlocal damage model differs from the local damage formulation, wherein the nonlocal damage formulation has an additional linear partial differential equation:

$$\tilde{\boldsymbol{\varepsilon}}(\bar{\boldsymbol{\varepsilon}}) - c \Delta \tilde{\boldsymbol{\varepsilon}}(\bar{\boldsymbol{\varepsilon}}) = \boldsymbol{\varepsilon} \quad (5.31)$$

Where c is the square of the dimension length, which is the internal length scale of the model and thus determines the degree to which damage growth localizes. Equation (5.31) needs to be additionally discretized on top of the displacement components, solved simultaneously with the standard equilibrium equations (Peerlings 1999).

The weak form of Equation (5.31) for the discretization of equivalent strain is:

$$\mathbf{e} \left[\int_{\Omega} (c\mathbf{B}^T \mathbf{B} + \mathbf{N}^T \mathbf{N}) d\Omega \right] = \left\{ \int_{\Omega} \mathbf{N}^T \boldsymbol{\varepsilon} d\Omega \right\} \quad (5.32)$$

As compared to discretization of standard strain that is given by:

$$\left[\int_{\Omega} \mathbf{B}^T \mathbf{C}_0 \mathbf{B} \mathbf{u} d\Omega \right] = \left\{ \int_{\Gamma} \mathbf{N}^T \mathbf{t} d\Gamma \right\} \quad (5.33)$$

Where \mathbf{N} represents the interpolation function, \mathbf{t} is the boundary traction, \mathbf{B} represents the derivatives of the interpolation function, \mathbf{u} is the vector of nodal displacements and \mathbf{e} represents the vector of nodal values of $\tilde{\boldsymbol{\varepsilon}}(\bar{\boldsymbol{\varepsilon}})$. Equations (5.32) and (5.33) can then be solved by the Newton-Raphson or other types of iterations.

6 MODELING ASR AT THE MACROSCALE

6.1 INTRODUCTION

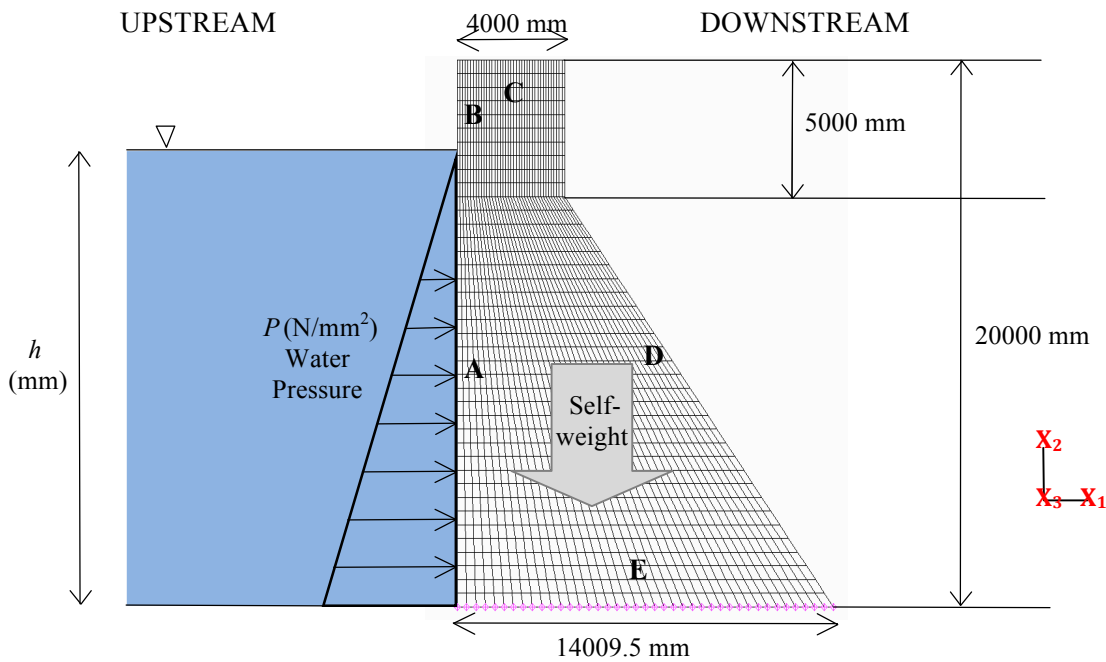
Many simulations on the study of ASR expansivity have been conducted on the macroscale level, for instance by Saouma and Perotti (2006), and Mostagh and Ghaemian (2008). As opposed to the material level where concrete can be considered as a heterogeneous material, concrete at a coarser scale is modeled as homogeneous, consisting of one phase which is concrete. The choice between homogeneous or heterogeneous media depends on the type of results that is required, whether the investigation is done on the material or structural level. When modeling at a structural level where any material point of view is irrelevant, a homogeneous model is sufficient. An advantage of the macroscale compared to a mesoscale model is that the numbers of degrees of freedom are greatly reduced and therefore a larger structure can be modeled. Having a smaller number of degrees of freedom cuts back simulation time greatly, plus, the results obtained are also sufficient. In this chapter, an engineering example of a thermo-chemo-hygro-mechanical model of a concrete gravity dam at the macroscale will be studied for varying environmental conditions of temperature and relative humidity.

6.2 MACROSCALE SIMULATION OF A CONCRETE GRAVITY DAM

Various experimental evidences for ASR deterioration can be found from literature, for example by Saouma and Perotti (2005), and Comi (2009). Comi developed a chemo-thermo-damage model of a gravity dam that evaluates the local evolution of ASR swelling governed only by temperature, resulting in a damage model that is fully decoupled from the heat-diffusion problem. Saouma and Perotti worked on temperature and hydrostatic loading on a dam and its effects on the ASR process. Mostagh and Ghaemain (2008) did an analysis of the Beauharnois power plant gravity dam on how ASR reaction has a high dependency on stress, resulting in the vertical strains being smaller than the horizontal strains. Fairbairn (2004) simulated the stress anisotropy of ASR swelling due to thermal and moisture dependency. The numerical example presented here illustrates the performance of a two-dimensional concrete gravity dam tested for thermo-hygro-chemo-mechanical loading using the finite element method described in the previous chapters. The simulation was developed using the stochastic finite element software SLANG. The Newton-Raphson iterative method was adapted for this model.

6.2.1 Modeling Parameters

Figure 6.1 shows the two-dimensional cross-section of a concrete gravity dam measuring 14009.5 mm width at the bottom surface and 4000 mm width at the top surface. The total height of the dam is 20000 mm. The finite element mesh for the cross-section consists of 1681 nodes with 1600 elements. The elements used in the dam are four-noded plane elements with four integrations points. The structure is restraint at the bottom surface in both x_1 and x_2 directions, while all other surfaces are allowed to move. The number of degrees of freedom for heat and pressure elements is 1681 with one degree of freedom per node and the number of degrees of freedom for mechanically loaded elements are 3362 with two degrees of freedom per node to accommodate for the x_1 and x_2 directions, using plane strain in the simulation.



Region	Boundary Conditions
A	Heat: $T = T_1^\circ\text{C}$ Pressure: $P = \rho gh$ $= 1000 \text{ kg/m}^3 \times 9.81 \text{ m/s}^2 \times h \text{ m}$
B	Heat: $T = T_1^\circ\text{C}$ Pressure: $P = 0.0 \text{ N/mm}^2$
C	Heat: $T = T_1^\circ\text{C}$ Pressure: $P = 0.0 \text{ N/mm}^2$
D	Heat: $T = T_1^\circ\text{C}$ Pressure: $P = 0.0 \text{ N/mm}^2$
E	Heat: $T = T_2^\circ\text{C}$ Pressure: $P = 0.0 \text{ N/mm}^2$

Figure 6.1: Two-dimensional macroscale model of the undeformed concrete gravity dam and the acting boundary conditions

Boundary conditions as can be seen in Figure 6.1 show that the upstream surface of the dam is exposed to water. This huge amount of body represents the mechanical loading for the system with the water pressure determined from $P(x) = \rho gh$ from the surface at $h = 17500 \text{ mm}$ height from the base of the dam exposed to hydrostatic loading. As a matter of simplification, all external boundaries will be taken as $T_1^\circ\text{C}$ and the base of the dam will be subjected to $T_2^\circ\text{C}$ which will be defined later. All the initial conditions for fluid and pressure are set to 0.0 N/mm^2 . Fluid flow in the dam will only be facilitated by fluid pressure from the upstream and gravitational force.

Material properties	Values
Tensile strength, f_t (N/mm ²)	3.0
Compressive strength, f_c (N/mm ²)	40.0
Fracture energy, G (Nmm/mm ²)	0.012
Nonlocal radius, R (mm)	176
Density of concrete, ρ (kg/m ³)	2240
Porosity of concrete, ϕ (%)	15
Permeability of concrete, κ_C (m ²)	1×10^{-7}
Asymptotic ASR expansion, ε_∞ (%)	0.22
Poisson's ratio, ν	0.12
Relative humidity, H (%)	80
Initial latency time constant, $\tau_l(T_0)$ (days)	550
Initial characteristic time constant, $\tau_c(T_0)$ (days)	80
Initial temperature of concrete, T_0 (K)	290.15
Young's modulus of concrete, E (N/mm ²)	40000
Thermal conductivity of concrete, k (W/mK)	1.77
Specific heat capacity of concrete, C_v (J/gK)	880
Density of fluid, ρ_f (kg/m ³)	1000
Viscosity of fluid, μ_f at 20°C (Pa.s)	8.9×10^{-4}
Linear coefficient of thermal expansion, α_T at 20°C (/°C)	12×10^{-6}
Volumetric coefficient of thermal expansion, β_T at 20°C (/°C)	207×10^{-6}

Table 6.1: Material properties of the concrete gravity dam

6.2.2 Theories and Assumptions

The numerical example presented here illustrates the performance of a two-dimensional decoupled thermo-chemo-hygro-mechanical model of a concrete gravity dam that evaluates the evolution of ASR resulting in a damage model for alkali-silica reactivity. The numerical simulation of stress anisotropy due to the ASR phenomena is performed by taking into consideration the thermoactivation of alkali-silica reactivity and its dependency on relative humidity. The simulation was developed using finite element method described in the previous chapters. Considering the fact that damage caused by ASR is due to expansion, behaviour of the concrete gravity dam under compressive stress can be modeled as linear. Since the ultimate compressive strength value, f_c is not exceeded, damage due to compression is assumed negligible. Creep and shrinkage will not be considered in this simulation.

The material properties that are used for the simulation of the concrete gravity dam in Table 6.1 are selected as optimal values for alkali-silica reactivity conditions. The material properties are assumed to be homogeneous throughout the macroscale domain. In modeling the effect of ASR in this research for a concrete gravity dam, the asymptotic ASR expansion, ε_∞ is assumed to be 0.22. Relative humidity is added into the simulation through Equation (4.24). The latency and characteristics time values, τ_L and τ_C are influenced by temperature and relative humidity. The initial values are assumed for humid environmental conditions, which will change during the simulation according to Equation (4.16). The new time constants values will be used in Equation (4.19) in order to determine the ASR reaction extent, ξ . The ASR reaction extent, ξ values will then be used in Equation (4.44) to determine the resulting ASR strains, ε^a .

The velocity of fluid, V_i in the model is simulated according to the Navier-Stokes equation for natural convection with the influence of gravity force, g represented by the Boussinesq term. The Navier-Stokes equation is represented in Equation (3.50). As can be seen from the equation, fluid flow is influenced by temperature, T and pressure, P . Temperature distribution, which is solved using Equation (3.53) is also dependent on velocity. The body of water at the upstream region of the dam, as can be seen in Figure 6.1 represents hydrostatic loading onto the dam and can be tested for its effects on the ASR process. Calculation of the pressure distribution is done using the penalty method in Equation (3.33).

The simulation of fluid flow and heat transfer using the finite element method is developed using the backward Euler method. This method linearizes transient and nonlinear equations in Equations (3.56) and (3.57) into the linear form in Equation (3.59). The Newton-Raphson iterative method was adapted for this model. More on this theory is explained in Section 2.5.2. The error tolerance is taken as 0.010 according to Reddy (2004).

6.2.3 Heat Analysis for Transient Conditions

This section displays the results of temperature distribution due to transient thermal condition. For the boundary conditions of $T_1=20^\circ\text{C}$ and $T_2=17^\circ\text{C}$ (refer to Figure 6.1 for the boundary conditions) and the initial condition of T_2 , solution of Equation (3.59) results in the temperature distributions shown in Figure 6.2.

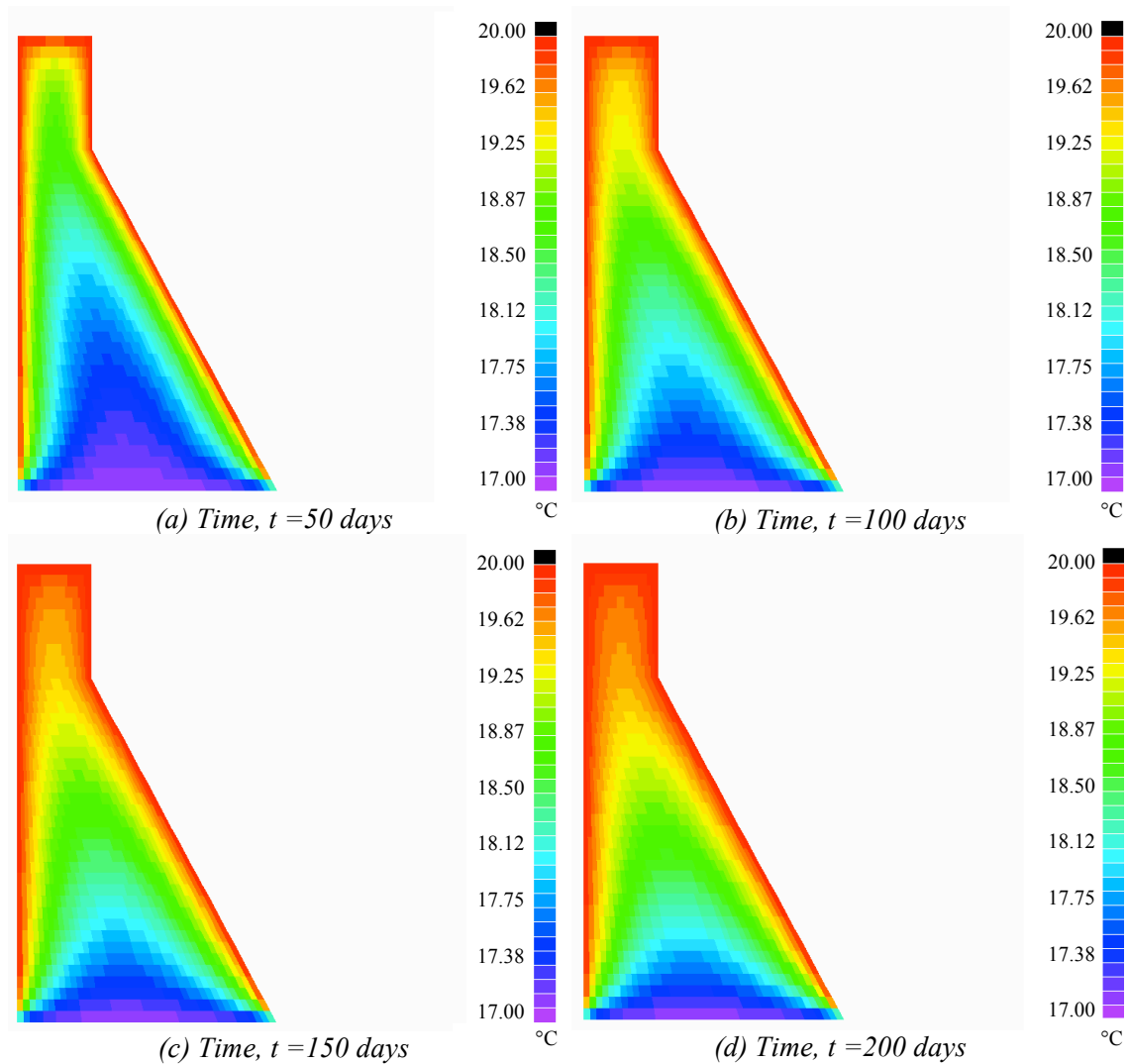


Figure 6.2: Temperature distribution throughout the concrete gravity dam for temperatures ranging from 17°C for the initial condition and base to 20°C for all other boundary conditions

Temperature distribution behaves linearly, moving from higher temperature boundaries into the internal region which has lower temperature until a steady state solution is reached in approximately 200 days. The length of time needed to reach equilibrium depends mainly on the material properties of the concrete; which are the thermal conductivity coefficient, k and the specific heat coefficient, C_v and if there are any other influencing conditions affecting the concrete.

6.2.4 Thermal Stress Analysis for Transient Conditions

Assume that the dam consists of hardened concrete subjected to a small thermal difference and that the thermo-mechanical behaviour of the material in this model behaves in a linear manner. The intensity of thermal expansion and contraction in the gravity dam depends on the concrete stiffness. A higher material stiffness results in lower expansion or contraction. Figure 6.3 shows that a positive thermal difference between the surface and the inner region of the dam causes it to expand horizontally. In the vertical direction, contraction of the dam shows that the effect of dead load due to the self-weight of the dam is larger than the effect of thermal expansion.

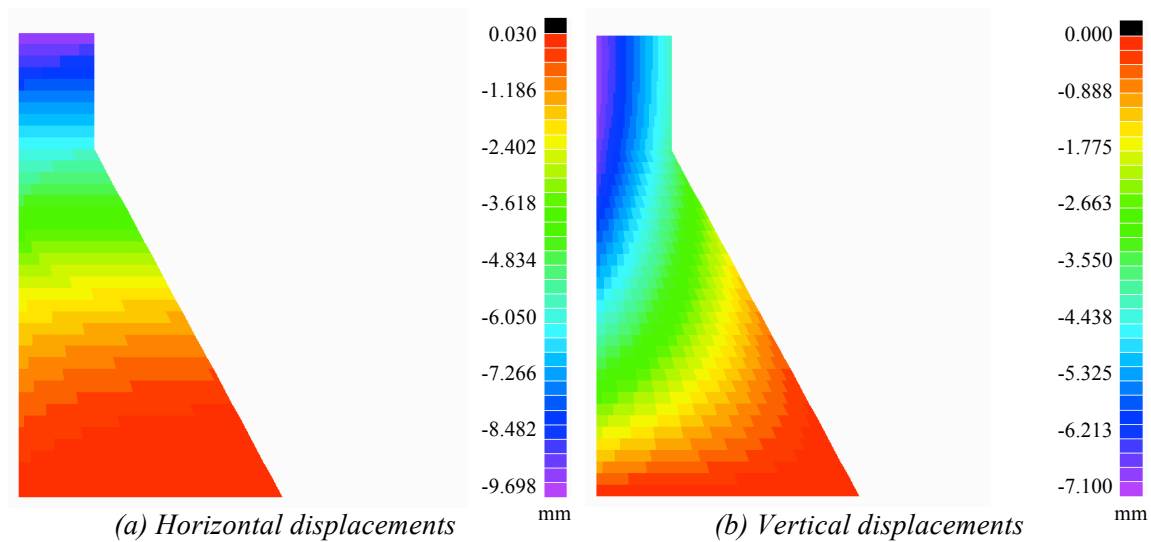
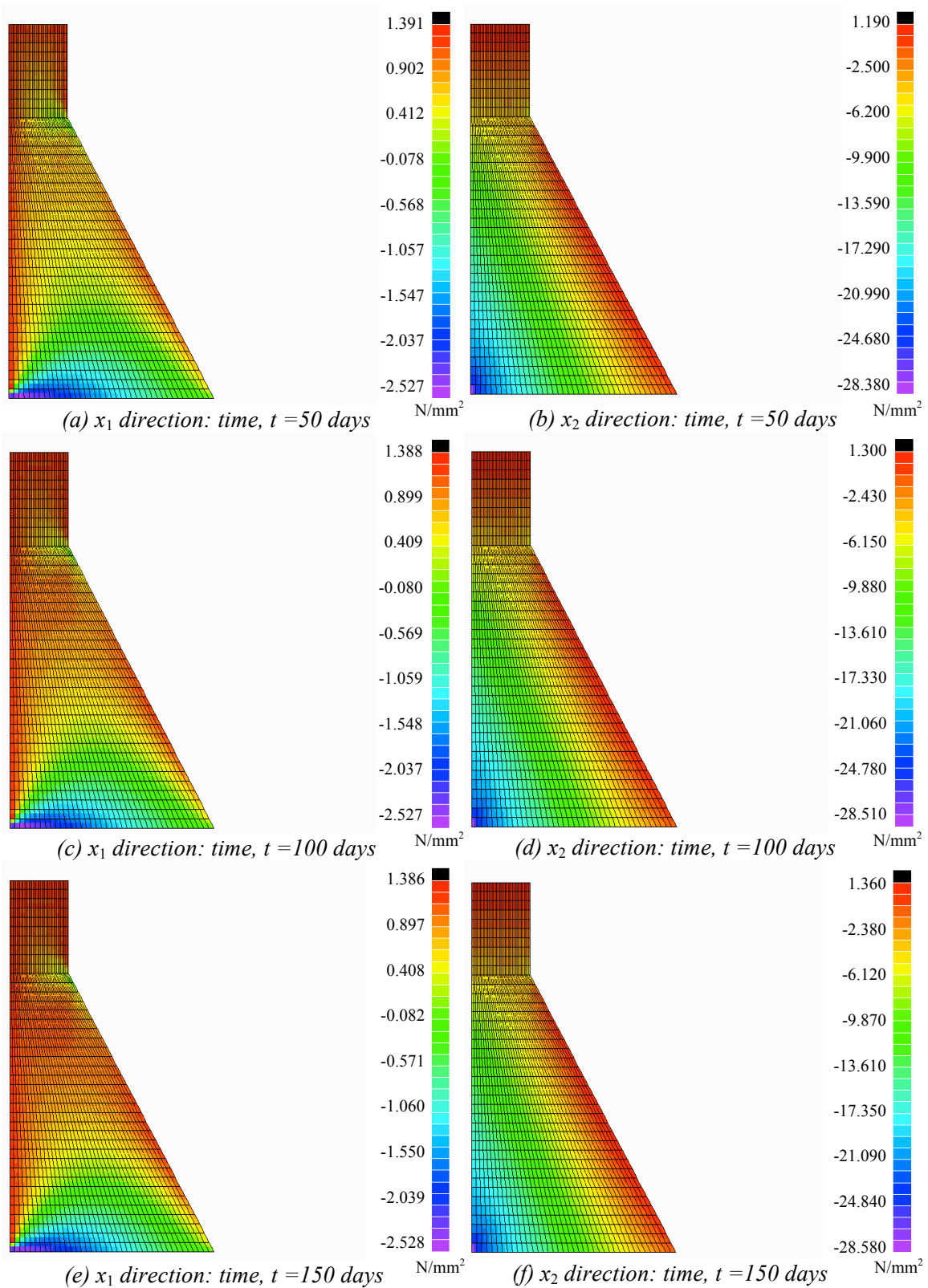


Figure 6.3: Displacement contours due to thermal expansion at 200 days in the dam for temperatures ranging from 17°C for the initial condition and base to 20°C for all other boundary conditions

These effects are also reflected in the thermal stress distributions in Figure 6.4. By solving Equation (3.41) for thermal stresses in the dam, the stress distributions portray tensile stresses throughout the structure due to thermal expansion. Distributions show that the maximum tensile stress values for the horizontal and vertical stresses are similar and that the stress values increase with the movement of thermal distribution into the concrete. This causes the outer regions of the dam to reach constant stress values first while the inner region stress values continue to change, with the values of stress in the outer regions having higher stress distribution in both horizontal and vertical directions due to the higher thermal difference at those regions. The vertical stress distribution portrays higher compressive stresses compared to the horizontal direction due to the

dead load effect, with the maximum compressive stress in the bottom left corner of the dam due to the restraints and the shape of dam expansion.



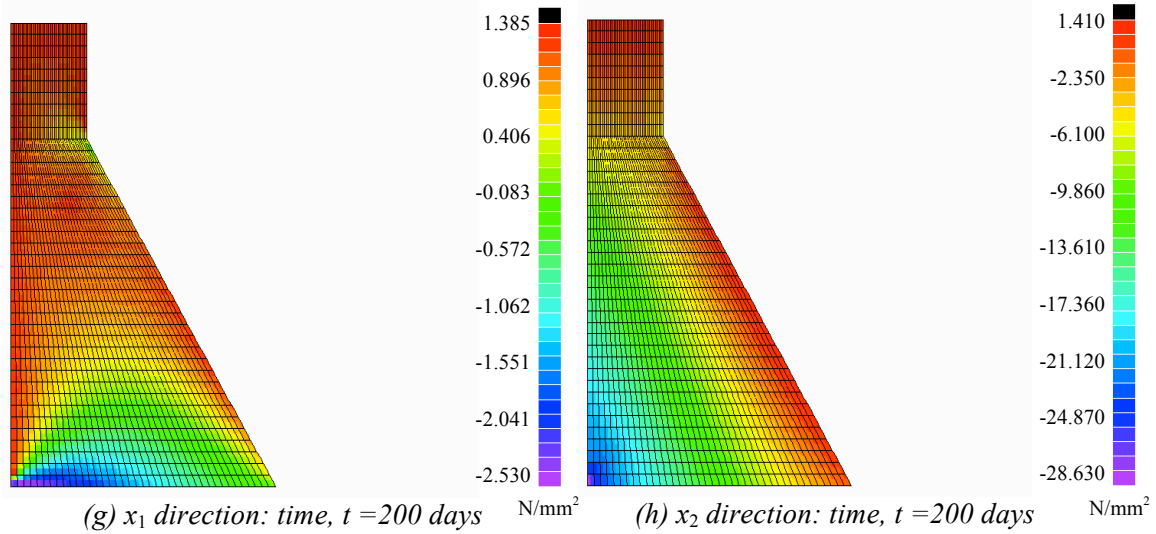


Figure 6.4: Thermal stress distributions due to temperature gradient from 17°C for the initial condition and base to 20°C for all other boundary conditions

The effects of temperature on the concrete gravity dam can be seen from three models for different temperature distributions ranging from 10°C , 15°C and 17°C for the initial condition and the base temperature, T_1 and 20°C for outer boundary conditions, T_2 (refer to Figure 6.1 for the boundary conditions). The resulting averaged thermal stress values for Element 650 for the three temperature models are shown in Figure 6.5. It can be seen that a higher difference in temperature results in a higher thermal stress, but still follows the same pattern as for a lower temperature difference.

The stress value increases rapidly in the initial stage, after which it becomes constant. This is reflected in the formulation from Equation (3.38), where strain due to thermal effects is proportionate to the temperature difference at a point between iterations. This shows that how large the temperature difference ($T_2 - T_1$) is, or if the result of ($T_2 - T_1$) is negative or positive, is a major factor in determining the intensity of thermal expansion or contraction.

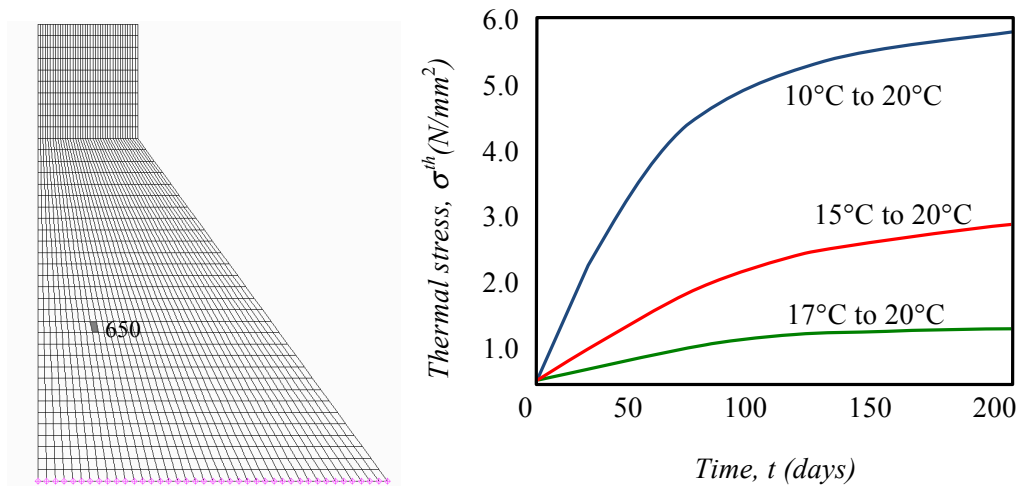


Figure 6.5: Thermal stress, σ^{th} for three models of temperature distributions of between 10°C, 15°C and 17°C for the initial condition and base to 20°C for the boundary condition

6.2.5 ASR and Hydrostatic Pressure Analysis for Constant Relative Humidity

For the illustration of the concrete gravity dam performance under the influence of ASR expansion, it is assumed that the system is closed where there is no mass flux exchange between the external and internal of the system. This holds the assumption that the reaction extent, $\xi \in [0, 1]$ to be true.

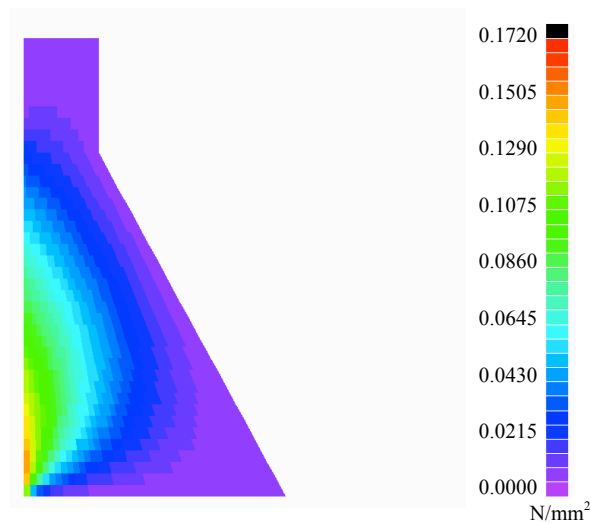


Figure 6.6: Fluid pressure distribution throughout gravity dam due to fluid-structure interaction from the upstream region

Another assumption made is that the gel formation and expansion happens simultaneously, which in theory states that expansion only happens after pore availability is depleted and is not simultaneous to the gel formation. It is also assumed that silica and alkali sources will not deplete or increase due to external sources and that the reaction continues as long as the optimal conditions are satisfied. Figure 6.6 shows the fluid pressure distribution due to the hydrostatic loading as shown in Figure 6.1. The pressure is the highest from the boundary of the loading and decreases throughout the cross-section.

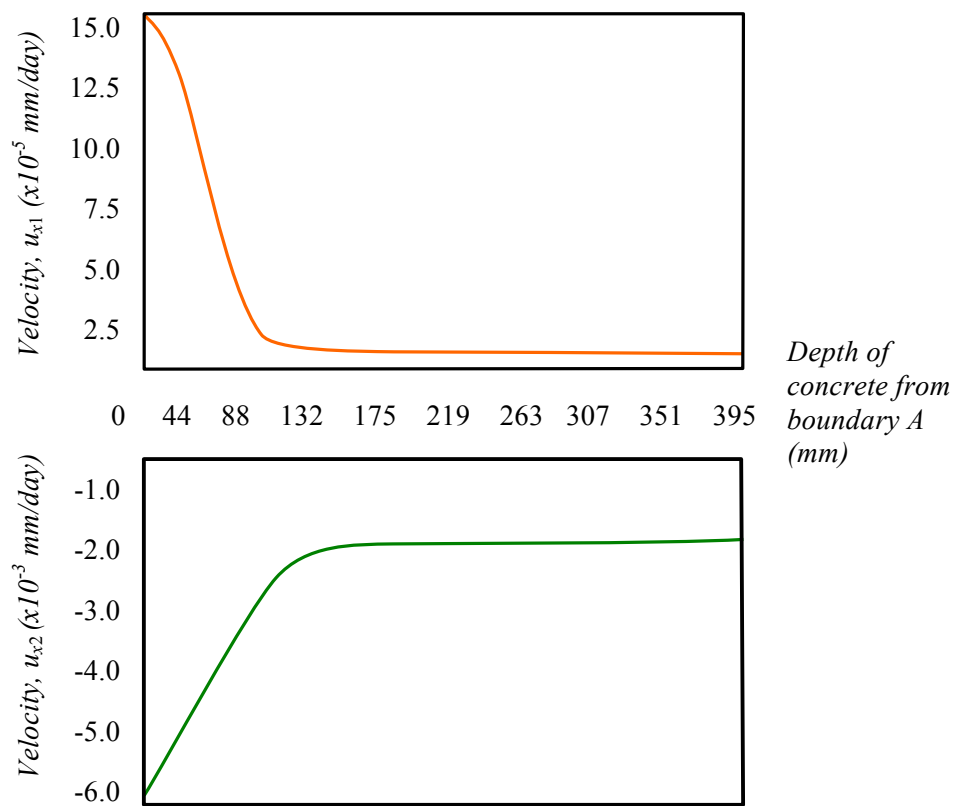


Figure 6.7: Velocity of fluid along the depth of the concrete gravity dam due to fluid pressure

Figure 6.7 displays the fluid velocity due to fluid pressure from the upstream region. The horizontal velocity is mostly influenced by fluid pressure. The vertical velocity is influenced by both fluid pressure and gravity, hence having a higher value in the $-x_2$ direction. It can be seen from the figures that the velocity decreases with the concrete depth. This is influenced by the permeability and porosity of the concrete, which in this case is better studied at the mesoscale level. However, it can be seen that under these circumstances, the value of fluid velocity is close to zero and can be

assumed as negligible. Hence the moisture diffusivity length theory in Section 4.7 by Steffens (2003) will be adapted for this research.

Figure 6.8 shows the displacement contours due to ASR expansion under a constant temperature of 20°C and relative humidity of 80% at 7300 days. Similar to the displacements due to the thermal difference model in Figure 6.3, ASR for an isothermal case causes the dam to expand outwards. However, under the defined material properties and boundary conditions, displacements show that the dam deflects outwards but leans towards the upstream. The stress distributions due to ASR effects throughout the concrete gravity dam in Figure 6.9 show tensile stresses in both the horizontal and vertical directions that reflect the displacement distributions. It also agrees with the findings from Mostagh and Ghaemian (2008), whom upon performing a simulation on an isothermal power plant affected with ASR found that the vertical stress values are lower than horizontal stress values. Under isothermal temperature and relative humidity, the horizontal stress distributions are smeared throughout the cross-section except for the lower region of the dam which is restraint, limiting expansion.

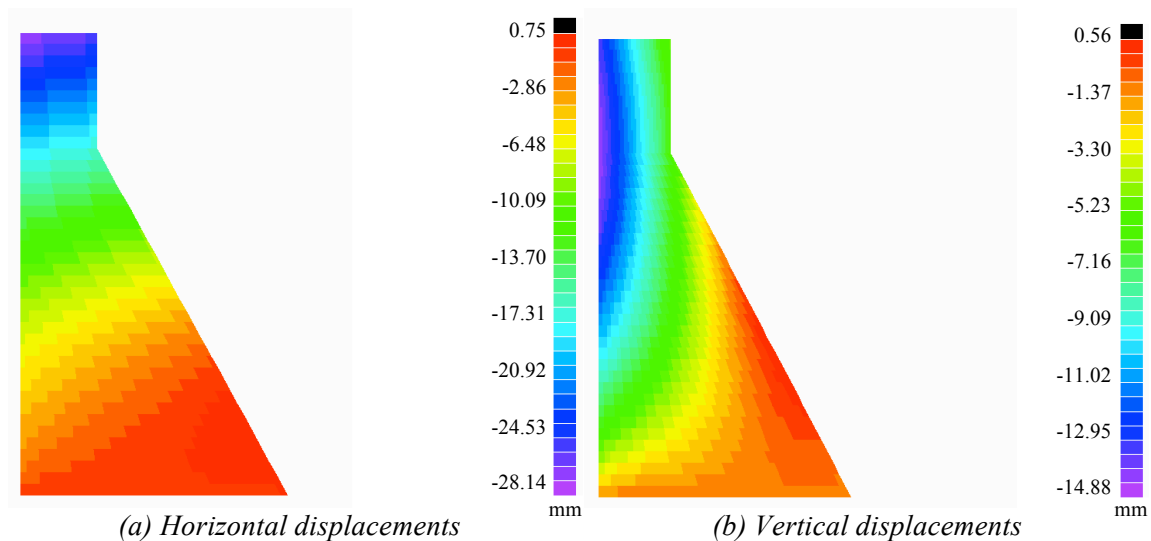


Figure 6.8: Displacements at 7300 days due to ASR expansion and hydrostatic pressure in the dam for an isothermal condition of 20°C with constant relative humidity, characteristic time constant, τ_c and latency time constant, τ_l

The vertical stress distribution has a higher compressive value due to the self-weight of the dam. If we look at Figure 6.10, it can be seen that at approximately 3600 days, damage initiates and hence the stress values at the location where damage orientates starts to lessen. This is reflected in Figure 6.9 where the stresses start to

decrease in the damage regions. Damage in the dam due to ASR initiates at the downstream and spreads inwards and in a smeared manner throughout the dam.

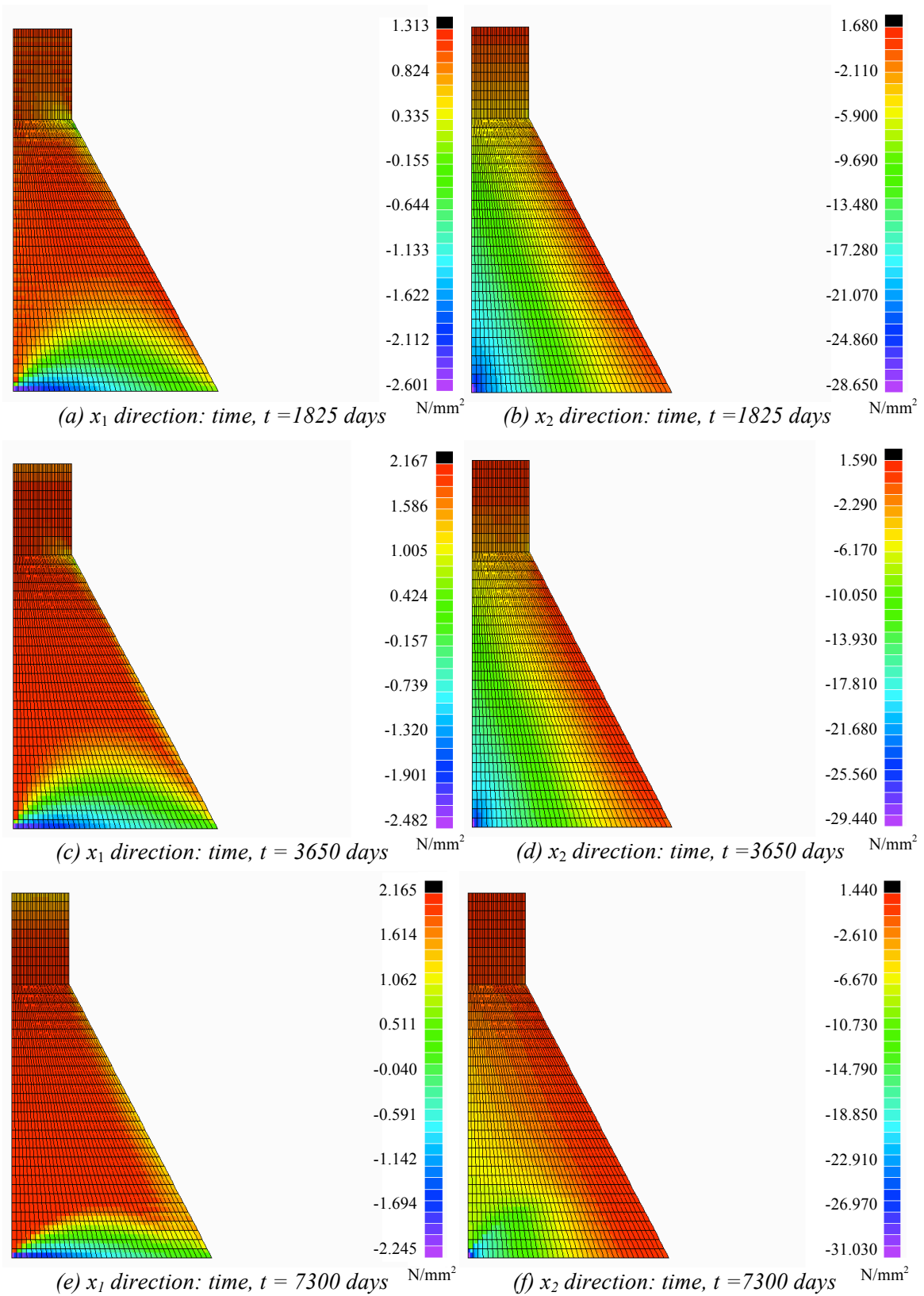
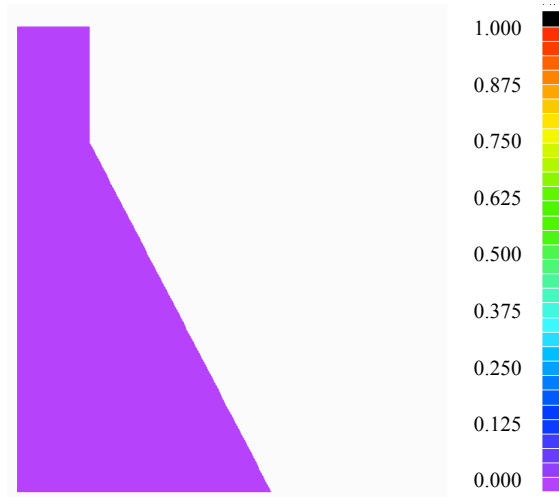
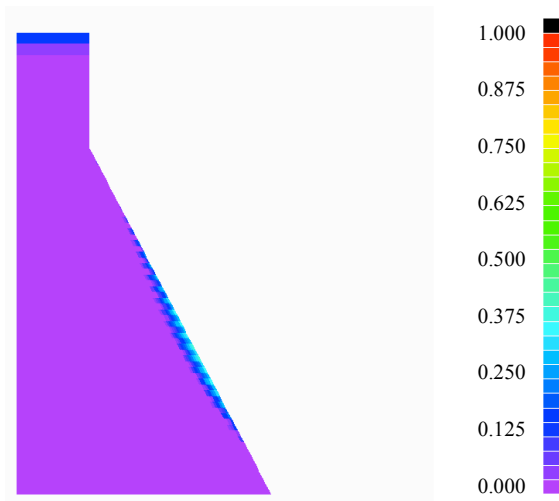


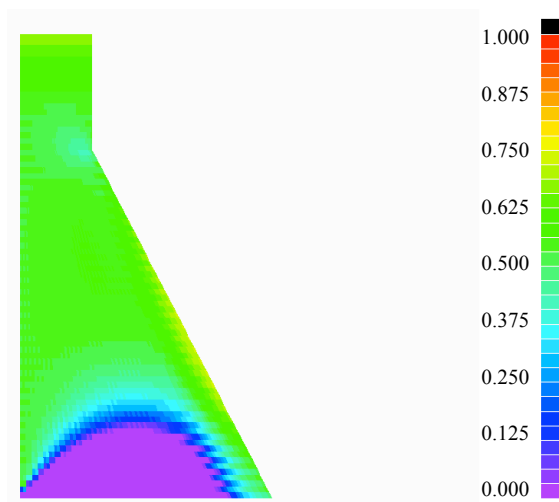
Figure 6.9: Stress distributions in the dam due to ASR expansion and hydrostatic pressure for an isothermal condition of 20°C with constant relative humidity of 80%



(a) Time, $t = 1825$ days



(b) Time, $t = 3650$ days



(c) Time, $t = 7300$ days

Figure 6.10: Damage variable due to ASR expansion and hydrostatic pressure for a constant temperature of 20°C and relative humidity of 80%

6.2.6 ASR and Hydrostatic Pressure Analysis for Varying Relative Humidity

Relative humidity influences the latency and characteristic time constants τ_L and τ_C , which will in turn influence the ASR reaction rate. In this section, the effect of relative humidity will be presented using the same problem as in the previous section but for decreasing values of relative humidity values throughout the domain. Figure 6.11 shows the concrete gravity dam with shaded zones reflecting the different values of relative humidity. Starting from the boundary which is exposed to water, the relative humidity of the region is set to 100% to represent submerged humidity conditions. The relative humidity gradually decreases to 60% moving towards to downstream, which is the minimum threshold value of humidity needed for ASR to initiate. The different zone sizes were calculated from the equation for moisture diffusion length in Equation (4.59), giving the moisture diffusion length in the 100% H zone as 1000 mm and the moisture diffusion length in the 60% H zone as 4000 mm, as shown in Figure 6.11.

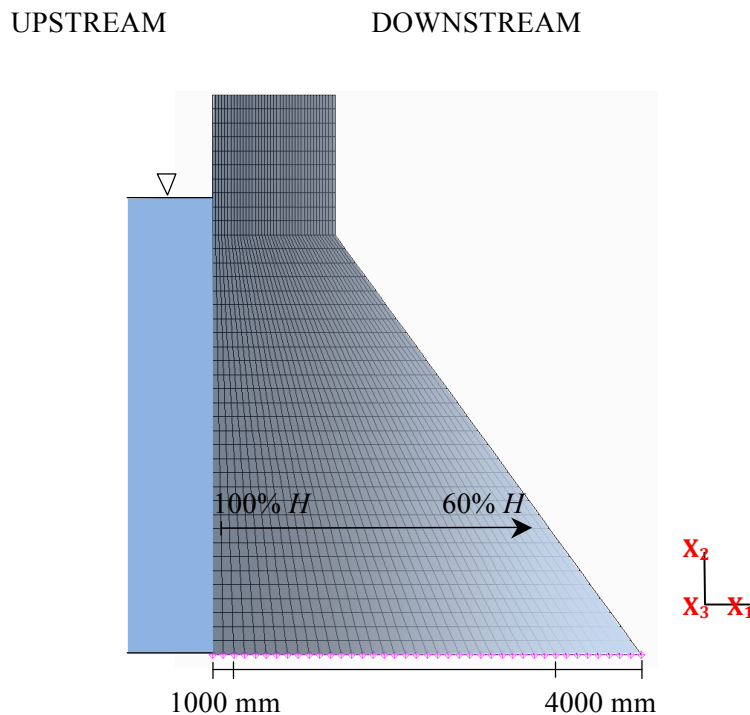


Figure 6.11: Shaded zones depicting different relative humidity conditions ranging from 100% to 60%

Comparing to Figure 6.8, the displacements due to a varied relative humidity in Figure 6.12 is larger since a higher relative humidity causes a more rapid ASR reaction rate, for example, in the 100% H zone. This zone, having the maximum relative

humidity expands faster when compared to the zone which has a relative humidity of 60%, which is the minimum optimal relative humidity condition for ASR reaction to initiate. This causes a high distribution of tensile stresses in that region, larger than the compressive stresses caused by hydrostatic pressure, and larger than the tensile stresses in the downstream region as reflected in Figure 6.13. Seeing that the upstream region expands faster and with larger values than the downstream region, the dam deflects outwards and leans towards the downstream, causing compressive stresses in the vertical direction of the downstream region.

When compared to problems of constant relative humidity in Section 6.2.4, the damage contours for the varying relative humidity in Figure 6.14 is more localized to regions of higher relative humidity. Damage initiates at the zone where relative humidity is 100%, at the upstream region and continues inwards. There is no damage at the regions with the low relative humidity of 60%. However, as for the case of constant relative humidity, under these conditions, ASR reaction takes longer to occur and start causing damage to a structure. Damage for the constant conditions start at approximately 3600 days while damage for the varying relative humidity start at approximately 1800 days, which is twice the time for the constant conditions case. However, after 7300 days damage in the constant conditions case is smeared throughout the dam while damage in the varying relative humidity case is localized at the higher moisture regions.

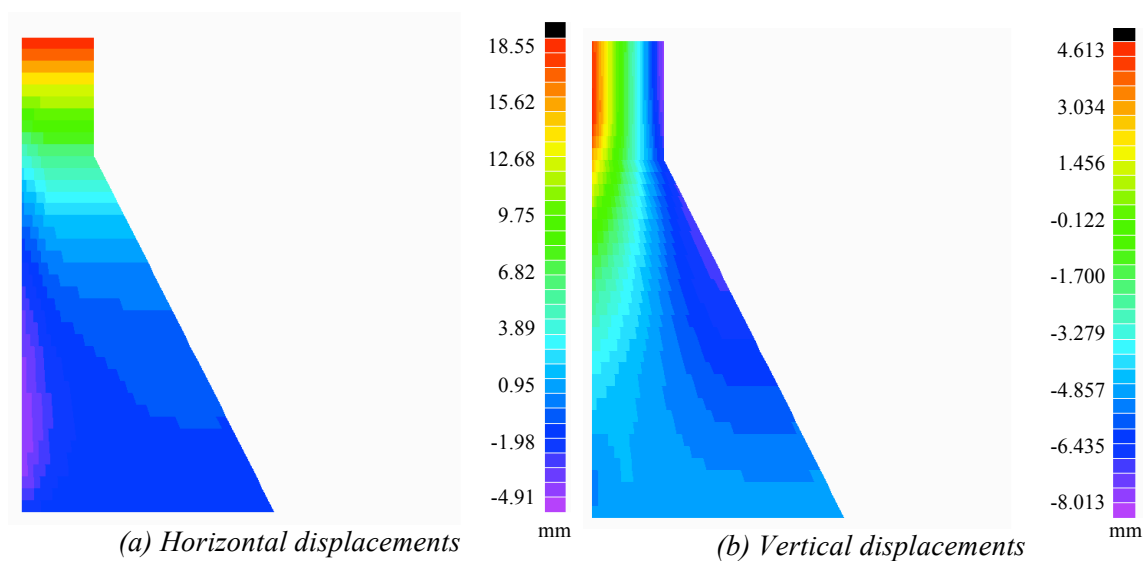


Figure 6.12: Displacements at 7300 days due to ASR in the dam for an isothermal condition of 20°C with varying relative humidity ranging from 60% to 100%

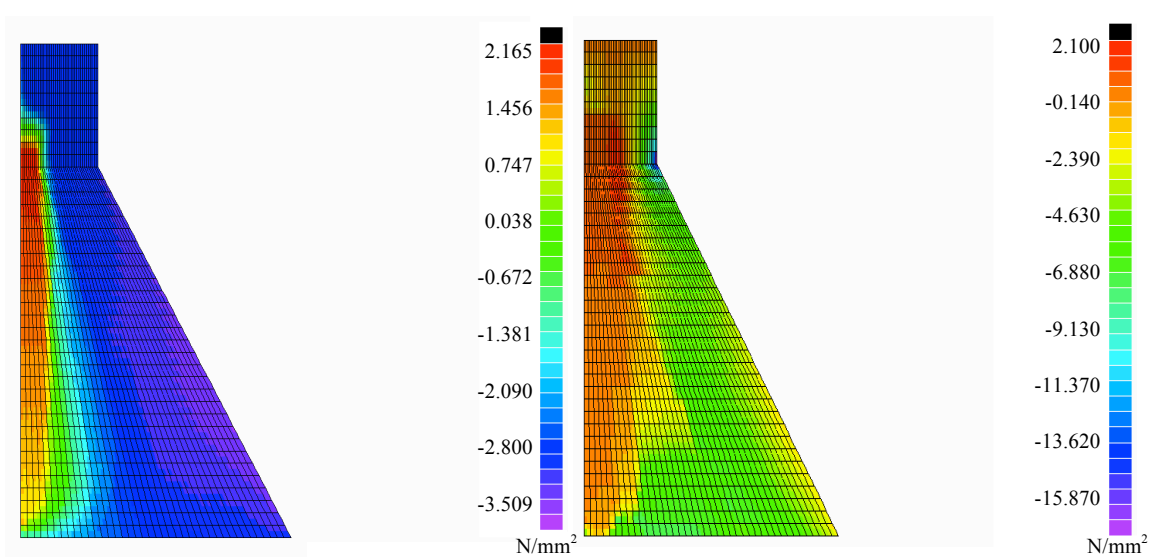
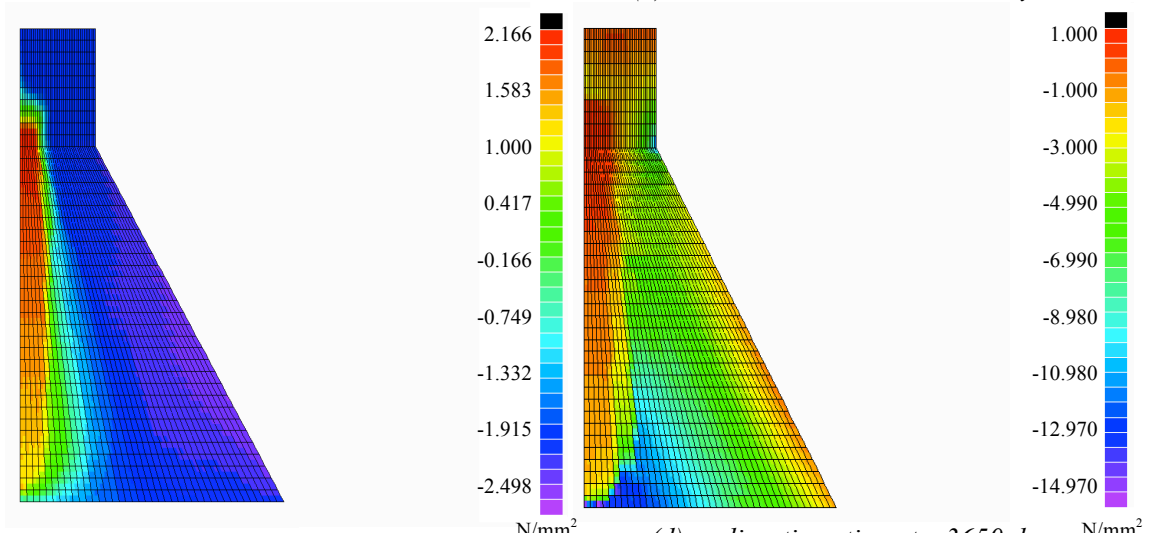
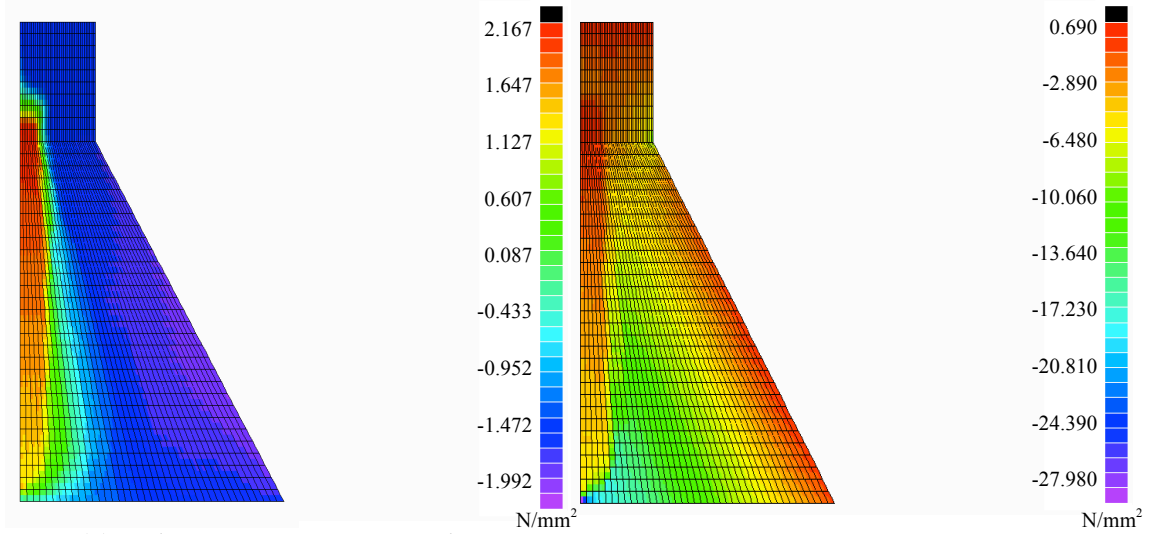
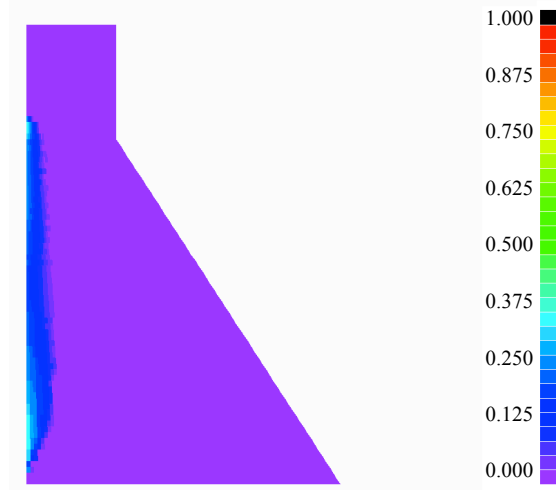
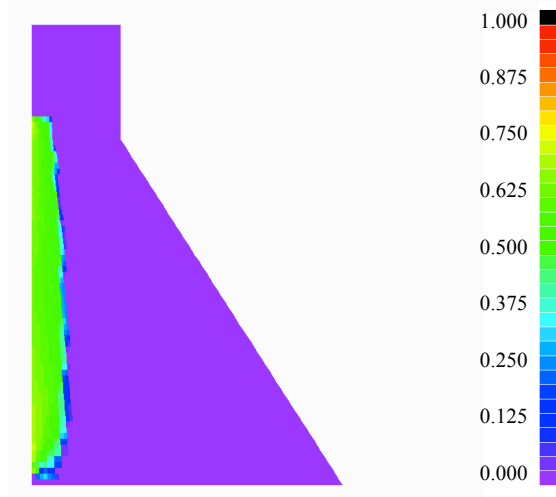


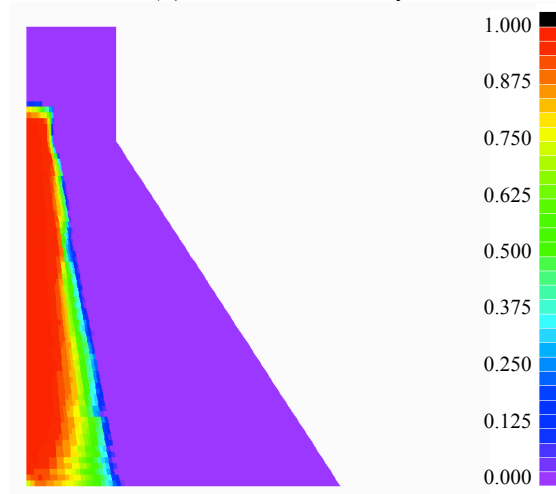
Figure 6.13: Stress distributions due to ASR in the dam for an isothermal condition of 20°C with varying relative humidity ranging from 60% to 100%



(a) Time, $t = 1825$ days



(b) Time, $t = 3650$ days



(c) Time, $t = 7300$ days

Figure 6.14: Damage variable due to ASR and hydrostatic pressure for a constant temperature of 20°C and relative humidity ranging from 60% to 100%

Figure 6.15 shows the curve for ASR reaction extent against time for two relative humidity values of 80% and 100% for Nodes 126 and 513 respectively. The curve follows a sigmoidal shape, where at the start of the reaction, the ASR reaction rate, ξ is 0 meaning that the reaction has not initiated. As the reaction continues the reaction rate increases, its rapidity depending on the temperature as well as the relative humidity. As can be seen, under such circumstances the reaction rate for the relative humidity of 100% happens at a much faster rate than for the relative humidity of 80%. However for both cases, ASR takes a long time until fully reacted, which enables us to conclude that eventhough ASR expansion may cause damage to a concrete structure, additional stresses to the structure accelerates the damage process. The exposure conditions of the structure also determine the orientation and initiation of the ASR damage.

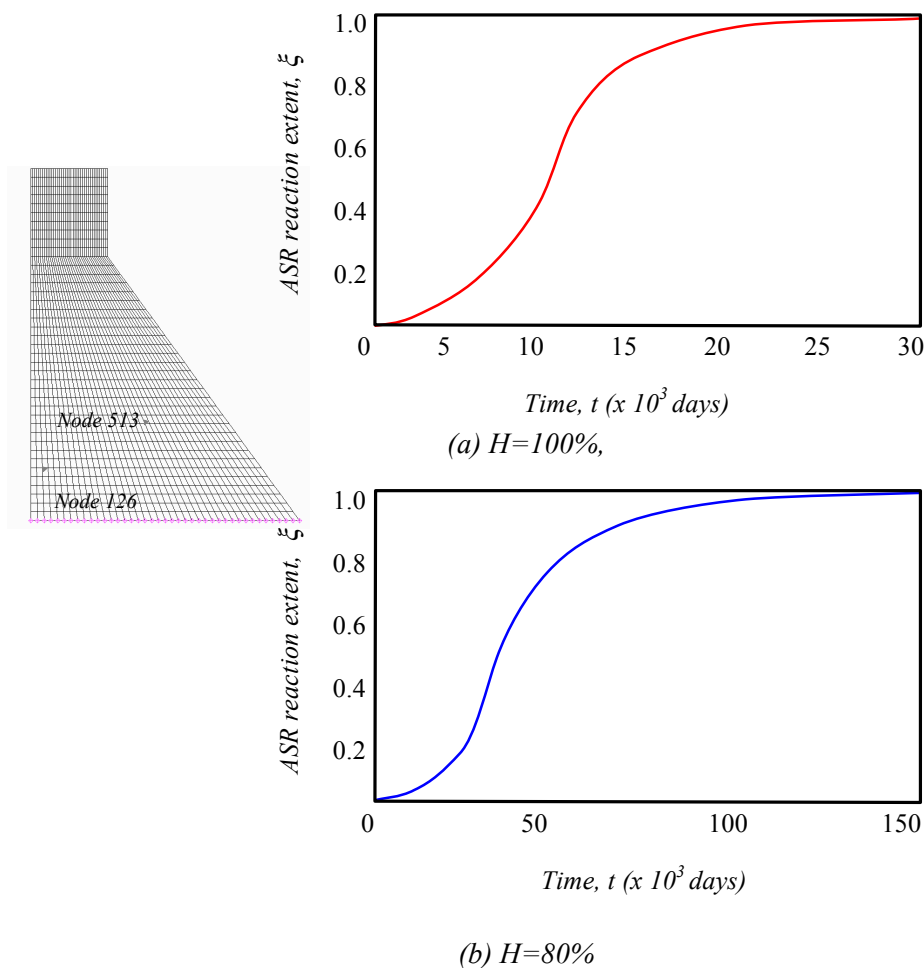


Figure 6.15: ASR reaction extent against time for an isothermal condition of 20°C and relative humidity of 80% and 100%

7 MODELING ASR AT THE MESOSCALE

7.1 INTRODUCTION

Material models at the mesoscopic level help to gain insight into the origin and nature of concrete behavior. Previous works on ASR by Ulm (2000), Larive (1998) and Comi (2009) model concrete as a two-phase material which includes the homogenized skeleton with interstitial pores as a phase and the ASR gel as another. The model presented in this chapter is performed at the mesoscale where the model consists of two phases, the aggregates as one phase and the homogenized skeleton with interstitial pores as the other. Although the problems are not examined in full engineering detail, nor is the porosity of the matrix explicitly simulated, the model is sufficient to demonstrate the workability of the algorithm applied in this research. This has been proven feasible by a series of validation tests conducted with benchmark examples in the following section. This chapter will touch on the fundamentals of mesoscale numerical simulation procedure for concrete, which is the take-and-place method, as well as the general ASR testing methods, and then extended to the ASR testing methods by the Finger-Institut Baustoffkunde (FIB). Results from the ASR testing in FIB will be numerically simulated and a comparison will be made. This is followed by a mesoscale model of ASR deformation for heterogeneous prism in order to study the effects of ASR on concrete at the mesoscale.

7.2 THE CONCEPT OF MESOSCALE MODELING

Mesoscale modeling is an essential tool to predict damage initiation and orientation in a multiphasic material model. Mesoscopic modeling of concrete may consist of aggregates and the cementitious matrix, as well as the interfacial transition zone if required. Wittmann (1984) was the first researcher to have developed a numerical simulation to represent the concrete mesostructure using the finite element method in the 1980s. Since then, mesoscale modeling has been used to solve various engineering problems in concrete structures as well as other materials. In order to perform a mesoscale simulation of concrete, a random generation of aggregate particle size, shape and distribution that resembles real concrete is required, after which the cementitious matrix will fill the remaining space.

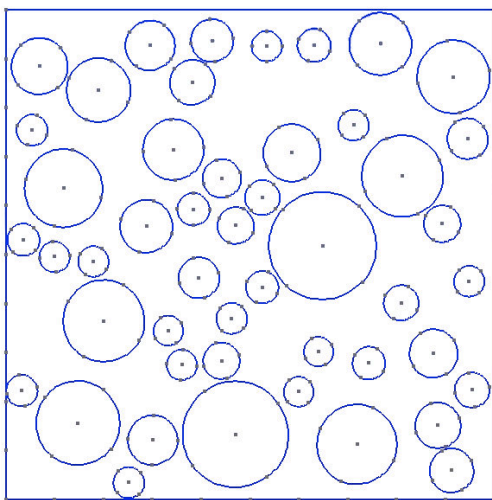
The shape of aggregates is an important factor to consider in mesoscopic simulation of concrete since it affects its mechanical behavior. Different aggregate particle shapes have different influences on the stress distribution and orientation within the concrete composite (Häffner 2007). For example, a more angular-shaped aggregate particle will subject the concrete to stress localization, which in turn influences the location of cracking initiation. Some past researches by Bazant (1990), and Schlangen and van Mier (1992) have dealt with circular aggregate particles while Wittmann et.al (1984) simulated rounded aggregate particles and Wang (1999) worked with crushed as well as rounded aggregate particles.

Wang (1999) also produced angular-shaped aggregate particles from polygons with elongation ratios. Three-dimensional mesoscale models were developed by Bazant (1990), Schlangen and Mier (1992), and further enhanced by Guidoum and Navi (1993), who all assumed the aggregate particles to have spherical shapes. Leite (2004), Häffner (2007) and Eckardt (2009) dealt with ellipsoidal functions with varying parameters for various aggregate particle shapes which can be switched from spheres to ellipsoids by changing the parameter.

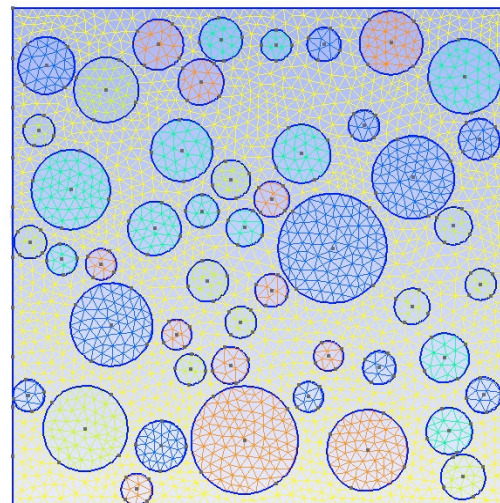
To develop a feasible concrete mesoscale model, the aggregate particle distribution must satisfy as closely as possible the basic statistical characteristics of real concrete material with a macroscopically homogeneous and isotropic spatial distribution (Wriggers 2006, Bazant 1990). In order to achieve this, Wang (1999) developed an aggregate random sampling method using the principle of Monte

Carlo's simulation to generate random aggregate particles in a given concrete model. He then developed a method for generating finite element mesh to study the nonlinear behavior of concrete called the take-and-place method. In this method, aggregate particles are generated randomly according to a selected aggregate grading curve and then placed one by one into the model in such a way that it is not overlapping with either other aggregates that were previously placed or with the specimen boundary surfaces. Then mortar will be placed into the voids in between the aggregates, filling the space between them.

The take-and-place method is separated into two processes, the take process where the aggregate particle shape distribution is defined, and the place process, where the size distribution of the aggregate particles is fulfilled. Figure 7.1 (a) shows a mesoscopic model containing randomly generated aggregate particles. The void in between the particles will be filled with cementitious matrix. Figure 7.1 (b) shows the same model but with finite element meshing. This model will be used for finite element analysis.



(a) Random aggregates placed in a prism with mortar matrix placed in between



(b) Finite element model meshing of prism in (a) using 3-noded plane elements

Figure 7.1: The take-and-place method for finite element meshing in mesoscale modeling

More detailed description for this method can be found in literature by Bazant (1990), Schlangen and Mier (1992), Wittmann et.al. (1984), Wang (1999), and more recently by Häffner (2007) and Eckardt (2009).

7.2.1 Aggregate Particles Shape Distribution (Take Process)

In the take process, the aggregate particle shape distribution is first determined. The volume of the aggregate particles according to the aggregate grading size is calculated. Then, a random number defining the size of an aggregate particle from the largest class is generated, after which its volume is calculated and subtracted from the total aggregate volume. This process is repeated until all the aggregate particles in that particular size range have been calculated. The process is then continued for the following grading size group.

One method of describing the aggregate grading curve is the Fuller's curve (Fuller 1907), which can be represented by the curve in Figure 7.2 or also represented by Equation (7.1):

$$P(d) = 100 \left(\frac{d}{d_{\max}} \right)^n \quad (7.1)$$

Where $P(d)$ is the cumulative percentage passing a sieve for an aperture diameter d , the term d_{\max} is the maximum size of aggregate particles and n is the exponent of the equation within the range of 0.45 to 0.70 (Wriggers 2006).

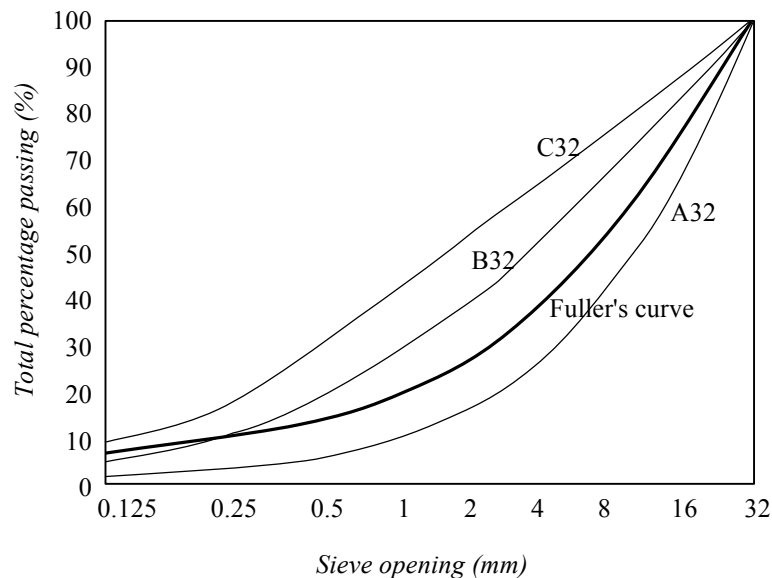


Figure 7.2: Fuller and limiting grading curves (Wriggers 2006)

B32 and A32 are the ideal range limits and C32 is the upper limit for the aggregate size distribution.

Concrete at the mesoscale is a heterogeneous and multiphasic material. The usual mix design states that aggregate contents in a given concrete should normally consist of between 60% to 90% of its volume (Häffner 2006). The aggregate size distribution in concrete is determined from the sieve analysis, which will give us the grading size ranges for fine and coarse aggregates in an aggregate sample, where according to Wriggers (2006), between 40% to 50% of the concrete volume is usually taken up by coarse aggregates. The amount of coarse aggregates can be calculated using the aggregate volume fraction, ϕ_p (Wriggers 2006):

$$\phi_p = \frac{w_p}{Y_p V_T} \quad (7.2)$$

Where w_p is the total weight of the aggregate particles, Y_p is the specific weight and V_T is the total volume of the specimen.

The volume of aggregates, V_p within a grading class bound between a minimum coarse aggregate particle size, d_{min} and a maximum coarse aggregate particle size, d_{max} is given by (Wriggers 2006):

$$V_p(d_{min}, d_{max}) = \phi_p V_T \frac{P(d_{min}) - P(d_{max})}{P(d_{max}) - P(d_{min})} \quad (7.3)$$

Where d is the aperture diameter of the sieve.

The approximation of the aggregate particle surface is given by Zohdi (2001) and Häffner (2007) as:

$$\left(\frac{x_1}{r_1}\right)^n + \left(\frac{x_2}{r_2}\right)^n + \left(\frac{x_3}{r_3}\right)^n = 1 \quad (7.4)$$

The term x_i in Equation (7.4) refers to the axes with $i=1, 2, 3$. The variable exponent, n determines the shape of the aggregate as can be seen in Figure 7.3. Changing the value of n results in different aggregate shapes.

The term r is the radii and can be expressed as a function of the second largest radius r_2 , where according to Eckardt (2009) is defined as:

$$r_1 = \left(1 + X_2 \frac{\eta_{13} - 1}{\eta_{13} + 1}\right) r_2 \quad r_3 = \left(1 - X_3 \frac{\eta_{13} - 1}{\eta_{13} + 1}\right) r_2 \quad (7.5)$$

Where X_2 and X_3 are uniformly distributed random numbers between 0 and 1. The parameter η_{13} defines the maximum ratio between the radii r_1 and r_3 and controls the shape of the aggregate particle. Eckardt (2009) states that taking η_{13} as 1 will generate spherical particles while a higher value of η_{13} will generate ellipsoids.

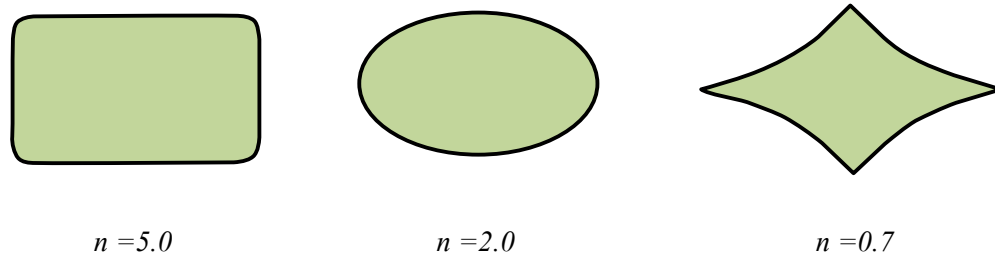


Figure 7.3: Shapes aggregate particles due to modified ellipsoids function (Häffner 2006)

According to Eckardt (2009), the expected value of the volume of an aggregate particle, $E(V)$ can be expressed as a function of r_2 :

$$E(V) = \frac{4}{3} \pi r_2^3 \left(1 - \frac{1}{2} \frac{\eta_{13} - 1}{\eta_{13} + 1}\right) \left(1 + \frac{1}{2} \frac{\eta_{13} - 1}{\eta_{13} + 1}\right) \quad (7.6)$$

The division of aggregate particles into mineral classes according to the aggregate grading curve is bound to the minimum aggregate diameter, d_{min} and maximum aggregate diameter, d_{max} . The mass fraction of aggregate, ϕ_m for one mineral class is defined from Eckardt (2009) to be:

$$\phi_m(d_{eqv}) = \frac{\ln d_{eqv}}{\ln d_{max} - \ln d_{min}} - \frac{\ln d_{min}}{\ln d_{max} - \ln d_{min}} \quad (7.7)$$

Where d_{eqv} is the equivalent diameter of the aggregate particle. ϕ_m at a given diameter, d represents the mass fraction of aggregates, where d_{eqv} is smaller than d .

The density function for a given mineral class is obtained by differentiating ϕ_m :

$$\rho_m(d_{eqv}) = \frac{d\phi_m}{dd_{eqv}} = \frac{1}{(\ln d_{\max} - \ln d_{\min})d_{eqv}} \quad (7.8)$$

And the accumulative distribution function, ϕ_d (Eckardt 2009):

$$\begin{aligned} \phi_d(d_{eqv}) &= \int_{d=d_{\min}}^{d_{eqv}} \rho_d(d) dd \\ &= \frac{d_{\min}^3 d_{\max}^3}{d_{\max}^3 - d_{\min}^3} \left(\frac{1}{d_{\min}^3} - \frac{1}{d_{eqv}^3} \right) \end{aligned} \quad (7.9)$$

The equivalent diameter of the aggregate, d_{eqv} is generated according the following equation:

$$d_{eqv} = 2r_2 = \frac{d_{\max} d_{\min}}{\sqrt[3]{Xd_{\min}^3 + (1-X)d_{\max}^3}} \quad (7.10)$$

Where ($0 \leq X \leq 1$).

7.2.2 Aggregate Particles Size Distribution (Place Process)

Placing of the aggregate particles starts one by one with the particles with the largest volume. Some requirements for this placing process are that the aggregate particles must have no overlapping boundaries with the specimen surface or other previously placed particles, and the minimum distance between the aggregate particles and to the specimen surface boundaries must be fulfilled (Wriggers 2006). Wang (1999) stated that the generation of the aggregate particle coordinates are made in terms of the local coordinates with respect to a reference point O inside the particle. When placed in the specimen, its position and orientation are defined by the x_1 and x_2 coordinates of the reference point O and the phase angle, χ .

The coordinates O may be obtained as (Wang 1999, Wriggers 2006):

$$x_{1,O} = x_{1,\min} + \eta_1(x_{1,\max} - x_{1,\min}) \quad x_{2,O} = x_{2,\min} + \eta_2(x_{2,\max} - x_{2,\min}) \quad (7.11)$$

Where $x_{1,O}$ and $x_{2,O}$ are the coordinates of O , the terms $x_{1,\min}$, $x_{1,\max}$, $x_{2,\min}$ and $x_{2,\max}$ are the minimum and maximum x_1 and x_2 coordinates of the concrete area, and η_1 and η_2 are two independent random numbers uniformly distributed between 0 and 1.

The placement and position of the ellipsoids according to Eckardt (2009) however, is defined by center points coordinates c_{x1} , c_{x2} and c_{x3} and Euler angles α , β and γ . During placements, these parameters are computed using uniformly distributed random variables. A valid parameter set is obtained if the ellipsoids are completely inside the specimen and if there are no overlapping regions with already placed ellipsoids. If not, the ellipsoid position and orientation will be recalculated and the testing procedure repeated. Then the ellipsoids separation is checked using an algorithm from Wang (2001), Häffner (2007) and Eckardt (2009) that uses a matrix representation of an ellipsoid:

$$\mathbf{x}^T \mathbf{A} \mathbf{x} = 0 \quad (7.12)$$

Where $\mathbf{x} = [x_1, x_2, x_3, 1]^T$ are homogeneous coordinates of an ellipsoid particle and \mathbf{A} is a 4x4 matrix that represents the radii, position and orientation in space for that ellipsoid (Eckardt 2009). The vector \mathbf{A} is given by:

$$\mathbf{A} = \mathbf{D}_t^T \mathbf{D}_r^T \bar{\mathbf{A}} \mathbf{D}_r \mathbf{D}_t \quad (7.13)$$

Where \mathbf{D}_t and \mathbf{D}_r are the transformation matrices for translations and rotations and are represented by:

$$\mathbf{D}_t = \begin{bmatrix} 1 & 0 & 0 & -c_{x1} \\ 0 & 1 & 0 & -c_{x2} \\ 0 & 0 & 1 & -c_{x3} \\ 0 & 0 & 0 & 1 \end{bmatrix} \quad (7.14)$$

$$\mathbf{D}_r = \begin{bmatrix} \cos\phi \cos\gamma - \cos\alpha \sin\beta \sin\gamma & \sin\beta \cos\gamma + \cos\alpha \cos\beta \sin\gamma & \sin\alpha \sin\gamma & 0 \\ -\cos\beta \sin\gamma - \cos\alpha \sin\beta \cos\gamma & -\sin\beta \sin\gamma + \cos\alpha \cos\beta \cos\gamma & \sin\alpha \cos\gamma & 0 \\ \sin\alpha \sin\beta & -\sin\alpha \cos\beta & \cos\alpha & 0 \\ 0 & 0 & 0 & 1 \end{bmatrix} \quad (7.15)$$

And $\bar{\mathbf{A}}$ is a matrix for an ellipsoid with its center at the origin and the radii aligned with the coordinate axes:

$$\bar{\mathbf{A}} = \begin{bmatrix} \frac{1}{r_1^2} & 0 & 0 & 0 \\ 0 & \frac{1}{r_2^2} & 0 & 0 \\ 0 & 0 & \frac{1}{r_3^2} & 0 \\ 0 & 0 & 0 & -1 \end{bmatrix} \quad (7.16)$$

The separation between two ellipsoids is determined by evaluating the characteristic polynomial, $f(\lambda)$ defined as (Häffner 2007, Eckardt 2009):

$$f(\lambda) = \det(\lambda \mathbf{A}_1 + \mathbf{A}_2) \quad (7.17)$$

Detailed explanation on this matter can be found from Häfner (2007).

7.3 ASR TESTING METHODS

Numerous testing methods have been developed to investigate alkali-aggregate reactivity, for example the concrete microbar test, the accelerated mortar bar test, the concrete prism test, the German dissolution test and the quick chemical test. All these tests follow different guidelines, for instance, the chemical test is a rapid method that follows the ASTM C-289-81. The concrete microbar test is an adaptation of a Chinese test developed by Xu (2000). It was initially used to determine alkali-carbonate reactive aggregates but later modified to determine ASR. The test method is similar to the ASTM C-1260-05 method.

The German dissolution test procedures are given in the Guidelines for Alkali-Aggregate Reactions in Concrete issued in 1986 by the German Committee for Reinforced Concrete. The accelerated mortar bar test methods, which is a modified version of the ASTM C-227 mortar bar test is performed according to the ASTM C-1260-94. An advantage of the accelerated mortar bar test is that it gives rapid results when compared to other performance tests. Numerous accelerated mortar bar tests have been developed from an adapted version of the NBRI-mortar bar test that was introduced by Oberholster and Davies (1986) including the Danish Method, the South Africa Method, the Chinese Method and the Japanese Method.

There is no single testing method that can be universally applied for all aggregates. For instance, the chemical test cannot be used with all types of aggregates and furthermore, it does not give an estimate of the potential aggregate. The German dissolution test is only applicable to opal-bearing aggregates with particle sizes above 1 mm and aggregates containing reactive flint in the size range of 1 mm to 4 mm. Therefore, different testing methods are needed to determine different types of aggregates under different conditions. The test methods mentioned above are often used as a basis for further modification by researchers in order to accommodate the various types of aggregates.

At the Finger-Institut Baustoffkunde (FIB), testing for alkali-silica reactivity in aggregates is conducted with a combination of petrography and mineralogy examinations and a modified version of the LMPA accelerated mortar bar test facilitated with the use of a climate chamber for simulation of environmental conditions. The LMPA accelerated mortar bar test is similar to the accelerated mortar bar test by RILEM test method AAR-2. Other tests conducted by the FIB include ASR performance tests for specific concrete mixture in the cyclic climate simulation chamber. The following section outlines the details of the test methods practiced by the FIB as outlined by Stark (2008).

7.3.1 Petrography

Petrography enables the identification of the various forms of silica in aggregates. This makes it an essential method to identify deleterious constituents in a given aggregate which is usually recognized from certain minerals, rock types or specific microstructural features that have been known to cause deterioration in concrete. The procedures for a petrographic examination of aggregates for concrete purposes are given in national codes, an example is the ASTM C-295-08 (Standard Guide for Petrographic Examination of Aggregates for Concrete 1994). Aggregates that are to be tested for its silica reactivity will be examined for the nature of its constituents and the relationships between texture, structure, composition and alterations to its properties (DePuy 1990).

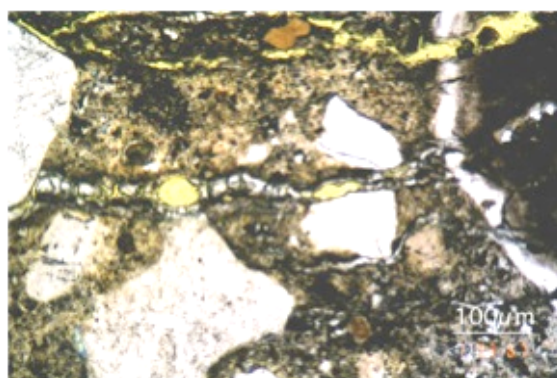


Figure 7.4: Cracking through the aggregate and cementitious matrix due to ASR obtained from petrography examination (Stark 2008)

7.3.2 Mortar Bar Test

The researchers at the FIB have attempted to modify the mortar bar test as an alternative procedure to the Alkali Guideline in DAfStb (Part 3, Series February 2007). The mortar bar test used to evaluate the alkali-silica reactivity in slow and late aggregates was modified from the LMPA Sachsen-Anhalt. The test is based on the South African NBRI-Test (Oberholster & Davies 1986) and has been recognized by international standards like ASTM C-1260, CSA A23.2-25A. The sand used in the test is chosen in order to examine its reactivity. Specimens were cast with the dimensions of 40 x 40 x 160 mm. The prisms are then stored at 70°C in a water bath in closed containers as shown in Figure 7.5. The measurements for length and mass

change are done periodically on the fourteenth, twenty first and twenty eighth days at the prism temperature of 20°C to maintain the consistency of conditions during measurement (Stark 2008).

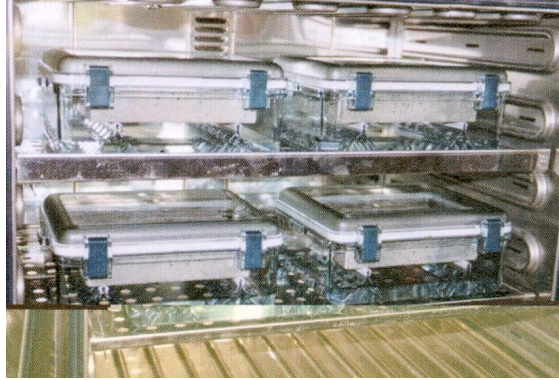


Figure 7.5: Storage of the prisms in water baths at 70°C in closed containers (Stark 2008)

Expansion limit	
≤ 1.5 mm/m	Non-reactive. Aggregate is suitable for use.
1.5 – 2.0 mm/m	Potentially reactive alkali. Aggregate is not suitable for use without concrete testing (Performance testing for concrete with the said aggregate).
> 2.0 mm/m	Reactive alkali. Aggregate is not suitable for use. Concrete testing is possible, but with the probability of an increasing mortar bar test expansion value.

Table 7.1: Limit for expansion for mortar bar tests after 28 days for aggregates (Stark 2008)

The evaluation of aggregate expansion in Table 7.1 follows the guidelines from the Bundesministeriums für Verkehr, Bau und Stadtentwicklung Nr. 12/2006 (ARS 12/2006). The deviating definition of the expansion limit from 1.5 mm/m to 2.0 mm/m is similar to the limit value by the LMPA Sachsen-Anhalt (Philipp and Eifert 2004) and is also based on the elimination of the thermal expansion effects since prisms are kept at a moderate temperature from 70°C and within the range of $20 \pm 2^\circ\text{C}$. Aggregates with expansion ≤ 1.5 mm/m after 28 days of testing is considered unreactive under the ARS 12/2006. Aggregates that fall into the category of > 1.5

mm/m is not necessarily assumed to be reactive. Such aggregates need to be further tested for performance first. Once results from the performance test show that a particular aggregate is in fact deleterious, only then will it be truly considered as reactive. Aggregates with more than 2.0 mm/m expansions are categorized as reactive and unsuitable to be used for concrete construction.

7.3.3 ASR Performance Test

All performance tests for alkali-silica reactivity in aggregates at the FIB are conducted using the cyclic climate chamber. The performance test by this method is a simplified and time-lapsing simulation of different conditions like drying, moistening and freeze-thawing and their complex interaction (Stark and Seyfarth 2008). This allows the initiation and acceleration of potential damaging processes in the concrete structure by intensification of transport and reaction processes. It also exposes the tested concrete to in-situ conditions, ensuring optimal exposure to reactants for optimum reaction conditions.

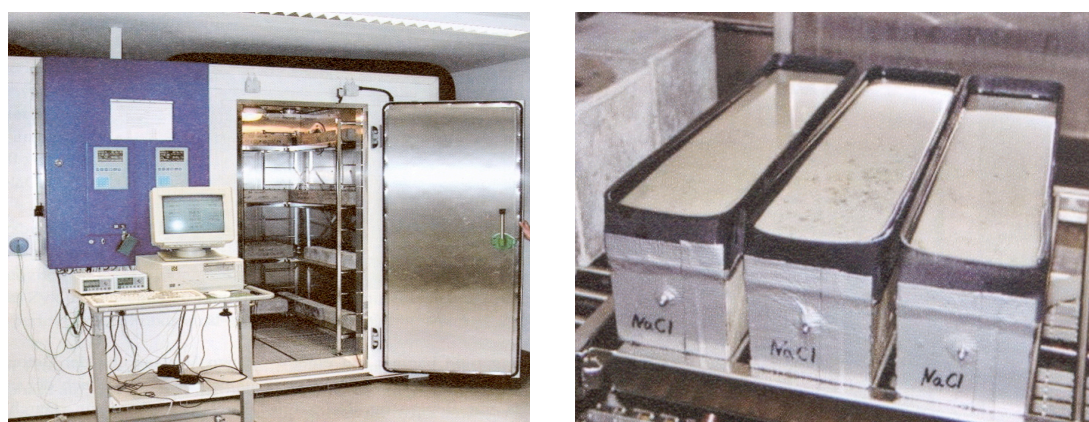


Figure 7.6: (a) The climate chamber used to simulate environmental conditions for ASR performance tests at the FIB, (b) Concrete prisms exposed to deicing solutions for ASR performance testing (Stark 2008)

The temperature conditions in the chamber can be set ranging from -40°C to $+90^{\circ}\text{C}$. It is also capable of simulating freezing, thawing, fogging and drying conditions. The temperature changing rate is up to 5 K/min. Moisture condition in the chamber ranges from 5% relative humidity, H to 100% H . Moistening at 100% H simulates conditions of fog while drying is simulated at $<10\%$ H (Stark 2008).

Investigations are conducted within the guidelines of Zusätzlichen Technischen Vertragsbedingungen und Richtlinien für Ingenieurbauten (ZTV) on building projects under conditions without alkali supply, and with intensive dampness caused by fogging due to a water bath at dew point kept at moderate temperature at the base of the climate chamber. Investigations from the ZTV Beton-StB 01, ARS 12/2006 on the other hand, considers alkali from external sources obtained from the use of deicing solutions on concrete surfaces (Stark 2008).

For the performance test, concrete prisms are prepared according to the Swedish slab test as shown in Figure 7.6 (b). As outlined in Section 4.24, one major influence in ASR is alkali from external source, which is mostly supplied from deicing solution. To simulate the effect of deicing solution on ASR, the prisms are exposed to deicing solutions or water on the top surface of the prism, which is then stored in the climate chamber. Hence the effect of additional source of alkali or moisture can be investigated.

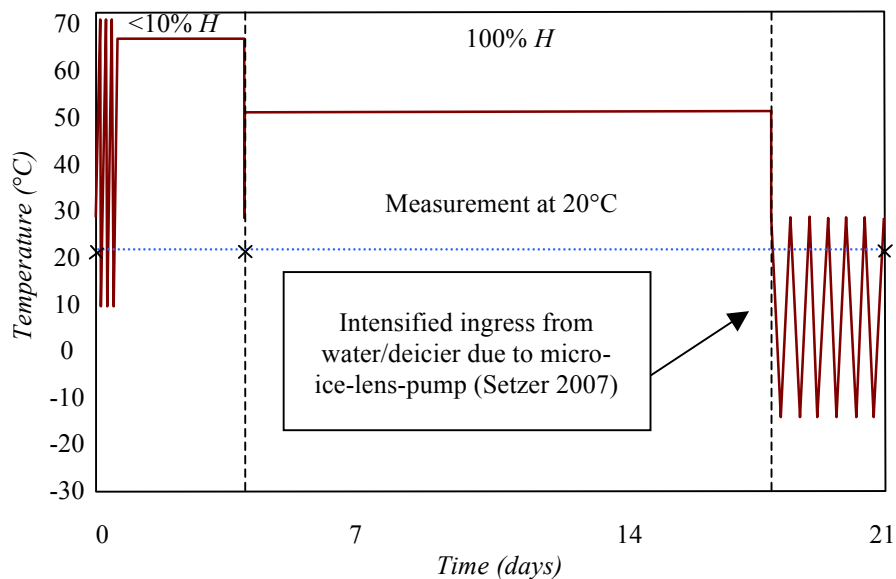


Figure 7.7: ASR climate chamber storage cycle (Stark 2008)

Temperature conditions in the climate chamber follows a 21-day cycle as shown in Figure 7.7. Before placing the prisms in the climate chamber, the initial length measurements were taken at 20°C. Temperature fluctuations from 5°C to 65°C are introduced to promote initial cracking. The prisms are then exposed to a drying period of 4 days at 60°C and a relative humidity of <10%. The temperature is then brought

down to 20°C and measured for length change, after which a fogging temperature will be subjected for 18 days at 45°C at 100% relative humidity. The prism length change is then measured again at 20°C. This stage is followed by a period of freezing and thawing for 3 days, at which temperature ranges from -20°C to 20°C, which is ended by a final measurement of the prism length change (Stark 2008).

Usual mix proportions are made from a selected ratio of cement/fine reactive aggregate by weight for a specific cement content and water/cement ratio. Specimens will be prepared for ASR mixes with deicing solutions exposed to the top surface, as well as a control mix where just water is exposed to the surface. In order to accelerate the effects of ASR process, ordinary Portland cement with high alkali content is used. Hobbs (1988) proved that rapid and drastic variations of temperature due to seasonal changes are very small and only affect the surface of the structure since change in concrete due to temperature is slow and limited. Plus, ASR deformation may take a long time to evolve. Hence, investigation of the long-term ASR process with a temperature history should be considered. However, due to temporal and financial constraints, this is not always possible. Therefore, the FIB mortar bar tests performed in cyclic chamber gives us a faster outlook to the ASR deformation influenced by temperature and moisture in the long-term for an accelerated case.

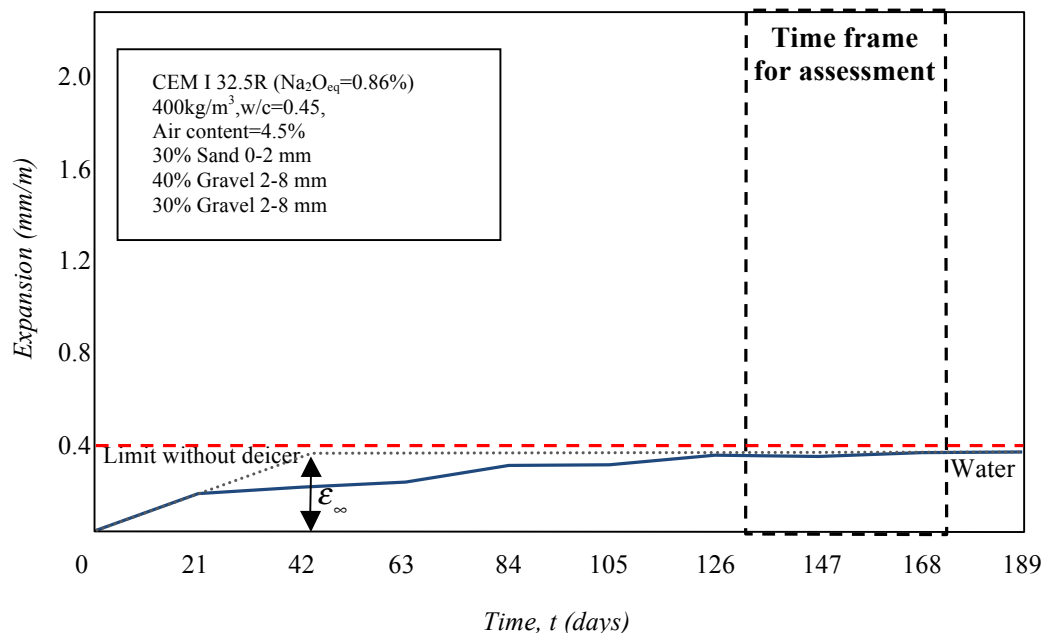


Figure 7.8: ASR expansion (mm/m) over time (days) for concrete prism exposed to water or deicing salt solution (Stark 2008)

An example of ASR gel expansion from mortar bar tests is shown in Figure 7.8. According to Stark (2008), the limit of expansion for ASR performance test is set to 0.4 mm/m without deicing solution. Aggregates that cause expansion over 0.4 mm/m is considered as reactive. Bangert (2004) explains that the volumetric expansion ϵ_{∞} is represented with the height of the graph. This parameter is used for an inverse analysis for ASR simulation in the next section.

7.4 MESOSCALE SIMULATION OF AN ASR EXPANSION ANALYSIS

7.4.1 Modeling Parameters

Assume a two-dimensional mesoscale model of a concrete prism used for FIB testing measuring 100 mm x 100 mm as described in Section 7.3.3. The mesoscale model is made up of a two-phased heterogeneous material consisting of aggregates as a phase and the cementitious matrix with interstitial pores as another phase. The mesoscale model is made up of 9651 three-noded plane elements with a total of 28953 nodes.

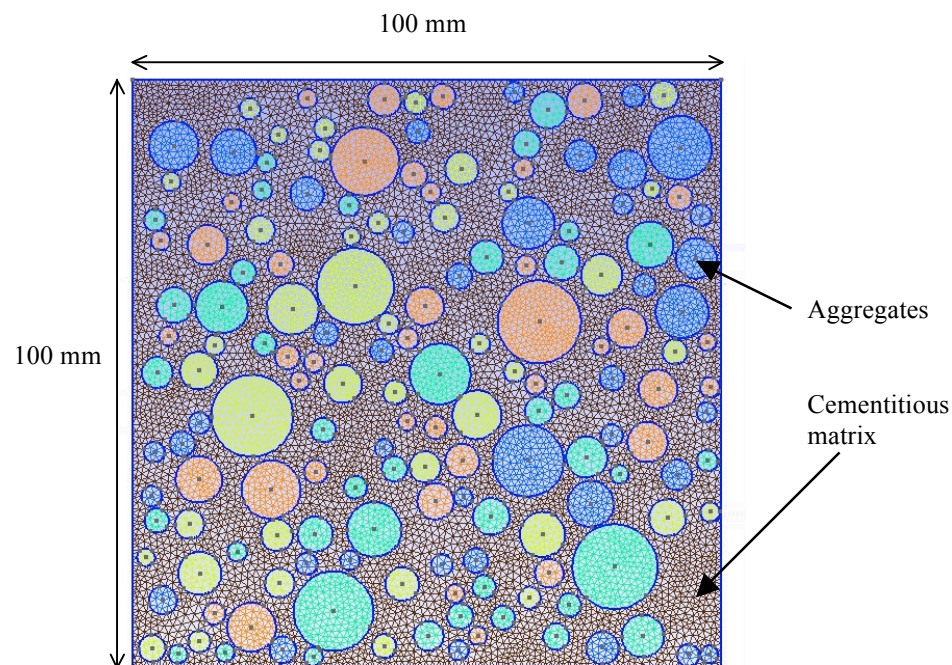


Figure 7.9: Finite element model of the two-dimensional three-noded plane elements mesoscale model of a 100 mm x 100 mm concrete prism

The number of degrees of freedom for heat elements is 28953 with one degree of freedom per node and the number of degrees of freedom for ASR and mechanically loaded elements are 57906 with two degrees of freedom per node to accommodate for the x_1 and x_2 directions. When compared to the macroscale level in Chapter Six which has much larger dimensions of 20000 mm x 14009.5 mm (at the largest cross-section), the macroscale model only has 1681 nodes, 1600 elements and 3362 degrees of freedom, which is substantially lesser from the mesoscale model which is only 100 mm x 100 mm in size.

The model is restraint in the x_2 direction along the lower boundary and x_1 direction along the left boundary and in both directions at the lower left corner node. The boundary conditions have been set for the effects that are taken into consideration, in this particular case, thermal and moisture fluctuations. The boundary conditions for temperature and relative humidity of the prism vary according to experimental setting. The prism is exposed to 8 cycles of the 21-day temperature and humidity fluctuations outlined in 7.3.3, where the model is subjected to drying, fogging, freezing and thawing, and exposed to temperatures ranging from 65°C to -20°C and humidity ranging from <10% to 100% within one cycle.

Material properties for concrete	Aggregate	Mortar
Thermal conductivity of concrete, k (W/mK)	5.00	1.73
Specific heat capacity of concrete, C_v (J/gK)	790	730
Initial latency time constant, τ_L (days)	25	25
Initial characteristic time constant, τ_C (days)	106	106
Young's modulus of concrete, E (N/mm ²)	32000	30610
Poisson's ratio, ν	0.12	0.12
Density of concrete, ρ (kg/m ³)	1520	2162
Permeability of concrete, κ_C (m ²)	1×10^{-7}	1×10^{-6}
Material properties for fluid		
Viscosity of fluid, μ_f at 20°C (Pa.s)	8.9×10^{-4}	
Density of fluid, ρ (kg/m ³)	1000	
Linear coefficient of thermal expansion, α_T at 20°C (/°C)	12×10^{-6}	
Volumetric coefficient of thermal expansion, β_T at 20°C (/°C)	207×10^{-6}	

Table 7.2: Material properties for heterogeneous concrete prisms (material properties were assumed)

7.4.2 Theories and Assumptions

Since the model is relatively small, the heat and moisture diffusion lengths, which are calculated from Equations (4.59) and (4.63) are found to be constant throughout the prism. Therefore the initial latency and characteristic time constants, τ_L and τ_C throughout the prism can be taken as constant. The effect of ASR chemical reaction is implemented by using the asymptotic ASR expansion, ε_∞ which is determined from inverse analysis from FIB experimental results and taken at an average of 0.22. More on this theory is outlined in Chapter Four. The values for the modulus of elasticity, E and Poisson's ratio, ν are estimated from experimental results. Other properties were assumed accordingly. This research considers exposure of the prism to water only and no other deicing solution.

As a means of studying the orientation of damage in the matrix and aggregates until fully damaged, the Newton-Raphson iterative method was used. Using this method, the difference between externally applied nodal point loads vector, \mathbf{F}_{n+1} and the internal node point loads that corresponds to element stresses, \mathbf{R}^i at iteration step i must equal to zero as shown in Equation (2.69). More on the Newton-Raphson iteration is explained in Chapter Two. More theories and assumptions made in solving the simulation models in this chapter follow the explanation given in Section 6.2.2.

7.4.3 Simulation of Experimental Results from the FIB

Due to the small prism dimensions with symmetrical results in both the x_1 and x_2 directions, only the x_2 results are discussed in this section. Figure 7.10 shows the vertical stress distributions of the mesoscale models for heterogeneous materials for selective dates within one cycle in the climate chamber. Figures (a) and (b) show the vertical stress distributions for thermal fluctuations of 60°C and 5°C imposed to promote initial cracking, (c) shows the vertical stress distribution after 4 days of drying at 60°C and <10% relative humidity, (d) shows the vertical stress distribution for measurement condition where the temperature in the chamber is lowered to 20°C, (e) shows the vertical stress distribution at 18 days after fogging at 45°C and 100% relative humidity, (f) and (g) show the vertical stress distributions for freezing and thawing conditions at temperatures ranging from -20°C to 20°C.

The simulation found that the prisms are subjected to both tensile and compressive strains at different regions throughout the prisms depending on the thermal and moisture conditions in the climate chamber. For example, Figures (a) and (b) show that the prism is subjected to rapid thermal fluctuations ranging from 65°C to 5°C within a short duration. Under high temperature in (a), the prism shows tensile stresses throughout almost the entire prism with the highest values at the prism surfaces due to the immediate exposure to the extreme conditions.

The cementitious matrix portrays a lower tensile stress with localized regions of compressive stress, probably a response to the high tensile stress portrayed by the aggregates compressing the matrix that has lower strength. Overall, the prism expands outwards. In (b) where the temperature drops to 5°C, the prism shrinks, causing compressive stresses along the external surfaces. The tensile stress within the prism reduces.

When the prism is subjected to 4 days of drying at 60°C at <10% relative humidity as in (c), the prism expands similarly to (a), but with higher tensile and compressive stresses since the time constraint is longer. Then in (d) where the temperature is reduced to 20°C and the prism elongation is measured, the prism shrinks slightly due to the temperature decrease, causing compressive stresses.

In (e) where the temperature is increased to 45°C and the relative humidity is set to 100% for fogging conditions, after 14 days, the prism once again expands outwards similar to the drying conditions in (c), but with slightly higher stress values. Eventhough (c) has a higher temperature than in (e), the relative humidity which also plays a major role is ASR is higher in (e), subjecting (e) to slightly higher stress values than in (c).

Freezing and thawing in (f) and (g) also exposes the prism to rapid thermal changes ranging from -20°C to 20°C. In (f) where the temperature drops to -20°C, the expansion decreases but still shows tensile stresses at the outer regions due to the rapidity of the thermal fluctuation. The highest tensile and compressive stresses are found in the mid-region of the prism, where while rapid fluctuations of temperature cause the outer regions to have a more transient effect, the internal regions behave more constant. In (g) where temperature increases to 20°C, the stresses also increase.

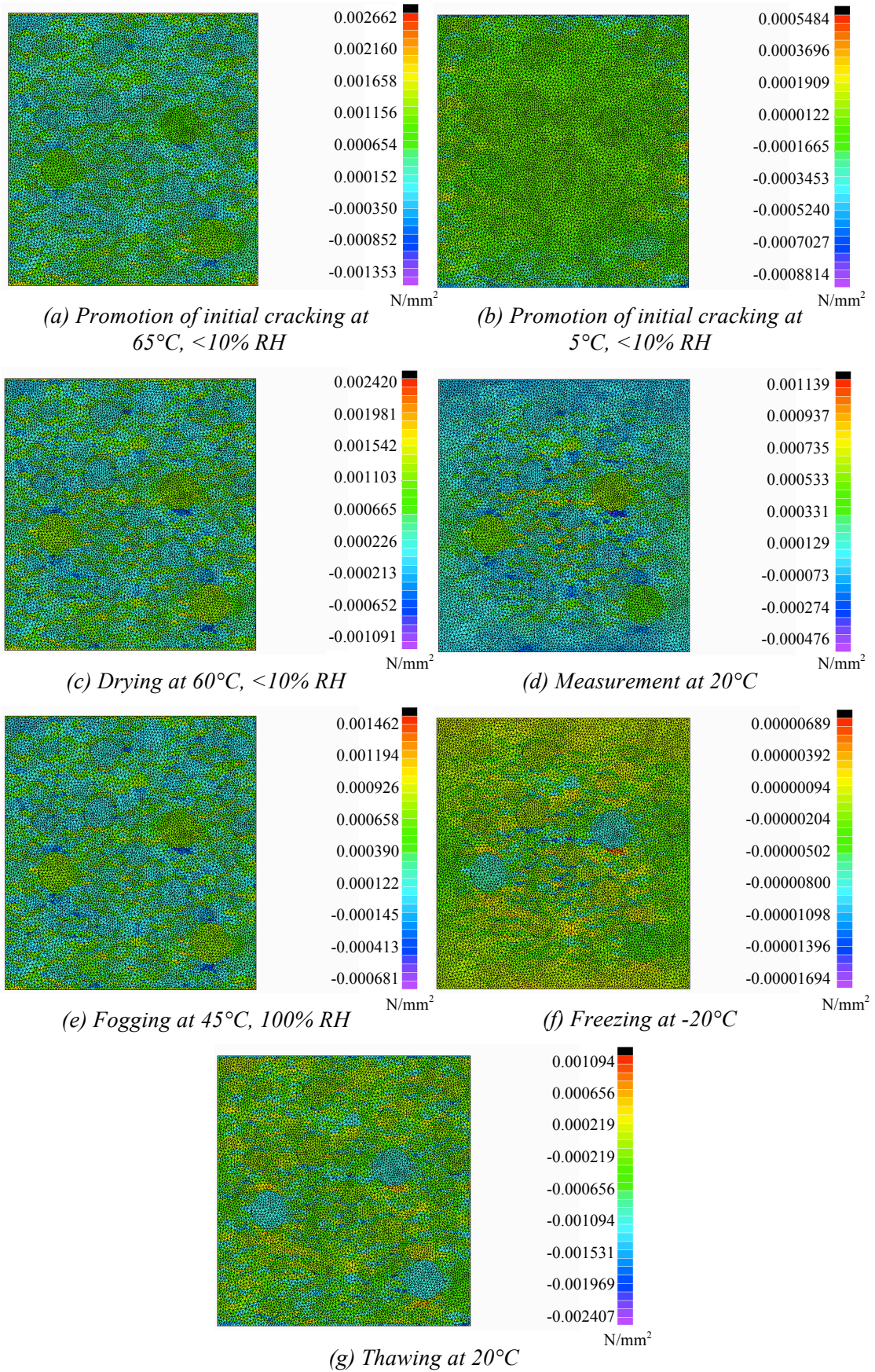


Figure 7.10: Vertical stress distributions due to ASR and thermal strains of heterogeneous concrete prism for different temperature and relative humidity conditions

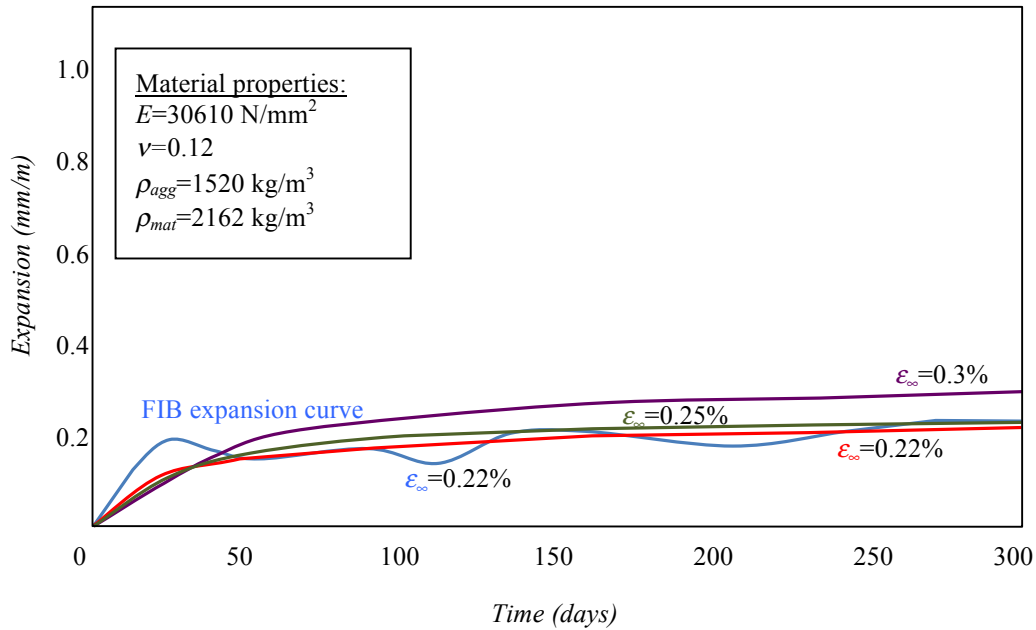


Figure 7.11: Results of ASR expansion (mm/m) over time (days) for concrete prism for different values of asymptotic volumetric strains, ϵ_{∞} from FIB experiment compared to numerical simulation

Figure 7.11 compares FIB results for the ASR expansion for concrete prism with results from numerical simulation. While experimental results yield a more fluctuating expansion curve, the numerical simulation results in a smoother curve. Testing with numerous material properties revealed that the ASR expansion model largely depends on how well one can simulate the environmental conditions and many other variables that are almost impossible to replicate explicitly. However, from this simulation it was found that the height of the expansion depends largely on the asymptotic volumetric strain, ϵ_{∞} , which is obtained from inverse analysis or can be assumed according to Larive (1998) to be within the range of $0.1 \pm 0.04\%$ to $0.4 \pm 0.15\%$.

7.4.4 Simulation of Damage due to ASR Expansion

Chapters Six and Seven show the effects of temperature, ASR and pressure loading cases on concrete as isolated and combined cases. It can be seen that individually, each case provides its own effect onto the structure and alkali-silica reactivity. To see the effect of damage in a concrete structure due to ASR expansion explicitly, a mesoscale model with heterogeneous material properties similar to Section 7.4.1 is selected (refer to Figure 7.9) and tested for different relative humidity ranging from 60%, 80% to 100% for an isothermal case of 45°C. The same assumptions are made as in Section 7.4.2.

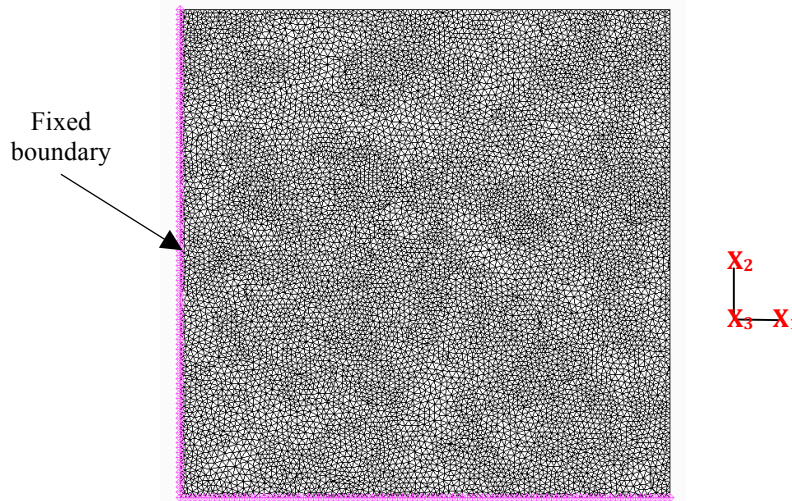


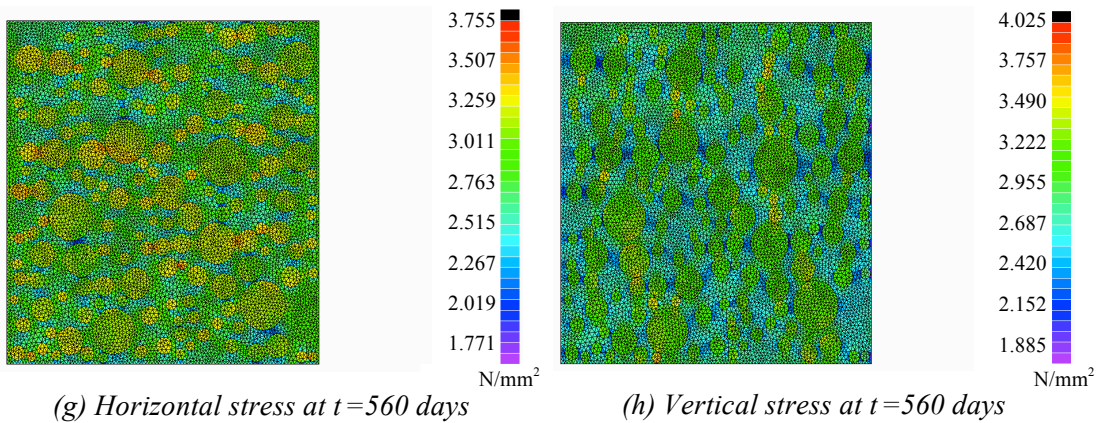
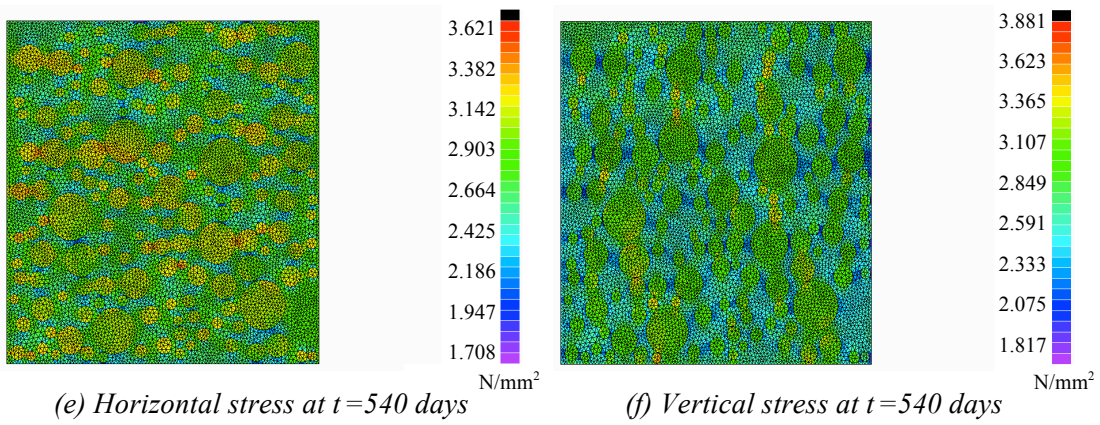
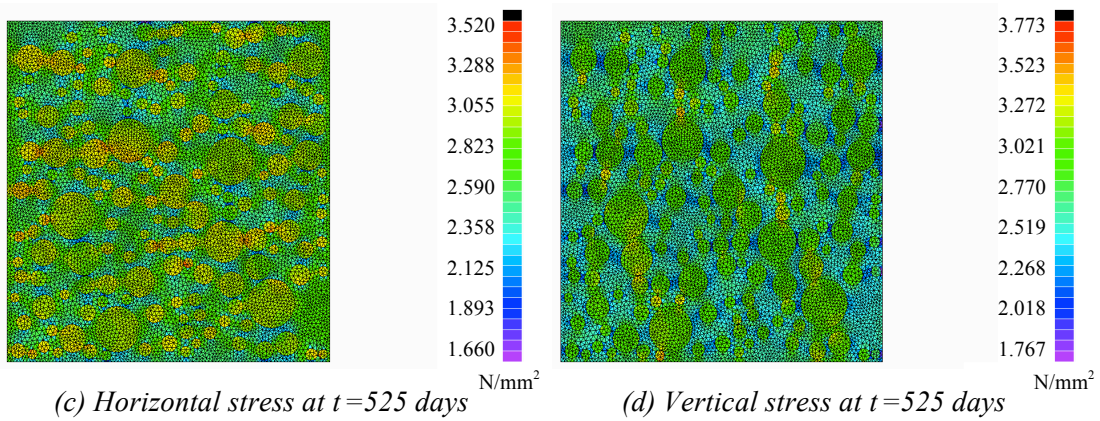
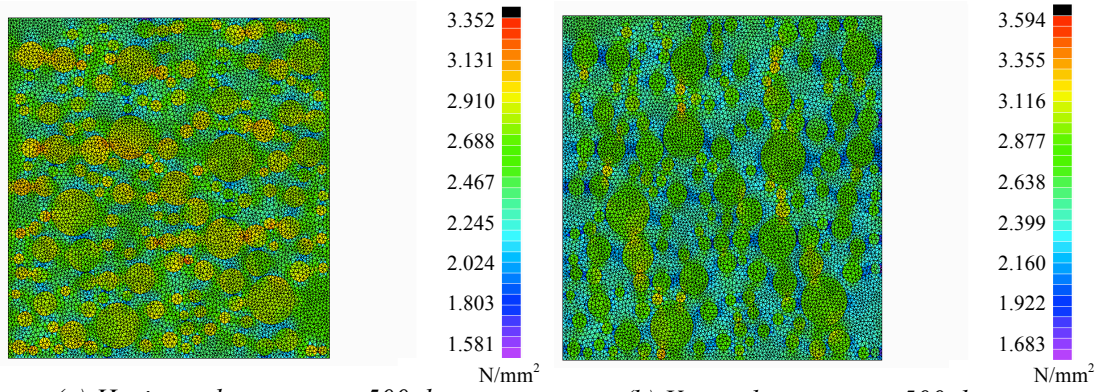
Figure 7.12: Boundary conditions for the two-dimensional three-noded plane elements mesoscale model of a 100 mm x 100 mm concrete prism

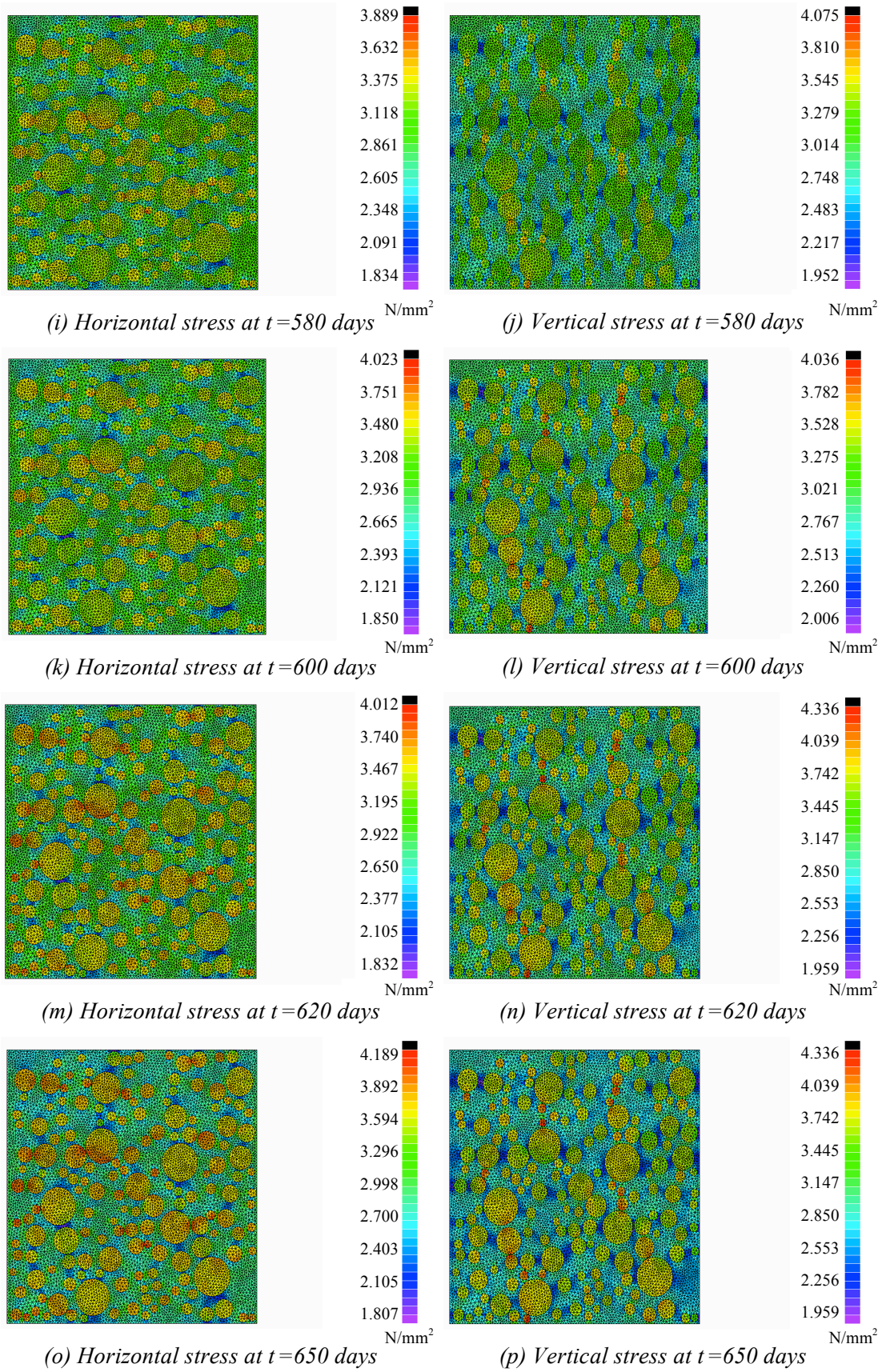
The model is restraint in the x_2 direction along the lower boundary and x_1 direction along the left boundary and in both directions at the lower left corner node. Due to the small dimensions of the mesoscopic models, the relative humidity and temperature are taken as constant throughout the cross-section as well as the initial latency and characteristic time constants. The purpose of the mesoscale models having different relative humidity values of 60%, 80% or 100% in this section is to determine damage intensities under such circumstances.

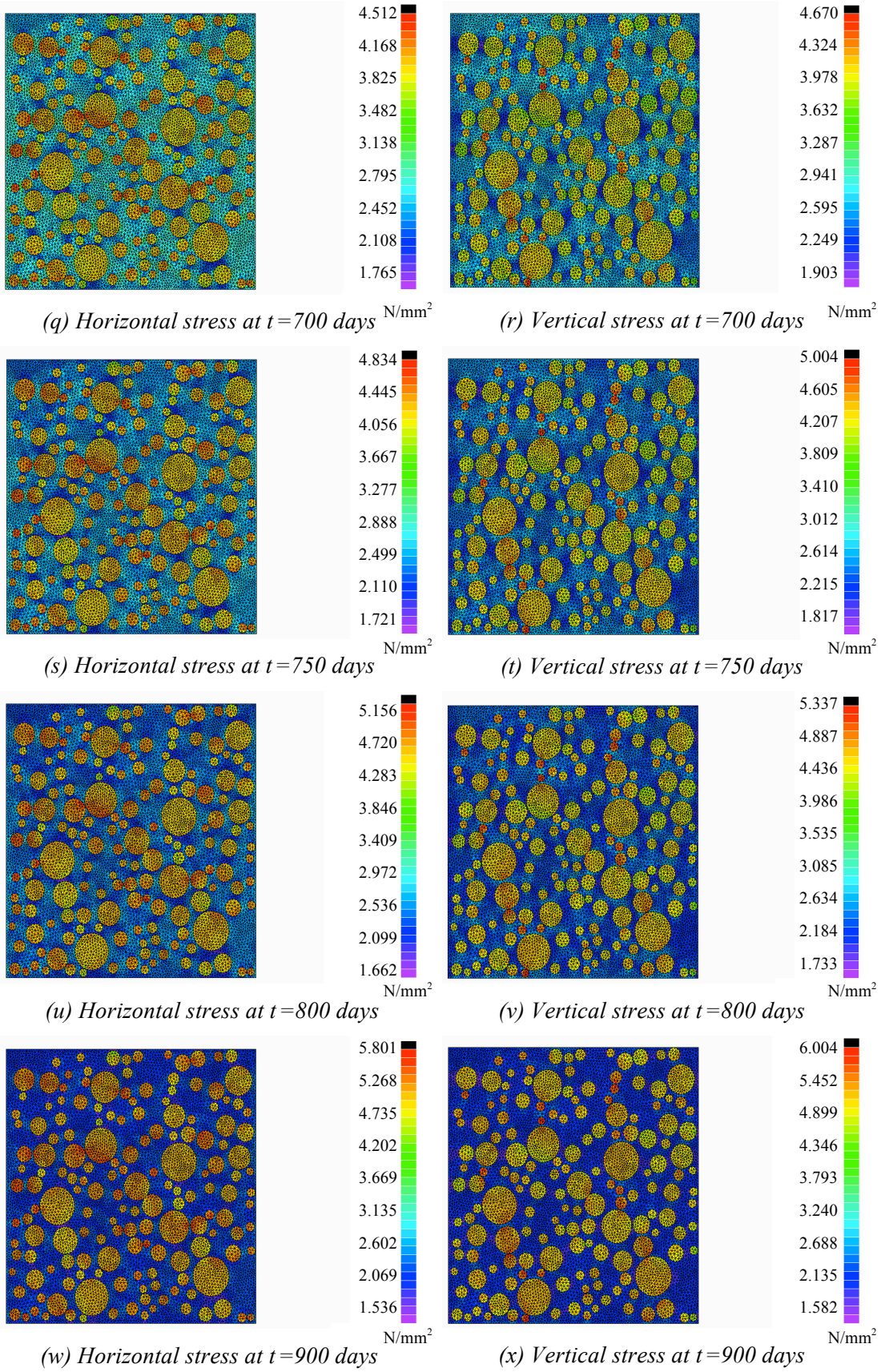
Material properties	Aggregate	Mortar
Tensile strength, f_t (N/mm ²)	6.0	3.0
Compressive strength, f_c (N/mm ²)	30.0	30.0
Fracture energy, G (Nmm/mm ²)	0.011	0.009
Nonlocal radius, R (mm)	5	5
Density of concrete, ρ (kg/m ³)	1520	2162
Porosity of concrete, ϕ (%)	15	15
Permeability of concrete, κ_C (m ²)	1×10^{-7}	1×10^{-6}
ASR material properties	Aggregate	Mortar
Asymptotic ASR expansion, ϵ_∞ (%)	0.22	0.22
Poisson's ratio, ν	0.12	0.12
Initial latency time constant, $\tau_l(T_0)$ (days)	106	106
Initial characteristic time constant, $\tau_C(T_0)$ (days)	25	25
Initial temperature of concrete, T_0 (K)	1×10^{-7}	1×10^{-6}
Young's modulus of concrete, E (N/mm ²)	50000	35000
Heat material properties	Aggregate	Mortar
Thermal conductivity of concrete, k (W/mK)	1.77	1.77
Specific heat capacity of concrete, C_v (J/gK)	790	730
Density of fluid, ρ_f (kg/m ³)	1000	1000
Viscosity of fluid, μ_f at 20°C (Pa.s)	8.9×10^{-4}	8.9×10^{-4}
Linear coefficient of thermal expansion, α_T at 20°C (/°C)	12×10^{-6}	12×10^{-6}
Volumetric coefficient of thermal expansion, β_T at 20°C (/°C)	207×10^{-6}	207×10^{-6}

Table 7.2: Material properties for heterogeneous concrete prisms
(material properties were assumed)

Figure 7.13 shows the stress distributions for the mesoscale model with 80% relative humidity for the respective time steps. Figures start with depicting tensile stresses throughout the model, with the highest tensile stresses in the aggregates. As time increases, so do the tensile stresses in both the horizontal and vertical directions. Once the damage initiates at 525 days (see Figure 7.14 (b)), stresses in the damaged regions start to reduce due to the stress release from cracking. Meanwhile, stresses in undamaged regions continue to increase. From here, it can be seen that stress distributions increase linearly in the initial stage, after some point, the stress becomes constant and then decreases when damage initiates.







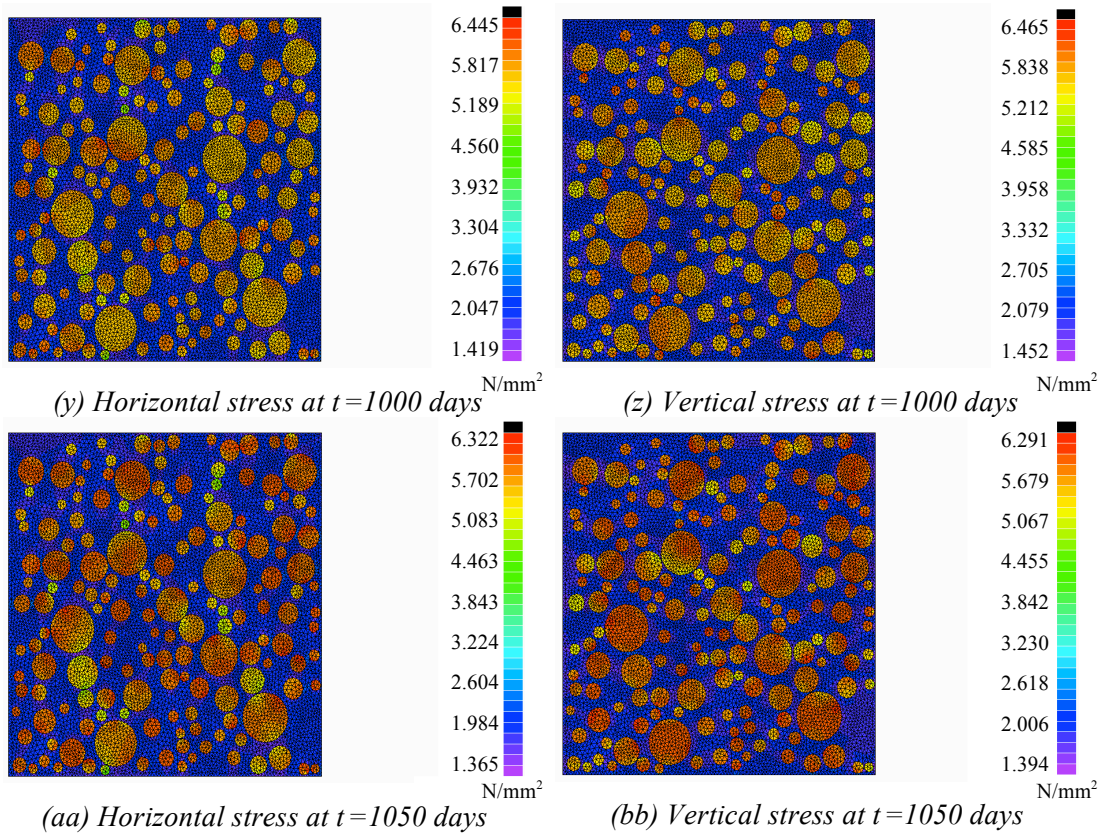
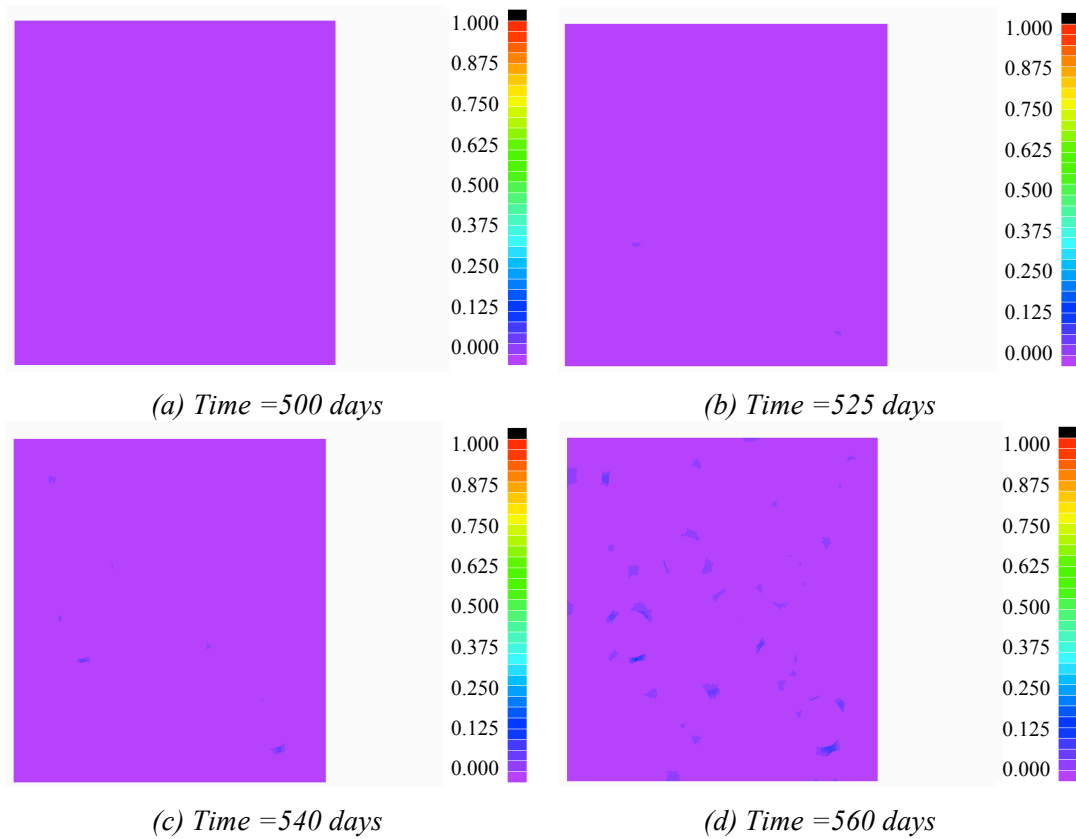
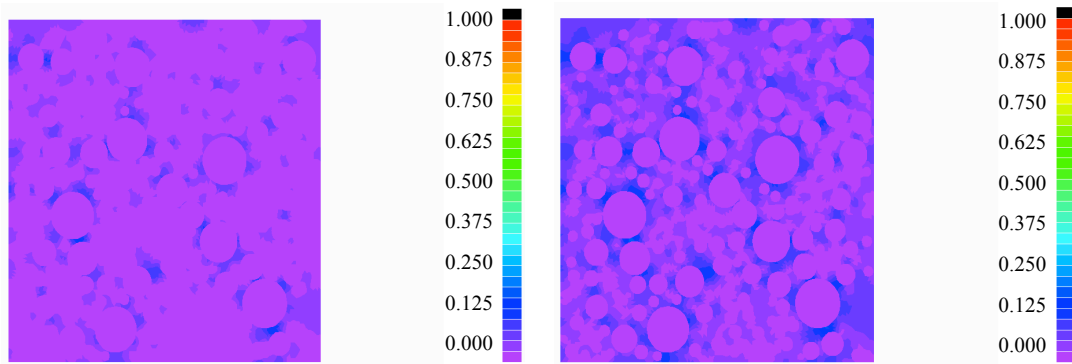


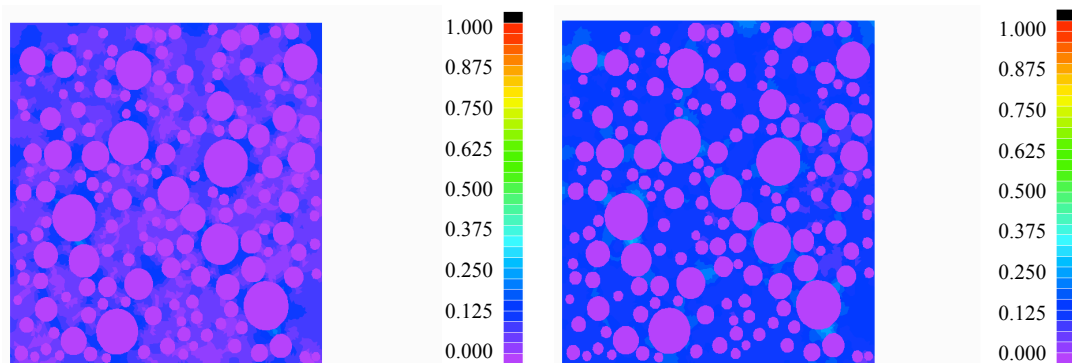
Figure 7.13: Horizontal and vertical stress distributions due to ASR expansion for an isothermal condition of 45°C and relative humidity of 80% for a mesoscale model





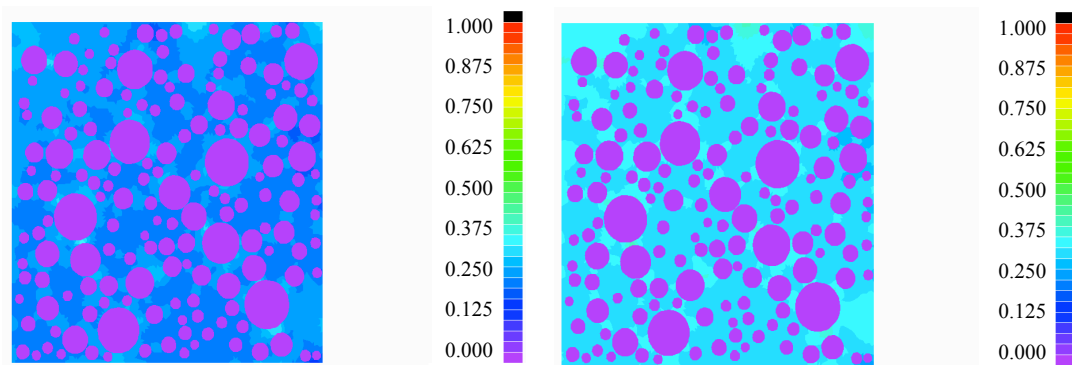
(e) Time = 580 days

(f) Time = 600 days



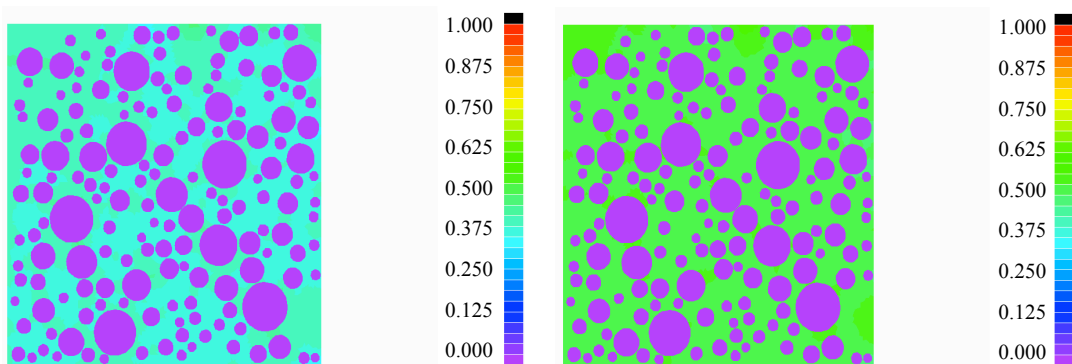
(g) Time = 620 days

(h) Time = 650 days



(i) Time = 700 days

(j) Time = 750 days



(k) Time = 800 days

(l) Time = 900 days

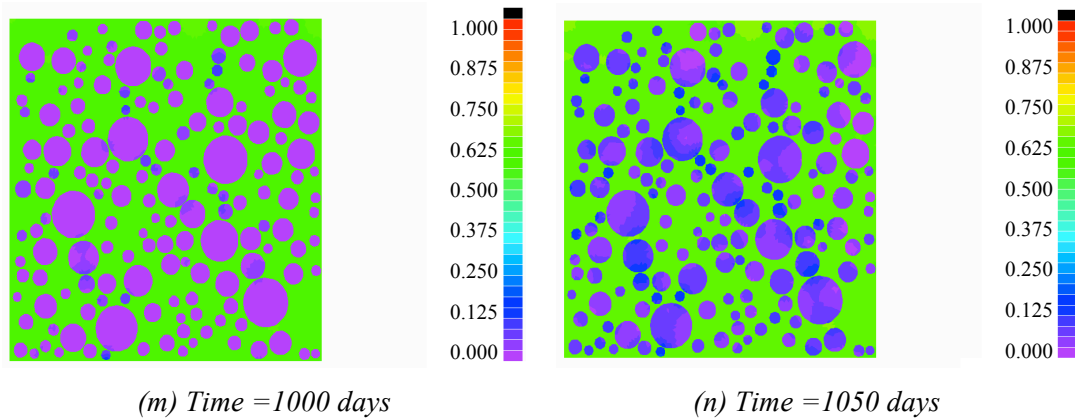


Figure 7.14: Damage due to ASR expansion for an isothermal condition of 45°C and relative humidity of 80% for a mesoscale model with heterogeneous material properties

Figures 7.14 to 7.16 show the damage distributions for 80%, 100% and 60% relative humidity for the mesoscale model. It can be seen that although models with different relative humidity values have similar damage patterns, the time scale is longer for the lower relative humidity. Damage initiates at approximately 70 days for 100% relative humidity and 400 days for 80% relative humidity. For 60% relative humidity, which is the minimum condition for relative humidity required for ASR to initiate, it can be concluded that damage due to ASR expansion did not happen.

Damage initiation occurs at the interfacial zones in between matrix and aggregates due to ASR expansion and spreads throughout the whole matrix, which has lower stiffness than the aggregates. Since aggregates have larger stiffness values than the matrix, eventhough with a higher stress in the aggregates, the lower tensile strength, f_t value for the cementitious matrix causes the damage to initiate in the matrix. Damage in the aggregates initiates at a later time, after the tensile strength, f_t value for aggregates have been surpassed, which are approximately 1000 days for the 80% and 100% relative humidity, and no damage was seen in the aggregates with the 60% relative humidity.

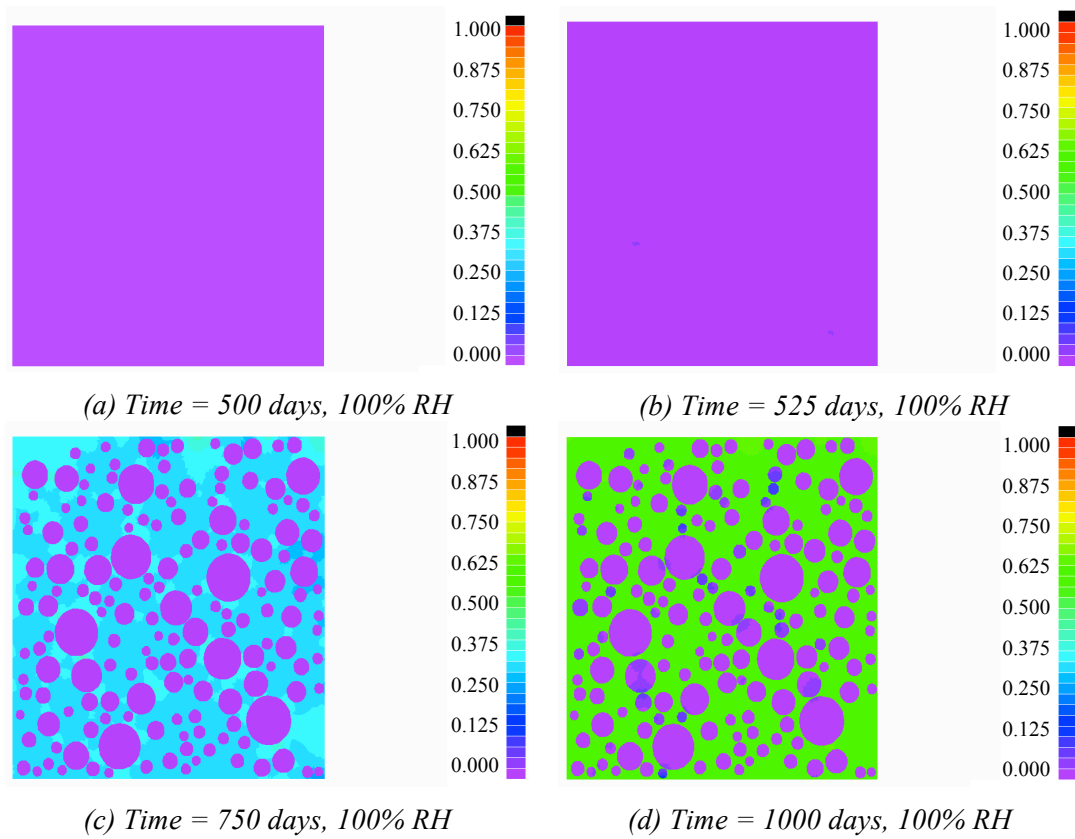


Figure 7.15: Damage due to ASR expansion for an isothermal condition of 45°C and relative humidity of 100% for a mesoscale model with heterogeneous material properties

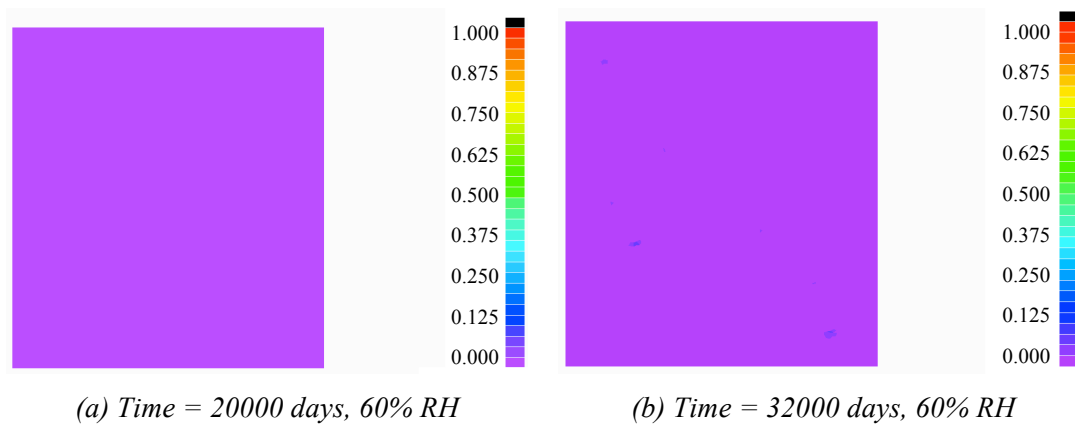


Figure 7.16: Damage due to ASR expansion for an isothermal condition of 45°C and relative humidity of 60% for a mesoscale model with heterogeneous material properties

8 CONCLUSION

8.1 SUMMARY

The aim of this research is to determine the effects of temperature, relative humidity and mechanical loading on ASR expansivity in a concrete structure. This was performed at two levels, the mesoscale level in order to determine damage mechanism at a more intricate level allowing us to determine damage initiation and orientation, and at the macroscale level which shows the accumulative damage effects at the structural level in a smeared sense.

The engineering study of a macroscale concrete gravity dam incorporated with the effects of temperature, relative humidity and mechanical loading cases as isolated and combined cases in this thesis shows that individually, temperature, relative humidity and mechanical loading influence ASR expansivity and causes its own affects to the expansion or contraction of the structure.

ASR has an increased effect due to moisture content. A higher relative humidity increases the characteristic and latency time constants, which means that a shorter time is needed before damage initiates. As a benchmark unanimous among fellow researchers, a minimum of 60% relative humidity was required for ASR deformation to occur. Under varying relative humidity conditions of 60% to 100%, it was discovered that ASR expands rapidly with a higher stress distribution at 100% relative humidity as opposed to a relative humidity of 60%. Under isothermal conditions, damage due to ASR expansion seems smeared.

Temperature distribution behaves linearly, moving from higher temperature to lower temperature regions until a steady state solution is reached. The length of time needed to reach equilibrium depends mainly on the material properties of the concrete.

Thermal difference, being a positive or negative value, leads to tensile or compressive stresses in concrete. The stress value increases rapidly in the initial stage, after which it becomes constant. Temperature, as well as relative humidity influences the latency and characteristic time constants, which dictate the rapidity of ASR expansion showing its dependency on the heat and moisture diffusion lengths into the structure, rendering heterogeneous values across the cross-section of the structure according to the relative humidity and temperature distribution. Hence, a mesoscopic study should be applied for further evaluation of ASR effects on a concrete structure.

Hydrostatic pressure causes compressive stresses in a structure. However, depending on the concrete material properties, boundary conditions and environmental conditions, its effect could be rapidly overcome due to expansion of the structure from ASR and thermal expansion. The shape of the structure as well as its restraints also influences the deflection of the structure. The tensile stresses in the structure due to thermal difference and ASR deformation causes the dam to expand towards the region with lower thermal difference and ASR deformation.

The mesoscale model in this thesis was developed to have heterogeneous material properties for aggregates and the cementitious matrix. In order to study the sole effect of ASR chemoelasticity, any mechanical loading has been omitted. It has been found that damage initiates at the interfacial transition zones between the aggregates and the matrix and spreads within the matrix which has lower stiffness. Damage in the aggregates, which have higher stiffness and tensile strength, occurs at a much later time than for the cementitious matrix which has a lower tensile strength.

The determination of ASR expansion with inverse analysis from experimental results and application into modeling shows that ASR expansion can be replicated in numerical simulation, provided with the proper material properties and environmental parameters. Therefore it can be concluded that the intensity of damage in a concrete structure due to ASR expansion, be it on the mesoscale or macroscale, depends on a lot of factors, most importantly the temperature and relative humidity. Other external factors that play an influence on the damage orientation and structure deflection depend on material properties, boundary conditions and if applicable, external loading.

8.2 FUTURE WORK

Although this thesis achieved its aim of determining the effects of thermo-chemo-mechanics on ASR expansion, there is always room for improvement. Since much of the material properties used in the thesis were assumed due to unavailability of infield data, detailed material data could perhaps refine the numerical simulation outcome. Another factor that can be improved is the porosity of the mesoscale model. Fluid transfer in porous media requires explicit pore simulation. Without pore simulation, transfer of fluid is smeared, hence only the moisture diffusion length is adequate for modeling purposes. Another interesting factor to consider in simulation is to model the effects of deicing solution in ASR expansion.

BIBLIOGRAPHY

- Ahmed T. (2003). The Effect of Alkali-Reactivity on the Mechanical Properties of Concrete. *Construction and Building Materials*, **17**:123-144.
- Aliabadi M.H. (2001). *Nonlinear Fracture & Damage Mechanics*. WIT Press. Southampton, UK.
- ASTM Designation ASTM C-1260. (1994). *ASTM C1260-05 Standard Test Method for Potential Alkali Reactivity of Aggregates (Mortar-Bar Method)*. Annual Book of ASTM Standards Volume 04.02.
- ASTM Designation ASTM C-295-08. (1994). *Standard Guide for Petrographic Examination of Aggregates for Concrete*. Annual Book of ASTM Standards Volume 04.02.
- Badia S. & Codina R. (2008). Pressure Segregation Methods Based on a Discrete Pressure Poisson Equation. An Algebraic Approach. *International Journal for Numerical Methods in Fluids*, **56**:351-382. Wiley InterScience.
- Bangert F., Kuhl D. & Meschke G. (2003). Modelling of Concrete Deterioration by Alkali-Silica Reaction. *Computational Modelling of Concrete Structures*, **EURO-C**:361-372.
- Bangert F., Kuhl D. & Meschke G. (2001). Finite Element Simulation of Chemo-Mechanical Damage Under Cyclic Loading Conditions. *Fourth International Conference on fracture Mechanics of Concrete and Concrete Structures*, FRAMCOS IV, 207-214.
- Bangert F., Kuhl D. & Meschke G. (2004). Chemo-Hygro-Mechanical Modelling and Numerical Simulation of Concrete Deterioration Caused by Alkali-Silica Reaction. *International Journal for Numerical and Analytical Methods in Geomechanics*, **28**:68-714. John Wiley & Sons Ltd.
- Bangert F. & Meschke G. (2004). A Coupled Hygro-Chemo-Mechanical Damage Model for ASR-Affected Concrete. *Fracture Mechanics of Concrete Structures*, FRAMCOS V, Vol. 1, pp 523-530.
- Bathe Klaus-Jürgen. (1996). *Finite Element Procedures*. Prentice-Hall, Inc. New Jersey, USA.

- Bazant Z.P. & Steffens A. (2000). Mathematical Model for Kinetics of Alkali-Silica Reaction in Concrete. *Cement and Concrete Research*. **30**:419-428. Elsevier Science Inc.
- Bazant Z.P., Tabbara M.R., Kazemi M.T. & Pijaudier-Cabot G. (1990). Random Particle Model for Fracture of Aggregate or Fibre Composites. *Journal of Engineering Mechanics* 116 (8). pp. 1686-1705.
- Bazant Z.P. & Kezemi M.T. (1988). Brittleness and Size Effect in Concrete Structures. Engineering Foundation Conference on "Advances in Cement Manufacture and Use", Paper No. 5, pp.5.1-5.8.
- Bazant Z.P. (1987). Nonlocal Damage Theory. *Journal of Engineering Mechanics* 113 (10). pp. 1512-1533.
- Capra B. & Bournazel J.-P. (1998). Modeling of Induced Mechanical Effects of Alkali-Aggregate Reactions. *Cement and Concrete Research*, Vol. 28, No. 2, pp. 251-260. Elsevier Science Ltd. USA.
- Capra B. & Sellier A. (2000). Anisotropic Modelling of Alkali-Aggregate Reaction in Concrete. *11th International Conference on Alkali-Aggregate Reaction*. Québec.
- Carrazedo R. & de Lacerda L.A. (2004). A Parametric Model Discussion for the Concrete Expansion due to AAR. *Proceedings of the 12th International Conference on Alkali-Aggregate Reaction in Concrete*.
- Charlwood R.G., Steele R.R., Solymar Z.V. & Curtis D.D. (1992). *Int. Conf. on AAR in Hydroelectric Plants and Dams*. CEA&CANCOLD. Fredericton. New Brunswick, Canada.
- Chatterji, S. (1978). An Accelerated Method for the Detection of Alkali-Aggregate Reactivities of Aggregates. *Cement & Concrete Research*. **8**: 647-650.
- Chen, W.-F. (1994). *Constitutive Equations for Engineering Materials. Volume 2: Plasticity and Modeling*. Elsevier Science B.V. The Netherlands.
- Chengzi Z., Aiqin W., Zhaojia W., Ningsheng Z. & Mingshu T. (2004). The Micromechanical Analysis of the Expansion and Cracking Model due to Alkali Aggregate Reaction. *Proceedings of the 12th International Conference on Alkali-Aggregate Reaction in Concrete*.
- Comi C., Fedele R. & Perego U. (2009). A Chemo-Thermo-Damage Model for the Analysis of Concrete Dams Affected by Alkali-Silica Reaction. *Mechanics of Materials*, **41**:210-230. Elsevier Ltd.
- Cook R. D. (1995). *Finite Element Modeling for Stress Analysis*. John Wiley & Sons, Inc. USA.
- Coussy O. (2004). *Poromechanics*. John Wiley & Sons Ltd. England.
- Cordebois J. & Sidoroff F. (1982). Endommagement Anisotrope. *J. Mécanique Théorétique et Appliquée*, Special.
- Danay A., Adeghe L. & Hindy, A. (1993). Diagnosis of the Cause of the Progressive Concrete Deformations at Saunders Dam. *Concrete International*. September 1993. pp. 25-33.

-
- Dent-Glasser L.S. & Kataoka N. (1981). The Chemistry of Alkali-Aggregate Reactions. *Proceedings of the Fifth International Conference on Alkali-Aggregate Reactions*, S 252/23, pp. 66.
- Dent-Glasser L.S. & Kataoka N. (1993). The Chemistry of Alkali-Aggregate Reaction. *Cement and Concrete Research*, **23**: 93-103.
- Diamond S., Barneyback Jr. R.S. & Struble L.J. (1981). On the Physics and Chemistry of Alkali-Silica Reactions. *Proceedings of the Fifth Conference on Alkali-Aggregate Reaction in Concrete*, S252/22, pp. 1-11.
- Dron R. & Brivot F. (1981). Thermodynamic and Kinetic Approach to the Alkali-Silica Reaction. Part 2: Experiment. *Cement and Concrete Research*, **11**: 1-9.
- Dunant C.F. & Scrivener K.L. (2010). Micro-mechanical Modelling of Alkali-Silica-Reaction-Induced Degradation using the AMIE Framework. *Cement and Concrete Research*, **40**:517-525.
- Eckardt S. (2009). *Adaptive Heterogeneous Multiscale Models for the Nonlinear Simulation of Concrete*. Ph. D Thesis. Bauhaus-Universität Weimar.
- Ehlers W. (2002). *Foundations of Multiphasic and Porous Materials*. In: *Porous Media – Theory, Experiments and Numerical Applications*. W. Ehlers, J. Bluhm (eds), Springer, Berlin pp. 3-86.
- Fairbairn E.M.R., Riberio F.L., Toledo-Filho R.D., Lopes L.E., Silvosso M.M., Águas M.F.F. & Guedes Q.M. (2004). Smearred Cracking FEM Simulation of Alkali Silica Expansion using a New Macroscopic Coupled Model. *Proceedings of the 12th International Conference on Alkali-Aggregate Reaction in Concrete*.
- Farage M.C.R., Alves J.L.D. & Fairbairn E.M.R. (2004). Macroscopic Model of Concrete Subjected to Alkali-Aggregate Reaction. *Cement and Concrete Research*, **34**:495-505. Pergamon.
- Flórez-López J., Benallal A., Gaymonat G. & Billardon R.A. (1994). A Two-field Finite Element Formulation for Elasticity Coupled to Damage. *Computer Methods in Applied Mechanics and Engineering*. **114**:3-4.
- Fuller W.B. & Thompson S.E. (1907). The Laws of Proportioning Concrete. *Transactions of the ACSE*. Volume 159.
- Garcia-Diaz E., Riche J., Bulteel D. & Vernet C. (2005). Mechanism of Damage for the Alkali-Silica Reaction. *Cement and Concrete Research*.
- Garcia-Diaz E., Riche J. & Bulteel D. (2004). Damage Mechanism for a Flint Aggregate Submitted to Alkali-Silica Reaction. *Proceedings of the 12th International Conference on Alkali-Aggregate Reaction in Concrete*. pp. 99-103.
- Gartling D.K. & Hogan R.E. (1994). *COYOTE - A Finite Element Computer Program for Nonlinear Heat Conduction Problems. Part I - Theoretical Background*. SAND94-1173.
- Gawin D. Pesavento F. & Schrefler B.A. (2003). Modelling of Hygro-Thermal Behaviour of Concrete at High Temperature with Thermo-Chemical and Mechanical Material Degradation. *Computer Methods in Applied Mechanics and Engineering*, **192**:1731-1771. Elsevier Science B. V.
-

- Grattan-Bellew P.E., Cybanski G., Fournier B. & Mitchell L. (2003). Proposed universal accelerated test for alkali-aggregate reaction the concrete microbar test. NRCC-46876, *Cement Concrete and Aggregates*, Vol. 25, no. 2, pp. 29-34.
- Grattan-Bellew P.E., Du-you L., Fournier B. & Mitchell L. (2004). Comparison of expansions in the concrete prism and concrete microbar tests of an assorted suite of aggregates from several countries. NRCC-47359, *Proceedings of the 12th International Conference on Alkali-Aggregate Reaction in Concrete*, Beijing, China, Oct. 15-19, pp. 251-256.
- Grill A. & Sorimachi K. (1979). The Thermal Loads in the Finite Element Analysis of Elasto-Plastic Stresses. *International Journal for Numerical Methods in Engineering*, **14**:499-505. John Wiley & Sons Ltd.
- Grimal E., Sellier A., Multon S., Le Pape Y. & Bourdarot E. *Concrete Modelling for Expertise of Structure Affected by Alkali Aggregate Reaction*. France.
- Guermond J.L. & Quartapelle L. (1998). On Stability and Convergence of Projection Methods Based on Pressure Poisson Equation. *International Journal for Numerical Methods in Fluids*. **26**: 1039-1053. John Wiley & Sons, Ltd.
- Guidoum A. & Navi P. (1993). Numerical Simulation of Thermomechanical Behaviour in Concrete through a 3D Granular Cohesive Model. *Micromechanics of Concrete and Cementitious Composites*. Presses Polytechniques et Universitaires Romandes. Lausanne. pp. 213-228.
- Häfner S. (2007). *Grid-based Procedures for the Mechanical Analysis of Heterogeneous Solids*. Ph. D thesis. Bauhaus-Universität Weimar.
- Häfner S., Eckardt S., Luther T. & Könke C. (2006). *Mesoscale Modeling of Concrete: Geometry and Numerics*. Computers and Structures 84. pp. 450-461. Elsevier Ltd.
- Halcrow J. *Implementation of a Pressure Poisson Equation Method for Plane Couette Flow*. Georgia Institute of Technology.
- Hobbs. D.W. (1988). *Alkali-Silica Reaction in Concrete*. American Society of Civil Engineers.
- Huang M. & Pietrusczak S. (1999). Modeling of Thermomechanical Effects of Alkali-Silica Reaction. *Journal of Engineering Mechanics*. pp. 476-485.
- Janssen, H. (2004). *Simulation of Moisture and Heat Transfer in Building Components under Atmospheric Excitation: Conservative Modelling and Numerical Optimization*. Building Physics Group. Technical University Eindhoven. The Netherlands.
- Kachanov L.M. (1986). *Introduction to Continuum Damage Mechanics*. Martinus Nijhoff Publishers. Dordrecht, the Netherlands.
- Kagimoto H. (2004). Threshold OH⁻ Ion Concentration in Pore Solution of Mortar using Alkali Reactive Aggregates. *Proceedings of the 12th International Conference on Alkali-Aggregate Reaction in Concrete*.
- Kawamura M. & Iwahori K. (2004). Some Theoretical Considerations on Expansive Pressure of ASR Gel. *Proceedings of the 12th International Conference on Alkali-Aggregate Reaction in Concrete*.

-
- Kuhl D., Bangert F. & Meschke G. (2003). Coupled Chemo-Mechanical Deterioration of cementitious Materials. Part I: Modeling. *International Journal of Solids and Structures*, **41**:15-40. Elsevier Ltd.
- Kythe P. K. & Wei D. (2004). *An Introduction to Linear and Nonlinear Finite Element Analysis. A Computational Approach*. Birkhäuser. Boston.
- Lahmer, T., *Optimal Experimental Design for Nonlinear Ill-Posed Problems Applied to Gravity Dams*.
- Larive C., Laplaud A. & Coussy O. (2000). The Role of Water in Alkali-Silica Reaction. *11th International Conference on Alkali-Aggregate Reaction*. Québec.
- Larive C. (1998). *Apports Combinés de l'expérimentation et de la Modélisation à la Compréhension de l'alcali-réaction et de ses effets Mécaniques*. Ph.D thesis. Laboratoire Central des Ponts et Chaussées. Paris.
- Leger P., Cote P. & Tinawi R. (1996). Finite Element Analysis of Concrete Swelling due to Alkali-Aggregate Reactions in Dams. *Computers & Structures*, **60**(4), pp 601-611.
- Leite J.P.B., Slowik V. & Apel J. (2004). Computer Simulation of Fracture Processes of Concrete using Mesolevel Models of Lattice Structures. *Cement and Concrete Research* **34**. pp. 1025-1033. Elsevier Ltd.
- Leite J.P.B., Slowik V. & Apel J. (2007). Computational Model of Mesoscopic Structure of Concrete for Simulation of Fracture Processes. *Computer and Structures* **85**. pp. 1293-1303. Civil-Comp Ltd. and Elsevier Ltd.
- Lemaitre J. (1971). Evaluation of Dissipation and Damage in Metals. *Proceedings I.C.M.* Vol. 1. Kyoto, Japan.
- Lemaitre J. (1985). A Continuous Damage Mechanics Model for Ductile Fracture. *Journal of Engineering Materials and Technology*, **107**, pp 83-89. January 1985.
- Lepi S. M. (1998). *Practical Guide to Finite Elements. A Solid Mechanics Approach*. Marcel Dekker, Inc. USA.
- Lewis R.W., Nithiarasu P. & Seetharamu K. N. (2004). *Fundamentals of the Finite Element Method for Heat and Fluid Flow*. John Wiley & Sons Ltd. England.
- Li K. & Coussy O. (2004). Comprehensive Chemo-Mechanical Modelling of ASR Expansion in Concrete Structures. *Proceedings of the 12th International Conference on Alkali-Aggregate Reaction in Concrete*.
- Li. K, Xu Y. & Larive C. (2004). Anisotropy of ASR Expansion: Modelling and Interpretation. *Proceedings of the 12th International Conference on Alkali-Aggregate Reaction in Concrete*.
- Li K., Ulm F.-J., Coussy O., Larive C. & Fan L. (2000). Chemoelastic Modelling of Alkali-Silica Reaction in Concrete. *11th International Conference on Alkali-Aggregate Reaction*. Québec.
- Lopes L.E. (2004). *Modelagem Mecânica e Numérica da Reação Álcali-Agregado com Aplicação a Barragens de Concerto*. Ph.D thesis. COPPE/UFRJ. November 2004. Brazil.
-

- Lund E. (2002). *Short Note on Thermal and Thermo-Elastic Finite Element Analyses*. Aalborg University.
- Mazars J. (1986). A Model of Unilateral Elastic Damageable Material and its Application to Concrete. *Proceedings of Fracture Toughness and Fracture Energy of Concrete*, ed F.H. Wittmann. pp 61-71. Elsevier. Amsterdam.
- Meyer R.E. (1971). *Introduction to Mathematical Fluid Dynamics*. Dover Publications Inc. New York.
- Mikelic A. (2003). *Boundary Conditions Between Free Fluid Flow and a Porous Medium*. Workshop on Filtration Problems in Porous Media and Paper Manufacturing (WG 14). The Netherlands.
- Mizuta M., Kojima T. & Kuzume K. *Analytical Evaluation of Effect on ASR of RC Structure using Meso-scale Concrete Element by FEM*. Japan.
- Moshtagh M. & Ghaemian M. (2008). Effect of Alkali-Aggregate Reactions in Concrete Dams Using Finite Element Method. *Scientia Iranica*, Vol. 15, No. 1, pp1-7. Sharif University of Technology.
- Mulligan G.P. (1988). On Nonlinear Temperature-Dependence of Thermal Strain. *Communications in Applied Numerical Methods*, 4:157-160. John Wiley & Sons Ltd.
- Moranville-Regourd M. (1997). Modelling of Expansion Induced by ASR – New Approaches. *Cement and Concrete Composites*, 19:415-425. Elsevier Science Ltd. Great Britain.
- Peerlings R.H.J. (1999). *Enhanced Damage Modelling for Fracture and Fatigue*. Technische Universiteit Eindhoven.
- Poole A.B. (1992). *The Alkali-Silica Reaction in Concrete*. R.N. Swamy (ed.). Blackie. London.
- Poyet S, Sellier A, Capra B., Foray G., Torrenti J.-M., Cognon H. & Bourdarot E. (2004). Modelling of Alkali-Silica Reaction in Concrete, Part 1: Influence of Aggregate Size Range on Chemical Modelling of ASR. *Proceedings of the 12th International Conference on Alkali-Aggregate Reaction in Concrete*.
- Poyet S, Sellier A, Capra B., Foray G., Torrenti J.-M., Cognon H. & Bourdarot E. (2004). Modelling of Alkali-Silica Reaction in Concrete, Part 2: Influence of Water on ASR. *Proceedings of the 12th International Conference on Alkali-Aggregate Reaction in Concrete*.
- Poyet S, Sellier A, Capra B., Foray G., Torrenti J.-M., Cognon H. & Bourdarot E. (2004). Modelling of Alkali-Silica Reaction in Concrete, Part 3: Structural Effects Induced by ASR. *Proceedings of the 12th International Conference on Alkali-Aggregate Reaction in Concrete*.
- Qi Y. & Ziyun W. (2004). Study of Expansion of A.S.R using Sol-Gel Expansion Method. *Proceedings of the 12th International Conference on Alkali-Aggregate Reaction in Concrete*.
- Reddy J.N. & Gartling D.K. (1994). *The Finite Element Method in Heat Transfer and Fluid Dynamics*. CRC Press Inc.

-
- Reddy J. N. (2006). *An Introduction to the Finite Element Method. Third Edition. International Edition 2006*. McGraw-Hill Education (Asia). Singapore.
- Saanouni K. (2003). *Numerical Modelling in Damage Mechanics*. Kogan Page Limited. Great Britain.
- Saouma V. & Perotti L. (2005). Alkali Aggregate Reactions in Dams; Stress Analysis and Long Term Predictions. *ASDSO Dam Safety Conference*. New Orleans.
- Saouma V. & Perotti L. (2006). Constitutive Model for Alkali-Aggregate Reactions. *ACI Materials Journal*, Vol. 13, No. 3.
- Schlangen E. & van Mier J.G.M. (1992). *Simple Lattice Model for Numerical Simulation of Fracture of Concrete Materials and Structures*. Material Structures 25(153). pp. 534-542.
- Seignol J.F., Barbier F., Multon S. & Toutlemonde F. (2004). Numerical Simulation of ASR Affected Beams Comparison to Experimental Data. *Proceedings of the 12th International Conference on Alkali-Aggregate Reaction in Concrete*.
- Sellier A. & Bary B. (2002). Coupled damage tensors and weakest link theory for the description of crack induced anisotropy in concrete. *Engineering Fracture Mechanics*, Vol. 69, pp. 1925-1939.
- Sellier A. & Capra B. (1997). *Physical-chemical modeling of the alkali-aggregate reaction: contribution to the calculation of degraded structure*. Revue française de genie civil. 1(3) pp. 445-481.
- Showalter R.E. (2002). *Diffusion in Deforming Porous Media*. Mathematics Subject Classification.
- Skrzypek J. & Ganczarski A. (1999). *Modeling of Material Damage and Failure of Structures*. Springer-Verlag. Germany.
- Sovinec, C. R. (2000). *Nonlinear Fusion Magneto-Hydrodynamics with Finite Elements*. International Sherwood Fusion Theory Conference. Los Angeles. California.
- Stanton T.E. (1940). Expansion of Concrete through Reaction Between Cement and Aggregate. *Proc. ASCE*, V. 66, No. 10, pp. 1781-1811.
- Stark J. (2008). *Alkali-Kieselsäure-Reaktion*. F. A. Finger-Institut für Baustoffkunde. Bauhaus-Universität Weimar.
- Stark J. & Seyfarth S. *Assessment of Specific Pavement Concrete Mixtures by using an ASR Performance-Test*. Bauhaus-Universität Weimar.
- Steffens A., Li K. & Coussy O. (2003). Aging Approach to Water Effect on Alkali-Silica Reaction Degradation of Structures. *Journal of Engineering Mechanics*.
- Swamy R.N. (1992). *Alkali-Silica Reaction in Concrete*. Blackie & Son Ltd. Glasgow.
- Tamma K.K., Dowler B.L. & Railkar S.B. *Computer Aided Applications to Injection Molding: Transfinite/Finite Element Thermal/Stress Response Formulations*. Department of Mechanical Engineering, University of Minnesota.
- The Concrete Society (1999). Alkali-Silica Reaction: Minimising the Risk of Damage to Concrete. *Concrete Society Technical Report No. 30*. Third Edition. Slough.

- Ulm F.J., Coussy O., Kefei L. & Larive C. (2000). Thermo-Chemo-Mechanics of ASR Expansion in Concrete Structures. *Journal of Engineering Mechanics*, Vol. 126, No. 3.
- Unger J.F. (2009). *Neural Network in a Multiscale Approach for Concrete*. Ph.D Thesis. Bauhaus-Universität Weimar. Germany.
- Wang J.G., Leung C.F. & Chow Y.K. (2003). Numerical solutions for flow in porous media. *International Journal for Numerical and Analytical Methods in Geomechanics*, **27**:565-583.
- Wang Z.M., Kwan A.K.H. & Chan H.C. (1999). Mesoscopic Study of Concrete I: Generation of Random Aggregate Structure and Finite Element Mesh. *Computers & Structures* **70**. pp. 533-544. Elsevier Science Ltd.
- Wang W., Wang J. & Kim M.-S. (2001). An Algebraic Condition for Separation of Two Ellipsoids. *Computer Aided Geometric Design*. **18**(6). pp. 531-539.
- Wang Z.M., Kwan A.K.H. & Chan H.C. (1999). Mesoscopic Study of Concrete II: Nonlinear Finite Element Analysis. *Computers & Structures* **70**. pp. 545-556. Elsevier Science Ltd.
- Wen H.-X., Wang Y.-Q. & Balendran R.V. (2004). Damage Mechanics Model for AAR Affected Concrete. *Proceedings of the 12th International Conference on Alkali-Aggregate Reaction in Concrete*.
- Wittmann F.H., Roelfstra P.E. & Sadouki H. (1984). Simulation and Analysis of Composite Structures. *Material Science Engineering* **68** (2). pp. 239-248.
- Wittmann F.H., Sadouki H. and Steiger T. (1993). Experimental and Numerical Study of Effective Properties of Composite Materials. In C. Huet (Ed.), *Micromechanics of Concrete and Cementitious Composites*, Universitaires Romandes Lausanne, pp.59-82.
- Wriggers P. & Moftah S.O. (2005). *Mesoscale Model for Concrete: Homogenisation and Damage Behaviour*. Finite Elements in Analysis and Design **42**. pp. 623-636. Elsevier B.V.
- Xu Z., Lan X., Deng M. & Tang M. (2000). A New Accelerated Method for Determining the Potential Alkali-Carbonate Reactivity. *Proceedings of the 11th International Conference on Alkali-Aggregate Reaction*. pp. 129-138. Québec.
- Zaitsev Y.B. & Wittmann F.H. (1981). *Simulation of Crack Propagation and Failure of Concrete*. Material Structures **14**(2). pp. 357-365.